# Vitrification and nanowarming at human organ scale

A DISSERTATION SUBMITTED TO THE FACULTY OF THE
GRADUATE SCHOOL OF THE UNIVERSITY OF MINNESOTA
BY

Lakshya Gangwar

IN PARTIAL FULFILLMENT OF THE REQUIREMENTS FOR THE DEGREE OF
DOCTOR OF PHILOSOPHY

Advisor: Dr. John C. Bischof

August 2024

# Acknowledgments

"Om Shri Gurubhuya Namah" I would like to thank the almighty paramatma who in form of my param pujya gurudev (spiritual teacher) has always been with me throughout the journey of this PhD life and beyond. The realization of "tat tvam asi" meaning almighty is within me has opened me to bliss, knowledge and satisfaction.

I would like to start by thanking my maa, Tara Gangwar who has sacrificed immense hours of her precious life for raising, teaching and caring for me through my education pathway and implanted the "sanskars" vedic values. Next, my father Lalta Prasad Gangwar, who has always provided me food and safety with all his love. My sisters Divya and Preeti, who have raised me like their own son and always been by my side, thank you to them. All my family has been the most supportive in my personal and academic life and I couldn't be where I am without them and deeply grateful to them.

My academic journey to PhD has lot of inspiring people on the way from elementary school at B.B.L. Public School, Bareilly, my tuition coach Mr. Sharma, IIT-Jee coach Abhishek Sir, my good friends like Manjush who pushed me to study harder, IIT Kanpur professors such as late-Dr. Sameer Khandekar, and Dr. Laxmidhar Behera-spiritual guide, and friends I cultivated at IITK -Saurabh, Balsant, Saurav, Lokendra, etc list goes on.

Next, I would like to express my sincerest gratitude to my one-of-a-kind advisor, Dr. John C. Bischof, for his unwavering support, guidance, and mentorship throughout my research journey. He has been my role model in the cryopreservation research world. I still recall the day I was hesitant to work with biological tissue, organs eventually developing my passion for engineering applied on biological things. I always will remember his lesson of not reinventing the wheel, thinking of the limits of problem, "science is simple" and excellence cannot be rushed. His mentorship extended beyond academic life to professional and social life where I will always rejoice his lesson of "suit analogy". He is an excellent guide who fostered my mind to always look from a high-level view of any research problem and then think of limiting scenarios to solve at start. His guidance has developed in me, a spirit of interdisciplinary collaboration and solving a diverse problem without reinventing the wheel. He mentored me in professional skills nurturing my overall growth as graduate-student. He helped me become an independent researcher and I am always grateful for the opportunity to have worked with multiple projects with highly interdisciplinary field. I am always grateful for the opportunity to work in his outstanding lab and use his excellent resources, which were crucial to the success of my project. I also owe my job-

hunting success to his support and valuable advice. I feel fortunate to have had such an amazing advisor, and I will always be grateful for his contribution to my academic and professional career throughout my life. And interestingly, I would like to point out my advisor providing me his invaluable hours on Sundays have become core memories for which I will always be obliged to him.

I would like to thank Dr. Michael Etheridge for his continued mentorship and wonderful engineering insight always even on his busiest days. Now, I would start thanking my wonderful lab members at University of Minnesota starting from Dr. Zonghu Han who was always a friend, colleague and avid pool of knowledge. Casey Kraft with whom I have intellectual discussion on research topics and deeper meaning of life. Elliott Magnuson who has always been a friend more than a labmate. Now I need to thank Pegah Ranjbartehrani specifically as she treated me like a brother and provided heartwarming mentorship and friendship throughout even indirectly helping in this writing of dissertation. I can relate to her in so many struggles during my grad school and gave me comfort in overcoming them as graduate student. Alumni of BHMT lab- Anirudh, Kanav, Jaqueline Pasek-Allen, Zongqi all of which have contributed to my personal growth as a researcher. My collaborator lab folks namely Yicheng, Bat, Joseph, and Saurin-who is the godfather of my cat-Cinnamon taking care of him always. Other lab mates such as Vasu, Minhan, Joe…list goes on but thank you all. Also, I would like to acknowledge Rob Goldstein as a great collaborator at AMF Life systems for support and guidance on RF coils. And vibrant student and beyond community of NSF ERC ATP-Bio which has immensely expanded my connections and outlook in research in last phase of my PhD.

My friend Matt Rogers whose spirit and passion always elevated me intellectually. My dear friend and Minnesota sister namely Arundhati Bhide who always provided her kindness and support. Minnesotan friends such as Nikhil Sethia- who was not only a friend but also amazing colleague helping me throughout my PhD. My Duluth friend-Amarjeet Tiwari who is always a fellow adventure seeker, joyful person and became my wonderful friend. I would like to acknowledge numerous taxpayers whose contribution to a nation‘s economy indirectly allow students like myself to pursue research in science, technology and medicine. And I acknowledge the indigenous native American tribes whose ancestral lands, University of Minnesota physical space stands this day.

I would like to also extend my heartfelt gratitude to my amazing PhD final exam committee members: Dr. Paul Iaizzo, Dr. Rhonda Franklin, Dr. Jeff Tithof, and my PhD prelim-oral committee members Dr. Xiaojia Wang and Dr. Perry Leo. Their extensive knowledge, insightful comments,

and constructive feedback helped me to improve my research work in ways that I couldn't have done on my own. I greatly appreciate their invaluable contributions to my research, and I am truly grateful for their unwavering support and encouragement throughout my final phase of PhD.

Last but foremost, I would like to thank my amazing fiancé Lori Anne Carpenter (my “chanda”-moon and princess jasmine) who is the love of my life, most caring and just for being there with me throughout my PhD journey. I am always privileged to have her companionship from the novel yummy “Strawberry Ladoos” to her original charming fantasy book, thank you sugar for brightening the colors in my life. And Cinnamon my pet cat who is the calmest and most peaceful kitty…indeed a “Buddha” (awakened) living being.

# Dedication

To my Gurudev- Pujya Bapuji; parents- Tara Gangwar, LP Gangwar; sisters- Divya and Preeti, and my dearest and nearest fiancé- Lori Carpenter alongside kitty-Cinnamon.

# Abstract

Cryopreservation of biomaterials is an area that has been studied for a variety of applications from organ transplantation and in vitro fertilization to food preservation and biodiversity conservation. Cryopreserved biomaterial can in principle have indefinite shelf life due to the biological arrest of metabolism in the cryogenic temperature range. More than 100,000 people in the United States alone were on the organ transplant waitlist as of March 2024 while only ~20,000 organs (living and deceased) were donated last year, highlighting a large gap in transplantable organs and a need for "organ banking." Vitrification is one of the most promising approaches for cryopreservation and has been successfully applied to a variety of systems such as cells and tissues and on the scale of rat and rabbit organs. The major challenges in cooling to and rewarming from a vitrified state remain ice crystallization and cracking/fracture. Ice crystallization can be inhibited by the use of cryoprotective agents (CPAs), though the inhibition further depends upon the rates achieved during cooling and rewarming. The minimum rate required to prevent any ice crystallization or recrystallization/devitrification for a given CPA is called the critical cooling rate (CCR) or critical warming rate (CWR), respectively. On the other hand, physical cracking is mainly related to thermomechanical stresses, which can be avoided by maintaining temperature differences ($\Delta T$) below a critical threshold. The other biological mode of failure not focused on this physical study is CPA toxicity that has been studied in literature and shown that successful loading & unloading of CPA without significant toxicity induced injury could be performed.

The first objective of this study is to perform a literature review for thermophysical properties of CPAs and tissues which govern the heat transfer within a biomaterial during cryopreservation. After compiling all the property values, we modeled heat transfer in bulk systems to predict failure modes during vitrification and rewarming, i.e., ice formation and physical cracking/fracturing and how to avoid them at multi-scale.

In our second objective, a numerical heat transfer model is developed for understanding the limits of success and failure at different length scales for cryopreservation by vitrification. Here we use thermal modeling (finite element analysis, FEA) to help us understand the magnitude and trajectory of these challenges as we scale the biomaterial volume for a given CPA from milliliter to liter scale. This modeled work is a guide for mL to Liter bulk vitrification and rewarming.

Third we measured dielectric properties of common organ vitrification CPAs which allowed us to characterize the uniformity and feasibility of nanowarming liter scale volumes in a newly built 120 kW radiofrequency (RF).

Our final and major objective is to apply the knowledge gained in previous objectives of numerical model predictions for choice of CPA, characteristic length of geometry, and specific cooling and rewarming conditions (nanowarming) for achieving potential experimental success of cryopreservation by vitrification. We demonstrate successful physical vitrification of multi-liter (up to 3L) in CPA systems and in a human-scale organ (porcine liver) which is the first largest human scale vitrification and nanowarming reported to our knowledge. We utilized several techniques for physical assessment including μCT imaging, visual evaluation, and thermometry depending upon the type of system and mode of failure. Furthermore, we rewarm multi-liter CPA systems (up to 2L) using iron-oxide nanoparticles inside a state-of-art 120 kW RF coil producing magnetic field strengths up to 35 kA/m, 360 kHz, and a capacity of 2.5 L. Lastly, we predict cooling and nanowarming rates inside smallest to largest human organs based upon simple assumption of ellipsoidal geometry, vascular fractions and characteristics length. Using thermometry, we show that cooling rates decrease to roughly <1 ˚C/min and would need longer thermal equilibration (annealing) times from >4 hours for bag volumes of CPA > 0.5L. This suggested the need for future methods to invent faster and uniform cooling methods to ensure vitrification in ≥ 1 L volumes or to choose CPAs with extremely low CCRs.

To summarize, we characterized the success and failure of vitrification based on ice crystallization and physical cracking/fractures. We developed a numerical model based upon characteristic length ($L_c$) to provide guidance for successful vitrification and rewarming of any system. We demonstrated vitrification at human-scale CPAs and in a porcine organ and finally nanowarming of these liter systems with distributed IONPs through a state-of-art 120 KW RF coil.

This work will not only act as a guide for understanding success and evaluating failure modes but also advance the current limits of vitrification and rewarming toward the scale of human organ in the field of cryopreservation, hopefully contributing to “organ banking” as a reality in the near future.

# Table of contents

# List of Tables

# List of Figures

# Chapter 1. Introduction to Vitrification and Nanowarming

In this chapter, we provide an overview of vitrification and rewarming approaches which have been applied in literature in various physical and biological systems. We discuss the two major failure modes that need to be addressed for scaling physical success of vitrification and rewarming at liter volume sizes relevant for human organs. Additionally, we provide a concise comparison of various rewarming approaches specifically volumetric rewarming needed for successful thawing of vitrified large-scale samples. This body of work is submitted as a review article to the Annual Review of Heat Transfer. The manuscript is reproduced here:

**Gangwar, Lakshya**, et. al. "Bulk cryopreservation enabled by nanowarming." Annual Review of Heat Transfer (2024) In submission.

## Overview

Scaling up the warming of larger vitrified biomaterials has been a barrier to cryopreservation of organs and other bulk systems. The two main challenges are ice recrystallization and physical cracking/fractures, which occur due to slow rates and thermal non-uniformity, respectively, which are inherent to traditional boundary rewarming. This chapter reviews this issue and various attempts to address it through volumetric rewarming including radiofrequency rewarming with magnetic nanoparticles (nanowarming), Dielectric/Microwave rewarming, and high intensity focused ultrasound (HIFU). Of these approaches, only nanowarming has demonstrated scalability of rates up to ~1500°C/min and volumes as large as 2 liters. To enhance translation and practical use of nanowarming, a comparison table for RF coils and magnetic nanomaterial (nanoparticles) based upon literature is provided, highlighting different commercial and laboratory-built options. Further, regarding the ease of implementation of nanowarming, this chapter summarizes biological outcomes for vitrified samples (organs, tissues) rewarmed using nanowarming to date. Lastly, we lay out the current state-of-the-art technology for nanowarming and the potential role this volumetric technique can play in the success of organ banking and beyond.

## Motivation for cryopreservation by vitrification- from regenerative medicine to space travel

A method to extend the preservation limits of organs would revolutionize how organs are recovered, allocated, stored, and ultimately used to save lives through transplantation. Unfortunately, organs begin to sustain ischemic damage as soon as they are recovered from the donor. To reduce injury, organs are traditionally stored at 0–4°C (in a cooler), at which temperature metabolic demand is lower. However, injury from cooling still occurs, and preservation under these conditions is limited to 4–6 hours for hearts and lungs, 10-12 hours for livers and pancreases, and 24–36 hours for kidneys [1-3]. Even so, for each of these, shorter preservation is better. Preservation would be extended if organs could be stored at even lower temperatures. Indeed, at cryogenic temperatures below -140°C, organ preservation is theoretically indefinite [4, 5], enabling true organ banking. Organs could then potentially wait for patients, rather than patients waiting for organs. The downstream benefits would be considerable: better donor/recipient matching, increased organ utilization, enablement of tolerance induction protocols that take days or weeks before transplant, better patient preparation for surgery, reduction in inequities of access, and ultimately, more lives saved. Such technology could be extended even further, from practical

applications such as the preservation of organs for biomedical research to ethereal concepts of deep space travel in a state of suspended animation.

## Introduction to vitrification and its principles

Ice formation is one of the most critical barriers preventing success in cryopreservation. When ice crystals form, they can destroy cells, intracellular organelles, and even the macroscopic integrity of organs and tissues. One way to avoid injury from ice formation is to minimize or prevent its formation altogether. Vitrification, or the transformation of biomaterial into a non-crystalline glass-like amorphous solid, could enable cryopreservation without ice [4, 6].

To achieve vitrification, the biomaterial must be cooled from above the melting point ($T_m$) of the material's fluid components, i.e., water, to below the glass transition temperature ($T_g$) where molecular movement is so decreased as to prevent the phase transition from the liquid to crystalline state [6]. At these low temperatures (<-120°C), the material enters a stable glass-like state. To avoid ice formation, cryoprotectant agents (CPAs) such as sugars, alcohols, and other organic compounds are added to inhibit ice and stabilize the cellular components [7]. Strategies to cool biomaterials to the vitrified state can be categorized into equilibrium and non-equilibrium vitrification.

In equilibrium vitrification, CPA agents are progressively added as the system cools (Figure 1.1). As CPA concentration increases, the $T_m$ decreases, and the system remains liquid. This so-called "liquidus tracking" allows cooling to proceed along the phase ($T_m$ curve in the phase diagram of a CPA; Figure 1.1) while avoiding dropping below $T_m$ and escaping freezing. If enough CPA can be added and temperature decreased sufficiently, the system eventually enters a vitrified and stable state below the $T_g$ line. In simple words, equilibrium vitrification is a way to reach $T_g$ by keeping the sample close to (or slightly above) the $T_m$ line (water–ice phase change curve) in the phase diagram, as seen in Figure 1.1. A second method for achieving the vitrified state is rapid cooling from above the $T_m$ to below the $T_g$. In this approach, the system enters a stable glassy state when it is quickly cooled down to the $T_g$. During rewarming, the reverse occurs; temperatures rapidly rise from below the $T_g$ to above the $T_m$. As shown in Figure 1, non-equilibrium (or rapid) vitrification is more favorable for bulk organs, as shown in the green region, where heterogeneous nucleation is either within 10–20°C of $T_g$ or disappears completely once the $T_{het}$ falls below $T_g$. The blue region implies a higher probability of ice formation and, hence, is unsuitable for glass formation. Further, $T_d$ approaches $T_m$ in the green region, meaning that ice recrystallization or devitrification is avoidable, given that ice crystal growth in the nuclei during rewarming is minimal

once $T_d$ disappears. Finally, the red region in Figure 1, though very stable for glass formation as both $T_d$ and $T_{het}$ vanish, has such a high concentration of CPA that toxicity is likely, especially when considering something as complex as an organ.

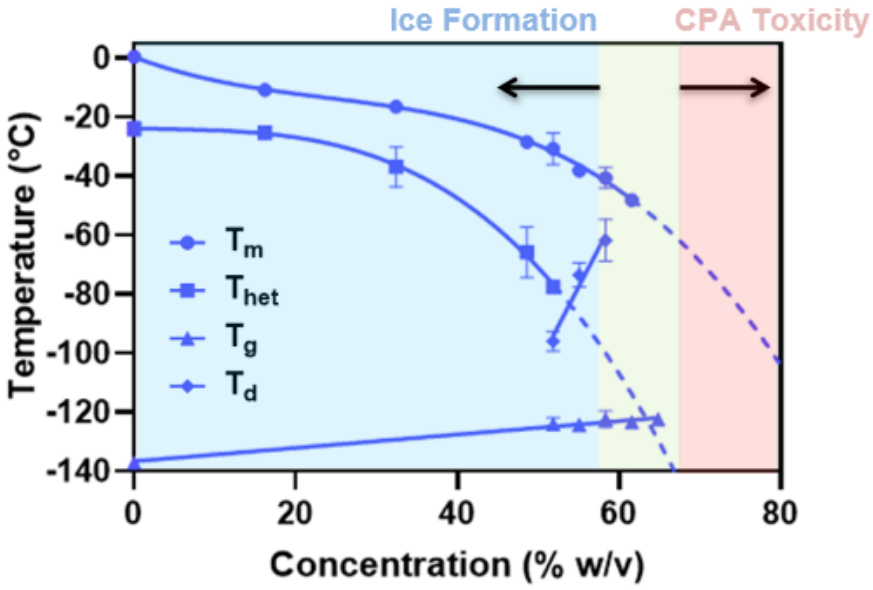


Figure 1.1: Supplemental phase diagram of the most promising organ vitrification CPA M22 showing various transition temperature curves, i.e., Tm = melt (liquidus) temperature; Thet = heterogenous nucleation temperature; Tg = glass-transition temperature; Td = devitrification temperature. Rapid cooling achieves non-equilibrium vitrification. The blue region indicates a risk of ice crystallization, the red area indicates a risk of higher CPA toxicity, and the green region indicates achievable successful vitrification. Adapted and modified from [8] with permission.

This classification of stable and unstable regions for vitrification has been described in detail by Fahy et al. [4]. A careful balance between ice formation and CPA toxicity is needed to achieve successful non-equilibrium (rapid) vitrification at the size of human organs. This approach is also more commonly applied and practical for bulk systems such as organs and can be combined with volumetric rewarming techniques such as nanowarming for successful uniform thawing of bulk vitrified systems.

To achieve vitrification and successful return, organs must pass through the ice crystal growth and nucleation regions twice, once upon cooling and again upon rewarming [6]. To avoid ice crystallization during both cooling and rewarming, the rates must be faster than the kinetics of ice crystal growth and minimize thermodynamic (ice nucleation) events. This translates into practical

thresholds, defined as critical cooling rates (CCR) and critical warming rates (CWR). For instance, CCR is described by Boutron as the rate that results in less than 0.2% ice within the solution mass [9], and CWR corresponds to the warming rate when ice crystallization comprises less than 0.2–0.5% of solution mass [10]. Notably, the CWR is always one to two orders of magnitude higher than the CCR, presumably because ice is nucleated within the system during cooling, even if crystallization does not occur. This means that conditions for crystallization around these nuclei will be favorable during warming. The amount of ice formed at any rate is denoted by ice fraction (q), calculated by Eq. 1 using the latent heat of ice crystallization recorded by a differential scanning calorimeter (DSC) during a specified cooling or warming rate.

$$q = 100 * (\frac{\Delta h}{\Delta h_w}) \qquad (1)$$

Where $\Delta h_w$ is the latent heat of water at 0°C,

and $\Delta h = \frac{1}{m}\int_{t1}^{t2} \frac{dH}{dt} dt = \frac{1}{m}\int_{t1}^{t2} \frac{dH}{dt} * \frac{dt}{dT} dT = \frac{1}{m}\int_{T1}^{T2} \frac{DSC\ Heat\ Flow}{Cooling\ Rate} dT$

Furthermore, specific criteria for these ice fraction and other calorimetric parameters such as $T_m$, $T_d$, etc., measured by DSC, are used to estimate the defined CCR and CWR thresholds and can be found in the literature [9, 10]. Note that these critical rates will decrease with increased CPA concentrations [11], allowing successful vitrification and rewarming at higher CPA concentrations for larger-scale systems such as organs. Various studies have summarized the CCR and CWR of common CPAs and CPA mixtures and the tissues permeated with them [11-13].

## Motivation for volumetric rewarming

Successful vitrification and rewarming of cells in suspension or small cell aggregates, such as mammalian embryos, was demonstrated many decades ago [14-16]. More recently, larger biomaterials, such as whole rabbit kidneys [4], ovaries [17], vascular tissue [18], articular cartilage [19], heart valves [20], etc., have also been successfully vitrified. However, in part because the CWR is much greater than CCR (usually an order or more) [11], the ability to rewarm larger tissue structures and whole organs has remained a barrier in the field [21]. The challenges of rewarming were twofold: 1) rewarming has to be fast enough to avoid ice crystallization (devitrification) during rewarming [6, 22], and 2) rewarming has to be sufficiently uniform to avoid cracking due to thermal stress [23], as shown in Figure 1.2.

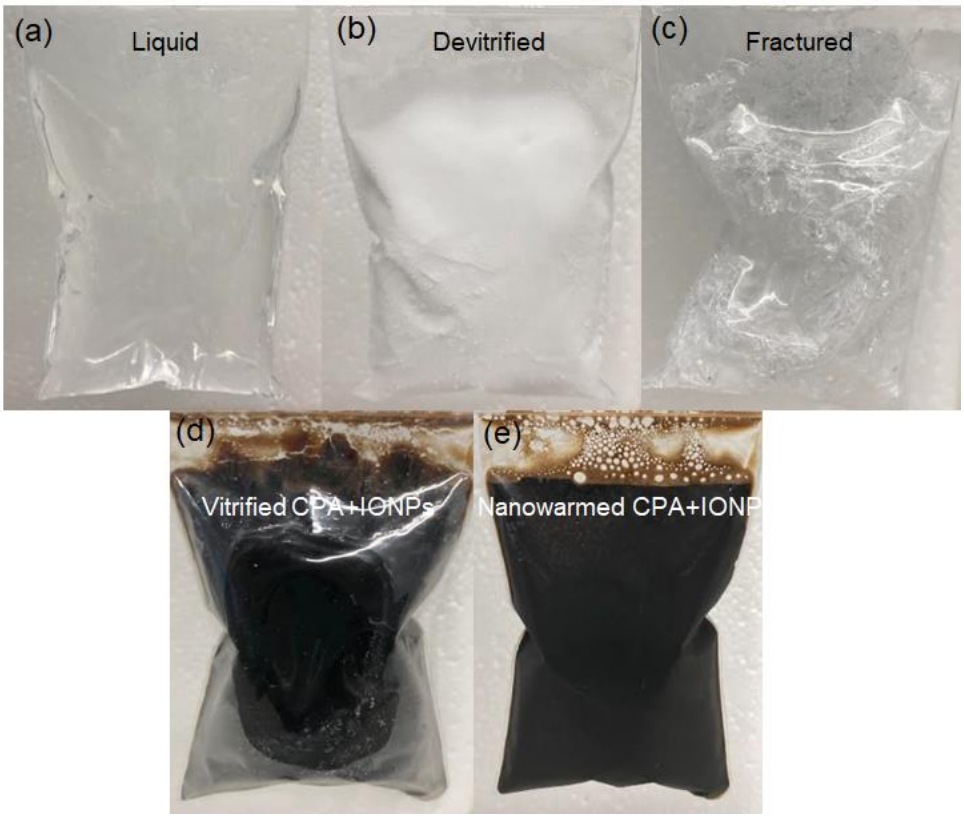


Figure 1.2: Successful vs failed vitrification (fracture and recrystallization/devitrification in a bulk system). Photos show 30mL volumes of CPA VS55 and CPA+EMG308 IONPs: (a) liquid CPA before vitrification; (b) devitrified or recrystallized CPA during rewarming; (c) fractured CPA during rewarming; (d) vitrified CPA+IONPs; (e) successfully nanowarmed CPA+IONPs, showing no cracks or crystals

Although successful vitrification in an organ can be physically achieved, the amount of CPA needed to avoid ice formation is often toxic. Indeed, Fahy and colleagues demonstrated that convective, or boundary-layer, heating could only achieve partial success [21]. In short, boundary warming is both too slow and nonuniform to successfully rewarm larger biomaterials, such as human organs, at tolerable CPA concentrations. Rapid and uniform volumetric heating is thus essential for rewarming cryopreserved organs.

## Introduction to rewarming of cryopreserved biomaterials

A successful cryopreservation protocol requires stable rewarming from a cryopreserved state, which for vitrified samples would be from cryogenic temperatures (i.e., below glass transition temperatures, <-120°C for common CPAs) at which the biomaterial is stored for stable shelf life.

As discussed in the section above, a faster and more uniform rewarming beyond boundary warming is crucial to achieving successful cryopreservation of biomaterials such as organs. The volumetric rewarming of bulk systems is one approach to accomplish this. For instance, radiofrequency (RF) fields for tissue heating have been used for magnetic hyperthermia-based treatments in thermal medicine [24-26], demonstrating that heat generation can occur due to high-frequency dielectric and microwave rewarming within a cryopreserved system [27]. This concept is being revisited because key aspects of uniformity could not be accomplished until recently. Furthermore, nanoparticle-induced heating in the presence of lower radiofrequency (RF) fields, or nanowarming, has also been used [28, 29]. Other volumetric rewarming techniques, such as high-focused ultrasound (HIFU), have also been attempted [30, 31]. Table 1.1 provides a comparison of various such methods.

Rewarming can be classified into two major categories: boundary and volumetric. Boundary heating techniques can be further divided into convection-based boundary techniques, such as those used by Fahy and others, which usually involve a water bath or air rewarming, and conduction-based heating, such as Joule heating or inductive metal form heating. In convection-based heating techniques, heat is dissipated to the sample via convection at the boundaries, and then conduction occurs inside the sample, such as in a water bath [32], where forced liquid convection is usually the primary mode of boundary heating, or in the case of air rewarming [32, 33], where free gaseous convection is the primary mode of boundary heating around the sample. In conduction-based heating techniques, the generated heat in a sample is dissipated primarily by conduction throughout the sample from the boundary heating source. This heating source can be produced by either electric currents, as with Joule heating [34, 35], or RF fields for inductive metal form heating [36].

Boundary techniques have several limitations. For instance, they create temperature gradients within a sample as heat flows from the source at the boundary to the inside core of the sample and is, hence, nonuniform throughout the volume. Further, when using such boundary warming techniques, warming rates inside a biomaterial decrease as the size of the biomaterial increases because heat diffusion must travel further inside.

Volumetric techniques, on the other hand, are uniform, faster, and independent of sample size, namely radiofrequency (RF) heating or nanowarming, dielectric heating, microwave heating, and high-intensity focused ultrasound (HIFU) rewarming, as shown in Table 1.2. All these techniques, except Nanowarming, generate heating within a sample, but their uniformity depends on temperature-dependent properties, and spatial uniformity depends upon the attenuation of the field

inside the sample (see Table 1.2). More importantly, RF fields used in nanowarming do not attenuate significantly within the sample and couple directly with magnetic nanoheaters instead of the sample directly. Further, radiofrequency (RF) operates at lower frequencies (longer wavelengths), resulting in more considerable penetration depths when compared to dielectric/microwave rewarming. Therefore, nanowarming rates are inherently independent of the size of the heated sample, meaning the warming rates do not decrease with the size of the sample. The penetration depth can also be adjusted by altering the frequency; a lower frequency creates larger penetration within the sample. For all these methods, the warming rates are controlled by adjusting the power, the electric or magnetic field, and/or the frequencies listed in Table 1.2. The highest warming rates reported in the literature are plotted in Figure 1.3. Indeed, nanowarming is able to operate across the broadest set of rates and volumes. Rates as high as ~1500°C/mins and can controlled (elevated or decreased) with volumes as high as 2 L by increasing or reducing iron-oxide nanoparticle (IONP) concentrations and manipulation of field parameters (green dashed line).

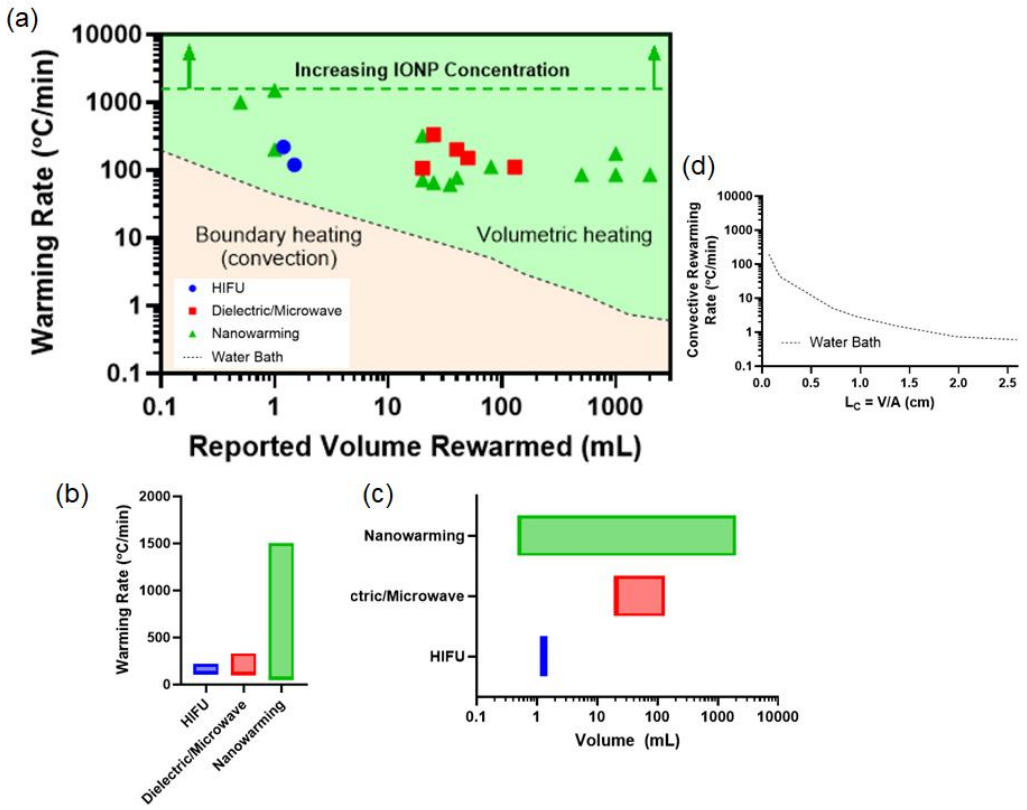


Figure 1.3: Bulk rewarming technologies reported by rate and size in literature. (a) Plot of highest rewarming rates achieved for volumes rewarmed from vitrified cryogenic temperatures in literature. Bar charts showing (b) the largest warming rate reported among the different volumetric

rewarming techniques and (c) the range of bulk volumes rewarmed using these various techniques. Boundary rewarming rates for a method, such as convective rewarming using a water bath, are also plotted as the lower black dashed line, which inherently begins to fall with increasing volumes. The green upper dashed line represents nanowarming rates, which are not affected by size and can be further increased theoretically with higher concentrations of IONPs. Also, note that the water bath curve is based upon modeled warming rates for $h=100W/m^2.K$ from for CPA M22 plotted for a specific volume [37]. The plotted water bath rewarming rates curve is an estimate modeled for a specific $L_C$ (cylindrical geometry) [37]. Plot (d) is a more precise way to estimate the convective warming rate using a water bath by calculating the $L_c$ (=V/A) for the sample. WRs are reported as the highest numbers (peak values) from the literature at their largest input settings, such as field, frequency, power, etc. For the plot data values, refer to Table 1.1 below.

Table 1.1: Reported highest warming rates (WR) at different volumes compiled from notable literature for the various volumetric rewarming techniques.

| Technique | Total Sample Volume | Sample type | | Highest WR | Temperature Range WR is calculated | Reference |
|---|---|---|---|---|---|---|
| Nanowarming | 0.5 mL | VS55+$Co_{35}Fe_{65}$ Nanowires | 10mg/mL | 1000°C/min | -150 to 0°C | [38] |
| | 1 mL | VMP+EMG308 IONPs | 100mgFe/mL | 1500°C/min | -100 to 0°C | This study |
| | 1 mL | HDF cells+VS55+EMG308/1200 | 59mgFe/mL | 200°C/min | -150 to -20°C | [39] |
| | 20 mL | Mouse pancreatic islets+IONPs | 5mgFe/mL | 72°C/min | -123 to -38°C | [40] |
| | 20 mL | VS55+IONPs | 10mgFe/mL | 321°C/min | Not mentioned | [41] |
| | 25 mL | Rat kidney+VS55 | 10mgFe/mL | 65°C/min | -90 to -45°C | [42] |
| | 35 mL | Rat liver+EG+Sucrose | 10mgFe/mL | 61°C/min | -90 to -45°C | [43] |
| | 40 mL | Porcine articular cartilage-OCA+CPAs | 2mgFe/mL | 77°C/min | -135 to -30°C | [44] |

| | | | | | | |
|---|---|---|---|---|---|---|
| | 80 mL | VS55+IONPs | 10mgFe/mL | 112°C/min | -135 to -30°C | [29] |
| | 1000/2000 mL | M22+EMG308 | 10.7/4.6 mgFe/mL | 180/90 °C/min | -100 to 0°C | This study |
| HIFU | 0.2-1.2 mL | 30%(v/v)Glycerol+ C.elegans | NA | 218°C/min | -60 to -40°C | [30] |
| | 1.5 mL | Sheep ovary | | 119°C/min | -140 to -20°C | [31] |
| Dielectric / Microwave | 20 mL | DPVP | | 106°C/min | -70 to -0°C | [45] |
| | 25 mL | DPVP: 41%v/v DMSO+6%w/v PVP | | 332°C/min | -150 to 0°C | [46] |
| | 40 mL | Canine kidney+DMSO | | 200°C/min | -80 to 4°C | [47] |
| | 50 mL | Rabbit kidney+M22 | | 150°C/min | -100 to -30°C | [48] |
| | 130 mL | 60%w/vDMSO+ Acetamide | | 111°C/min | -100 to 0°C | [49] |

Electromagnetic (non-contact) heating can be either directly coupled to a biological sample, such as in dielectric heating, microwave rewarming, or Joule heating, or indirectly coupled using external heaters in or around the sample, such as in inductive RF rewarming or metal form rewarming. Inductive RF rewarming by nano-sized magnetic heaters, called “nanowarming,” has shown considerable promise in cryopreservation applications for uniformly and rapidly heating cryopreserved biological materials, including cells [28, 29, 39, 50], organoids [40, 51], tissues [29, 32, 44, 52], and even whole organs [41, 43, 53-55]. During nanowarming, heat is generated by the hysteresis of magnetic nanomaterial such as IONPs in an alternating magnetic field [56]. The generated heating is uniform, as the IONPs are distributed throughout the vasculature of an organ after the organ is perfused with CPAs, or the IONPs are dispersed uniformly throughout the solution containing biomaterial such as cells and tissues. Further, this heating can be easily increased by controlling the amount of IONPs. A typical workflow for nanowarming a cryopreserved organ is shown in Figure 1.4.

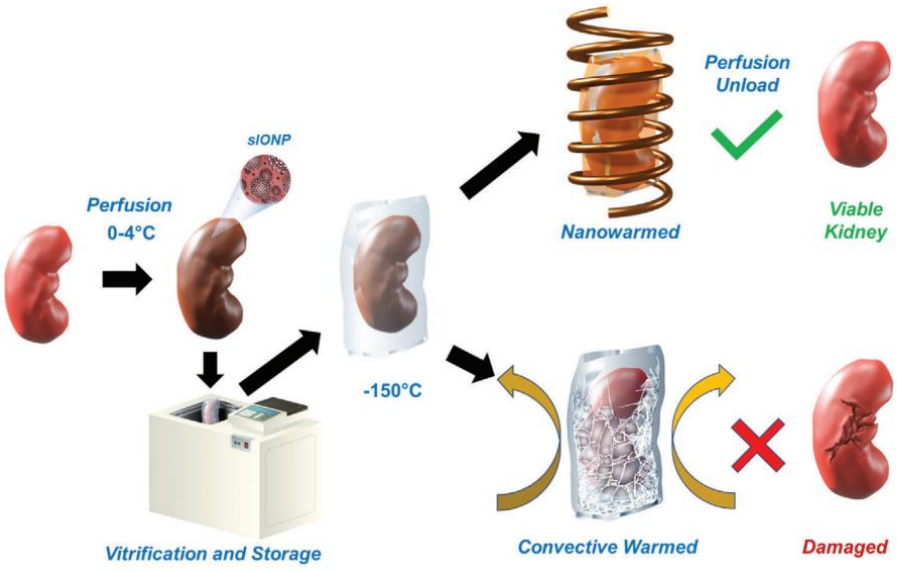


Figure 1.4: Overview of the steps involved in nanowarming a bulk system such as a kidney. Reprinted from [42] with permission (© 2021 The Authors, Advanced Science published by Wiley-VCH GmbH, CC BY 4.0).

Notably, the RF waves used in nanowarming are in the kHz range (typically 100–400kHz), which implies a longer wavelength and ensures deeper RF penetration inside any tissue, even a large clinical-scale organ. Nanowarming inherently produces negligible temperature gradients across samples irrespective of their size if IONPs are uniformly distributed throughout the volume, such as throughout the capillaries [29, 42]. For organ nanowarming, since the magnetic nanoparticles remain in the vasculature, the vascular fraction of an organ plays an important role in achievable rewarming rates. As an example, in a highly vascularized organ such as the lungs (vascular fraction ~35%), one can attain warming rates of (~>10°C/min) at perfused IONPs concentrations as low as ~2mgFe/mL, as opposed to a less vascularized organ such as the brain (vascular fraction ~5%). A similar warming rate (~10°C/min) in the brain would require five times the perfusion IONP concentration (~10mgFe/mL) (Gangwar et al 2024, in submission). Therefore, strictly speaking, vascular heating would mean the uniformity of nanowarming is governed by the uniformity of the vasculature [57]. Now, the intervascular distance inside an organ is usually small enough for heat to travel via diffusion on the same relative timescales of heating (thermal diffusion length: $L = \sqrt{4\alpha t} \sim 0.6$ mm for 1 sec and $\alpha \sim 8.4e\text{-}8$ $m^2/s$ for M22, which is sufficiently larger than average intercapillary distances ~ 20µm -100µm in human organs such as brain [58], heart [59] & kidney [60] [61] allowing effectively uniform temperature rise throughout the organ.

Dielectric or microwave heating is another non-contact volumetric rewarming approach that directly couples EM fields with the sample to produce heat. Unlike nanowarming, the frequency of EM waves being used is much higher, typically MHz for dielectric and GHz for microwave heating. These methods rely upon heating due to the relaxation of dipole molecules such as water or CPAs in a sample and are often challenging due to spatial nonuniformity caused by the uneven, uncontrolled distribution of dipolar molecules inside a sample and temporal non-uniformity due to the temperature dependence of the material's dielectric properties. More specifically, it is hard to achieve controlled heating in these systems, which can lead to overheating the tissue in microwave heating [27] and thermal hotspots in dielectric heating due to the contribution of DC electrical conductivity in dielectric loss (example from ionic components in CPAs) warming at near-zero temperatures [62]. This uncontrolled heating is often called "thermal runaway." It puts various constraints on a biomaterial/CPA composition, heating rates, and end temperature when the composition is rewarmed from a vitrified state [63-65]. Another limitation with dielectric and microwave rewarming is that smaller penetration depths inside clinical-scale organs (e.g., for a human liver whose max. dimension is ~15 cm, the penetration depth of DMSO < 5cm at 2.45 GHz for commercial microwave or < 10cm at 434MHz for dielectric heating [62]). Lastly, this form of rewarming limits the possible heating start temperature because the dielectric loss (i.e., ability to heat) for common CPAs decreases rapidly in vitrified state due to the physical limitations in the mobility of molecules in a glassy state. This means the heating cannot be produced in the glassy state and needs to wait until the glass transition temperature is reached using other forms of rewarming, such as convective rewarming [48]. Moreover, a dielectric heating system based on an EM resonance cavity [46, 66] has been attempted to avoid thermal runaway for cryopreservation applications. This approach has been tested on smaller volumes (<25 mL) and still shows spatial nonuniformity across the sample compared to nanowarming.

Another volumetric approach, called High-intensity focused ultrasound (HIFU), is a non-electromagnetic form of volumetric heating technique that utilizes the absorption of energy from sound waves to produce heating inside a sample. It has been used widely for clinical trials of diseased non-frozen tissue and approved for treatments, mainly for thermal ablation applications [67-69]. It has recently been applied in cryopreservation applications by utilizing a focused array of transducers and the careful characterization of power, frequency, and acoustic sample-coupling medium matching [30, 31, 70]. Some of the challenges faced by HIFU are real-time thermal monitoring using imaging such as MRI in order to avoid unintentional burning of tissue, reflections of ultrasound waves at interfaces of coupling medium and vitrified biomaterials at cryogenic

temperature, and ultrasonic cavitation at higher temperatures, which, similar to thermal runaway in dielectric heating, can induce tissue damage [69]. Further, the attenuation coefficients and speed of sound are temperature dependent [71] and hence pose another challenge to uniformity of rewarming due to mismatch between sample medium's and coupling medium's acoustic impedance [31]. So far in the literature, HIFU rewarming has only been demonstrated for mL-scale samples [30, 31].

Hence, the demonstration of the scalability of all the volumetric techniques, HIFU, dielectric, and microwave, has been limited (HIFU ~ <2mL, Microwave ~ <40mL, or Dielectric ~ <100mL). In summary, unlike nanowarming, these methods have yet to show the ability to rapidly and uniformly rewarm at the Liter(s) scale, which will be necessary for human organs.

Table 1.2: Overview table for comparison of various rewarming technologies available for heating cryopreserved biomaterial.

| **Heat Generation** | **Technique** | **Source** | **Commercial availability** | **Uniformity** | | **WR Rate Control Parameters** |
|---|---|---|---|---|---|---|
| | | | | Spatial* | Tempera-ture** | |
| **Boundary** | Metal forms (induction) | Electromagnetic (w/o heaters) | Yes | No | No, $\sigma=f(T)$ | f, H, Thickness, $\sigma$ |
| | Joule heating | | Yes | No | No, $R=f(T)$ | V, I |
| | Water bath | Heating Bath | Yes | No | No, $q=f(T)$ | $T_{bath}$ |
| **Volumetric** | HIFU | Sound wave | No | No | No, $\alpha=f(T)$ | f, P |
| | Dielectric/Microwave | Electromagnetic (w/ and w/o heaters) | No | No | No, $\varepsilon''=f(T)$ | f, E, $\varepsilon''$ |
| | Nanowarming (RF rewarming) | | Yes | Yes** | No, $\chi=f(T)$ | f, H, $C_{Fe}$ |

*Spatially uniformity relies upon nanomaterial (heaters) distribution throughout the sample

**Temperature uniformity is absent, i.e., WR=f(T), in almost all of the techniques, as given by specific absorption rate (SAR).

H: Magnetic field strength, E: Electric field strength, f: Frequency, $C_{Fe}$: IONP Concentration, P: Power, ε'': Dielectric loss, σ: Electrical conductivity, χ: Magnetic permeability, $\alpha_s$: Attenuation coefficient, q: Heat Flux, R: Electrical Resistance

# References For Chapter 1


1. Finger, E.B. and J.C. Bischof, *Cryopreservation by vitrification: a promising approach for transplant organ banking.* Current opinion in organ transplantation, 2018. **23**(3): p. 353-360.
2. Groenewoud, A. and J. Thorogood. *A preliminary report of the HTK randomized multicenter study comparing kidney graft preservation with HTK and EuroCollins solutions*. in *Transplant International Official Journal of the European Society for Organ Transplantation: Proceedings of the 5th Congress of the European Society for Organ Transplantation, Maastricht, October 7–10, 1991*. 1992. Springer.
3. Cavallari, A., et al., *A multicenter pilot prospective study comparing Celsior and University of Wisconsin preserving solutions for use in liver transplantation.* Liver Transplantation, 2003. **9**(8): p. 814-821.
4. Fahy, G.M., et al., *Vitrification as an approach to cryopreservation.* Cryobiology, 1984. **21**(4): p. 407-26.
5. Ozgur, O.S., et al., *Current practice and novel approaches in organ preservation.* Frontiers in Transplantation, 2023. **2**: p. 1156845.
6. Wowk, B., *Thermodynamic aspects of vitrification.* Cryobiology, 2010. **60**(1): p. 11-22.
7. Elliott, G.D., S. Wang, and B.J. Fuller, *Cryoprotectants: A review of the actions and applications of cryoprotective solutes that modulate cell recovery from ultra-low temperatures.* Cryobiology, 2017. **76**: p. 74-91.
8. Han, Z., et al., *Supplemented phase diagrams for vitrification CPA cocktails: DP6, VS55 and M22.* Cryobiology, 2022.
9. Boutron, P., *Comparison with the theory of the kinetics and extent of ice crystallization and of the glass-forming tendency in aqueous cryoprotective solutions.* Cryobiology, 1986. **23**(1): p. 88-102.
10. Boutron, P., *Glass-forming tendency and stability of the amorphous state in solutions of a 2, 3-butanediol containing mainly the levo and dextro isomers in water, buffer, and Euro-Collins.* Cryobiology, 1993. **30**(1): p. 86-97.
11. Han, Z. and J.C. Bischof, *Critical Cooling and Warming Rates as a Function of CPA Concentration.* 2020.
12. Peyridieu, J., et al., *Critical cooling and warming rates to avoid ice crystallization in small pieces of mammalian organs permeated with cryoprotective agents.* Cryobiology, 1996. **33**(4): p. 436-446.
13. Hopkins, J.B., et al., *Effect of common cryoprotectants on critical warming rates and ice formation in aqueous solutions.* Cryobiology, 2012. **65**(3): p. 169-178.
14. Luyet, B.J. and E.L. Hodapp, *Revival of frog's spermatozoa vitrified in liquid air.* Proceedings of the Society for Experimental Biology and Medicine, 1938. **39**(3): p. 433-434.
15. Rall, W.F. and G.M. Fahy, *Ice-free cryopreservation of mouse embryos at− 196 C by vitrification.* Nature, 1985. **313**(6003): p. 573-575.

16. Polge, C., A.U. Smith, and A.S. Parkes, *Revival of spermatozoa after vitrification and dehydration at low temperatures.* Nature, 1949. **164**(4172): p. 666-666.
17. Courbiere, B., et al., *Cryopreservation of the ovary by vitrification as an alternative to slow-cooling protocols.* Fertility and sterility, 2006. **86**(4): p. 1243-1251.
18. Song, Y.C., et al., *Vitreous cryopreservation maintains the function of vascular grafts.* Nature biotechnology, 2000. **18**(3): p. 296-299.
19. Song, Y.C., et al., *Vitreous preservation of articular cartilage grafts.* Journal of Investigative Surgery, 2004. **17**(2): p. 65-70.
20. Brockbank, K.G., et al., *Allogeneic heart valve storage above the glass transition at− 80 C.* The Annals of thoracic surgery, 2011. **91**(6): p. 1829-1835.
21. Fahy, G.M., et al., *Physical and biological aspects of renal vitrification.* Organogenesis, 2009. **5**(3): p. 167-175.
22. Boutron, P. and P. Mehl, *Theoretical prediction of devitrification tendency: determination of critical warming rates without using finite expansions.* Cryobiology, 1990. **27**(4): p. 359-377.
23. Steif, P.S., M.C. Palastro, and Y. Rabin, *The effect of temperature gradients on stress development during cryopreservation via vitrification.* Cell preservation technology, 2007. **5**(2): p. 104-115.
24. Jordan, A., et al., *Nanoparticles for thermotherapy.* Nanotechnologies for the Life Sciences, 2007.
25. Atkinson, W.J., I.A. Brezovich, and D.P. Chakraborty, *Usable frequencies in hyperthermia with thermal seeds.* IEEE Transactions on Biomedical Engineering, 1984(1): p. 70-75.
26. Johannsen, M., et al., *Thermotherapy of prostate cancer using magnetic nanoparticles: feasibility, imaging, and three-dimensional temperature distribution.* European urology, 2007. **52**(6): p. 1653-1662.
27. Burdette, E.C., et al., *Microwave thawing of frozen kidneys: A theoretically based experimentally-effective design.* Cryobiology, 1980. **17**(4): p. 393-402.
28. Etheridge, M.L., et al., *RF heating of magnetic nanoparticles improves the thawing of cryopreserved biomaterials.* Technology, 2014. **2**(03): p. 229-242.
29. Manuchehrabadi, N., et al., *Improved tissue cryopreservation using inductive heating of magnetic nanoparticles.* Science translational medicine, 2017. **9**(379): p. eaah4586.
30. Alcalá Guerrero, E., et al., *Sound waves for solving the problem of recrystallization in cryopreservation.* Scientific Reports, 13 (1). 2023.
31. Olmo, A., et al., *The use of high-intensity focused ultrasound for the rewarming of cryopreserved biological material.* IEEE Transactions on Ultrasonics, Ferroelectrics, and Frequency Control, 2020. **68**(3): p. 599-607.
32. Brockbank, K.G., et al., *Ice control during cryopreservation of heart valves and maintenance of post-warming cell viability.* Cells, 2022. **11**(12): p. 1856.
33. Brockbank, K.G., et al., *Vitrification of heart valve tissues.* Cryopreservation and freeze-drying protocols, 2015: p. 399-421.
34. Zhan, L., et al., *Rapid joule heating improves vitrification based cryopreservation.* Nature communications, 2022. **13**(1): p. 6017.
35. Han, H., et al., *Investigation of rapid rewarming chips for cryopreservation by joule heating.* Langmuir, 2023. **39**(31): p. 11048-11062.
36. Han, Z., et al., *Diffusion Limited Cryopreservation of Tissue with Radiofrequency Heated Metal Forms.* Advanced healthcare materials, 2020. **9**(19): p. 2000796.
37. Gangwar, L., et al., *Perspective: A Guide to Successful ml to L Scale Vitrification and Rewarming.* CryoLetters, 2022. **43**(6): p. 303-315.
38. Shore, D., et al., *Nanowarming using Au-tipped Co 35 Fe 65 ferromagnetic nanowires.* Nanoscale, 2019. **11**(31): p. 14607-14615.

39. Pasek-Allen, J.L., et al., *Phosphonate coating of commercial iron oxide nanoparticles for nanowarming cryopreserved samples.* Journal of Materials Chemistry B, 2022.
40. Wakabayashi, T., et al., *Nanowarming of vitrified pancreatic islets as a cryopreservation technology for transplantation.* Bioengineering & Translational Medicine, 2023. **8**(4): p. e10416.
41. Chiu-Lam, A., et al., *Perfusion, cryopreservation, and nanowarming of whole hearts using colloidally stable magnetic cryopreservation agent solutions.* Science advances, 2021. **7**(2): p. eabe3005.
42. Sharma, A., et al., *Vitrification and Nanowarming of Kidneys.* Advanced Science, 2021. **8**(19): p. 2101691.
43. Sharma, A., et al., *Cryopreservation of whole rat livers by vitrification and nanowarming.* Annals of Biomedical Engineering, 2023. **51**(3): p. 566-577.
44. Chen, P., et al., *Nanowarming and ice-free cryopreservation of large sized, intact porcine articular cartilage.* Communications Biology, 2023. **6**(1): p. 220.
45. Pan, J., et al., *Investigation of electromagnetic resonance rewarming enhanced by magnetic nanoparticles for cryopreservation.* Langmuir, 2018. **35**(23): p. 7560-7570.
46. Ren, S., et al., *Single-mode electromagnetic resonance rewarming for the cryopreservation of samples with large volumes: A numerical and experimental study*. Biopreservation and Biobanking, 2022. **20**(4): p. 317-322.
47. Rajotte, R., et al., *Preservation studies on canine kidneys recovered from the deep frozen state by microwave thawing.* Proceedings of the IEEE, 1974. **62**(1): p. 76-85.
48. Wowk, B., et al., *27 MHz constant field dielectric warming of kidneys cryopreserved by vitrification.* Cryobiology, 2024. **115**: p. 104893.
49. Ruggera, P.S. and G.M. Fahy, *Rapid and uniform electromagnetic heating of aqueous cryoprotectant solutions from cryogenic temperatures.* Cryobiology, 1990. **27**(5): p. 465-478.
50. Gao, Z., et al., *Preparation of Scalable Silica-Coated Iron Oxide Nanoparticles for Nanowarming.* Advanced Science, 2020. **7**(4): p. 1901624.
51. Lee, S.G., et al., *Development of heart organoid cryopreservation method through Fe3O4 nanoparticles based nanowarming system.* Biotechnology Journal, 2023: p. 2300311.
52. Karimi, S., et al., *Nanowarming improves survival of vitrified ovarian tissue and follicular development in a sheep model.* Heliyon, 2023. **9**(8).
53. Han, Z., et al., *Vitrification and nanowarming enable long-term organ cryopreservation and life-sustaining kidney transplantation in a rat model.* Nature Communications, 2023. **14**(1): p. 3407.
54. Gao, Z., et al., *Vitrification and rewarming of magnetic nanoparticle-loaded rat hearts.* Advanced Materials Technologies, 2022. **7**(3): p. 2100873.
55. Zhan, T., et al., *Fe3O4 nanoparticles with carboxylic acid functionality for improving the structural integrity of whole vitrified rat kidneys.* ACS Applied Nano Materials, 2021. **4**(12): p. 13552-13561.
56. Etheridge, M. and J. Bischof, *Optimizing magnetic nanoparticle based thermal therapies within the physical limits of heating.* Annals of biomedical engineering, 2013. **41**: p. 78-88.
57. Gangwar, L., et al., *When will nanowarmed organs crack? A preliminary 1-D model.* Cryobiology, 2020. **97**: p. 271.
58. Zlokovic, B., *Blood–Brain Barrier and Neurovascular Mechanisms of Neurodegeneration and Injury.* 2009.
59. Rakusan, K., et al., *Morphometry of human coronary capillaries during normal growth and the effect of age in left ventricular pressure-overload hypertrophy.* Circulation, 1992. **86**(1): p. 38-46.

60. Bosch, A., et al., *Retinal capillary and arteriolar changes in patients with chronic kidney disease*. Microvascular Research, 2018. **118**: p. 121-127.
61. Sarveswaran, K., et al., *Synthetic capillaries to control microscopic blood flow*. Scientific reports, 2016. **6**(1): p. 21885.
62. Marsland, T., S. Evans, and D. Pegg, *Dielectric measurements for the design of an electromagnetic rewarming system.* Cryobiology, 1987. **24**(4): p. 311-323.
63. Robinson, M.P., et al., *Electromagnetic re-warming of cryopreserved tissues: effect of choice of cryoprotectant and sample shape on uniformity of heating.* Physics in Medicine & Biology, 2002. **47**(13): p. 2311.
64. Wusteman, M., M. Robinson, and D. Pegg, *Vitrification of large tissues with dielectric warming: biological problems and some approaches to their solution.* Cryobiology, 2004. **48**(2): p. 179-189.
65. Evans, S., *Electromagnetic rewarming: the effect of CPA concentration and radio source frequency on uniformity and efficiency of heating.* Cryobiology, 2000. **40**(2): p. 126-138.
66. Luo, D., et al., *Development of a single mode electromagnetic resonant cavity for rewarming of cryopreserved biomaterials.* Cryobiology, 2006. **53**(2): p. 288-293.
67. Hijnen, N.M., et al., *Tumour hyperthermia and ablation in rats using a clinical MR-HIFU system equipped with a dedicated small animal set-up.* International journal of hyperthermia, 2012. **28**(2): p. 141-155.
68. Kovatcheva, R., et al., *US-guided high-intensity focused ultrasound as a promising non-invasive method for treatment of primary hyperparathyroidism.* European radiology, 2014. **24**: p. 2052-2058.
69. Izadifar, Z., et al., *An introduction to high intensity focused ultrasound: systematic review on principles, devices, and clinical applications.* Journal of clinical medicine, 2020. **9**(2): p. 460.
70. Encabo, L., et al., *HIFU Rewarming of Organs After Cold Preservation: Ex Vivo Assessment of Heart Performance in Murine Model.* Transplantation, 2024. **108**(1): p. e15-e17.
71. Xu, R., B.E. Treeby, and E. Martin, *Experiments and simulations demonstrating the rapid ultrasonic rewarming of frozen tissue cryovials.* The Journal of the Acoustical Society of America, 2023. **153**(1): p. 517-528.
72. Ecker, H., E. Burdette, and F. Cain. *Simultaneous microwave and high frequency thawing of cryogenically preserved canine kidneys*. in *Record of the IEEE International Symposium on Electromagnetic Compatibility*. 1976.

# Chapter 2. Review on Thermophysical Properties Measurement for biological materials-CPAs, Tissues, and CPA permeated Tissues

This chapter presents the literature review of measurement techniques and property values for thermal properties of various biological materials mainly cryoprotective agents (CPAs), tissues, and CPA equilibrated tissues. The contents of this chapter are taken from a manuscript in preparation.

# Overview

Thermophysical properties such as thermal conductivity, specific heat capacity, density, etc. govern the thermal response of a biomaterial undergoing temperature change such as during cooling and rewarming in cryopreservation. These thermophysical properties are crucial input parameters in numerical modeling prediction of temperature profiles, cooling and warming rates. We provide a brief compilation of thermal conductivity values for CPAs, tissues (animal and human) and CPA permeated tissues from literature. Furthermore, other thermal properties such as specific heat, density and coefficient of thermal expansion for common organ vitrification CPAs are briefly discussed. It is observed that the thermal properties vary among tissues, CPAs and CPA permeated tissues depending upon thermal history (vitrified vs. crystallized), interaction of CPA with tissue content (water, proteins, etc.) and cryogenic temperature as some of factors. Lastly, there exists a gap and unmet need in measurement of thermal properties for CPA permeated tissues specifically in cryogenic temperatures which are most relevant for modeling vitrification and rewarming of cryopreserved biomaterials.

# Introduction

The thermal properties of CPAs and tissues are key factors in modeling the thermal response during cooling or nanowarming in cryopreservation. Using thermophysical properties that govern heat flow, such as specific heat, thermal conductivity, etc., temperature distribution can be predicted inside a biomaterial. Firstly, thermal properties determine thermal response during nanowarming, especially how fast heat diffuses from the nanoparticle location throughout the organ. Secondly, knowing the accurate thermal properties of CPAs and CPA-permeated tissues is important in calculating SAR from measured heating rates of IONP samples, as SAR is directly proportional to specific heat capacity ($C_P$) and density ($\rho$). Specific heat decreases at cryogenic temperatures, which implies that heat from nanoparticles diffuses faster at those lower temperatures, especially in the glassy region (below $T_g$), where specific heat decreases significantly (from ~3500 J/kg.K to ~1500 J/kg.K), as reported in the literature for CPAs M22, DP6, and VS55 [1]. Thermal conductivity (k) has also been reported for popular CPAs whose vitrified state has similar values as the liquid state (~0.3 W/m.K for M22, VS55, DP6) [2], and the k value increases if ice crystallization occurs inside the CPA [3]. Note that there is limited information in the literature about the thermal properties of tissues permeated with common CPAs, but usually numerical studies have assumed CPA's thermal properties for an organ with the assumption of complete equilibration of tissue inside an organ with the perfused CPA [4, 5] which is a limitation [6].

## Thermal Conductivity of CPAs, Tissues

Measurement of thermal conductivity has been an important question relevant for mechanical (thermal sciences) and biomedical engineers for a long time [7] as thermal measurement of such properties allows predicting and modeling the thermal behavior of a biomaterial such as tissue undergoing thermal cycling for applications such as cryopreservation or cryodestruction (cryotherapy treatment for cardiovascular and oncological diseases). Both cryopreservation and cryosurgery require adequate knowledge of thermal history of a biomaterial (tissue) in order to preserve or destroy the biomaterial respectively. Mathematical modeling is one approach to identify freezing of biological tissues and knowledge of thermophysical properties such as thermal conductivity at low temperature is crucial for cryopreservation/cryotherapy-based treatments. Thermal conductivity is not only affected by temperature, but also by tissue type since each tissue differs in composition (quantity of water, fat, etc.), humidity, density etc.

Even though one can find significant number of literature (original research articles, review articles and property database such as ITIS tissue property) on thermal conductivity of a biomaterial, but most of them are restricted to suprazero (> 0°C) temperature range [7-12] thereby lacking cryogenic application such as cryopreservation. As we narrow down the literature search on subzero and cryogenic temperature dependence of biomaterial thermal conductivity, very few of them (~5) satisfy that temperature criterion [3, 13-16]. For instance, the review Choi et. al. [3] which is more than a decade old literature doesn't contain relevant cryoprotective agents (CPAs) which are proposed for organ cryopreservation and a comprehensive human tissue in their low temperature thermal conductivity database. Hence there is an unmet need to compile a thermal conductivity database in low temperature i.e. subzero (0°C to -30°C) and cryogenic temperature (<-30°C) ranges for biomaterial (tissues), solutions relevant for cryotherapy (cryopreservation) such as cryoprotective agents and the combination of both. Here we provide the most recent thermal property database in cryogenic temperature range for various tissue and CPA types particularly including commonly used CPA cocktails, human tissues and animal tissues equilibrated with CPAs.

A common way to measure thermal conductivity involves a thermal or electrical heat source applied to a bio-sample of interest whose temperature change is directly or indirectly measured. This temperature variation information is usually fed to a heat transfer model where thermal conductivity is calculated from the governing heat equation of the system with applied or observed boundary conditions as shown in Figure 2.1. Several measurement techniques exist (thermal comparator, transient hot wire method, chato's probe, pulse decay thermistor, 3ω technique,

thermal needle probe, etc to name few) which can be chosen based upon factors such as sample thickness/size, state- solid vs liquid, invasive, in-vitro, commercial availability, etc. and can be read in more detail in literature [3].

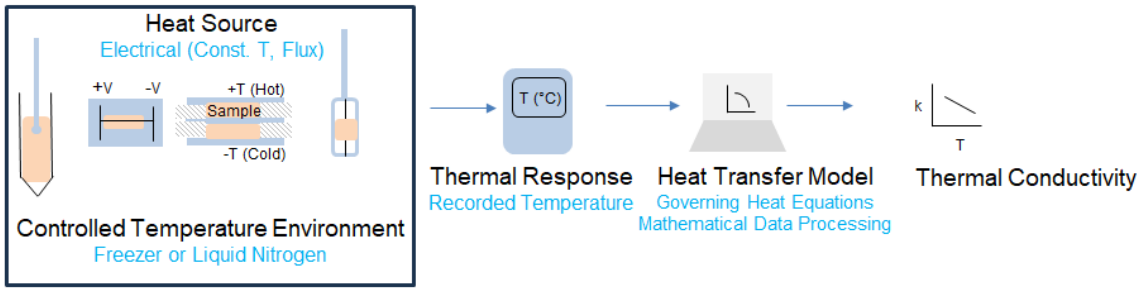


Figure 2.1 Sequential flow of thermal conductivity measurement of CPAs, tissues at low/cryogenic temperature.

Figure 2.2 provides a summary plot of thermal conductivity of tissues, CPAs, and CPA permeated tissues. Thermal conductivity is reported to be varied with temperature for tissues which is mainly due to amount of water being frozen into ice which contributes to increase in thermal conductivity values. For CPA or tissue, the state of material i.e. vitrified vs. crystalline affect thermal conductivity. It is also observed that thermal conductivity differs between CPA and tissue equilibrated with CPA (e.g. ~10% for liver+glycerol). This study provides comprehensive thermal conductivity values for various tissue types such as rabbit, porcine and more importantly human as well as popular CPA cocktails such as VS55, DP6, M22, etc.

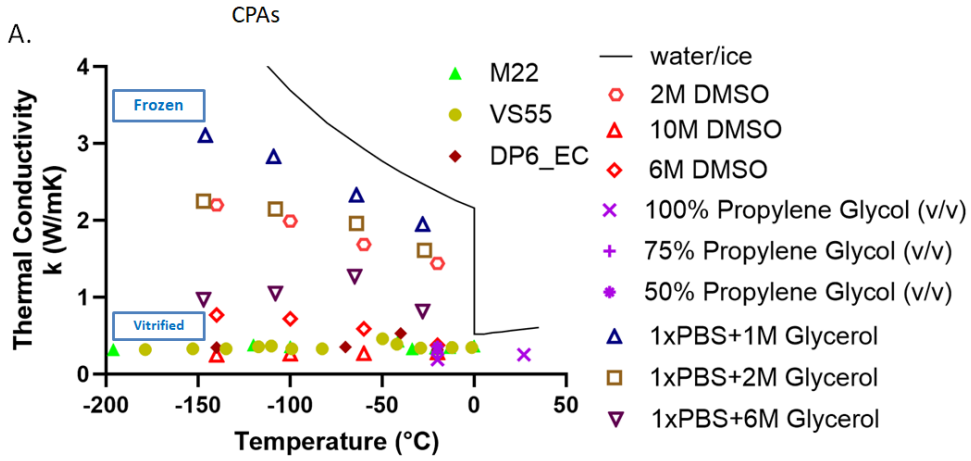

B. Animal Tissues

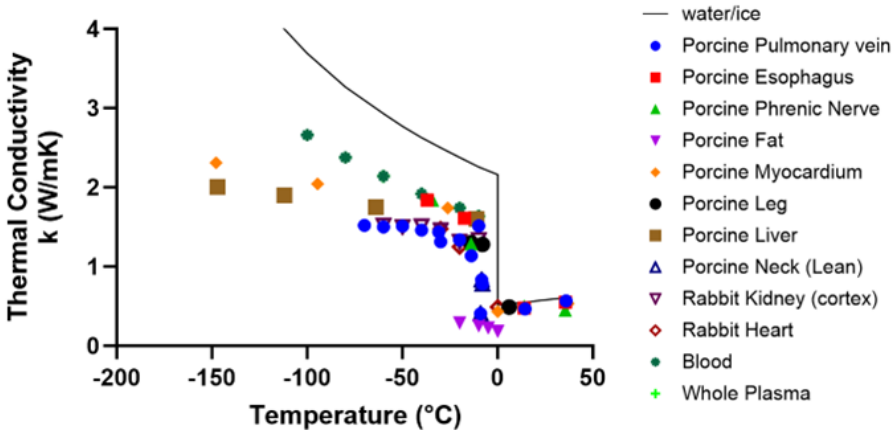


C. Human Tissues

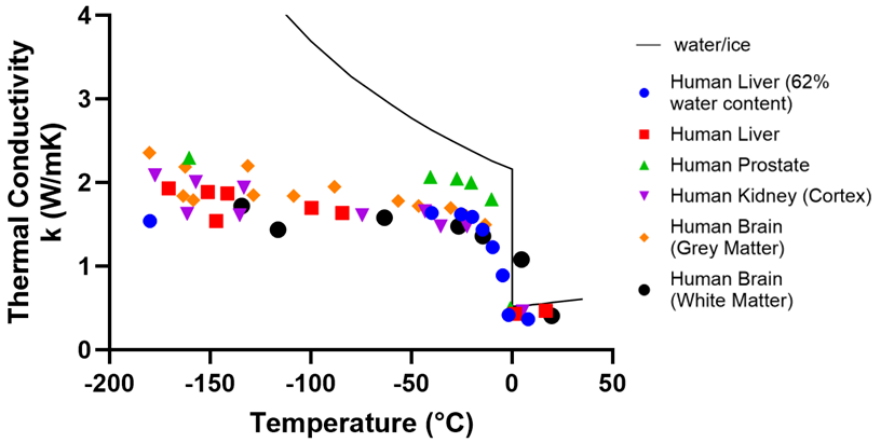

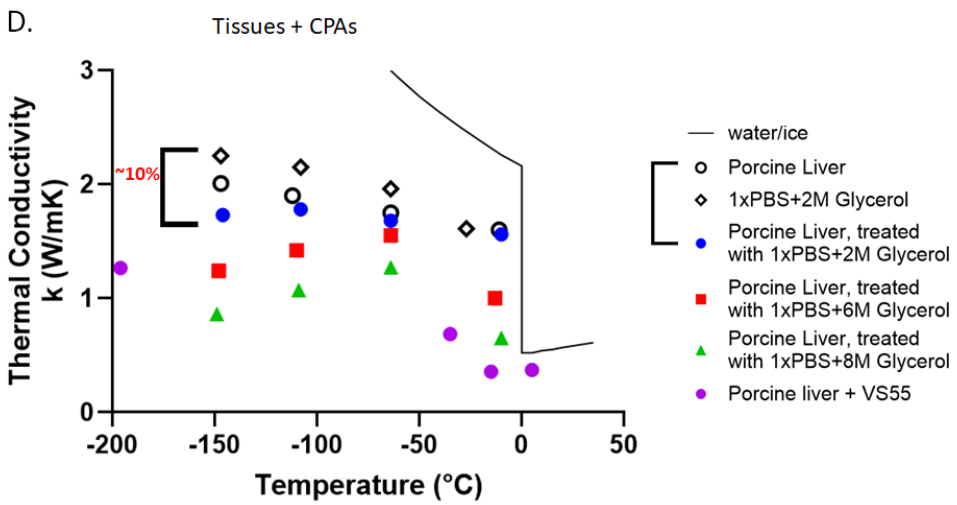


Figure 2.2 Thermal conductivity (k) of biological materials relevant for cryopreservation. k vs Temperature for A. CPAs, B. Animal tissues, C. Human tissues, and D. CPA permeated tissues compiled from literature. Data values are compiled for water/ice from [17], CPAs from [2, 6, 18-20], animal tissues from [6, 13, 15, 16, 21-25], human tissues from [13, 26] and CPA permeated tissues from [6, 15]. See Table A1.1-A1.4 in Appendix 1 for data values.

## Specific Heat Capacity of CPAs and tissues

Specific heat capacity at constant pressure ($C_p$) is another important thermal property which governs the energy storage inside a material. Specific heat is usually measured using a calorimetric device such as a differential scanning calorimeter (DSC). Specific heat for various tissue types have been measured though only at room temperature [9, 12]. For CPAs and CPA permeated tissues, the specific heat values are limited in literature and often been reported as weighted average of consitutents which is not necesarily true [27, 28]. Specific heat capacity of CPAs such as glycerol and propylene glycol in glassy state was measured to decrease signficantly after glass formation many decades ago [29]. More recently, specific heat of common organ vitrification CPAs such as M22, VS55, DP6 as function of cryogenic temperature have been reported [1, 3]. M22 seems to have the highest heat capacity (~3500 J/g.K) at room temeprature which drops down drastically below glass transiton temperature (~1500 J/g.K) whereas VS55, DP6 whose $C_p$ values drop from ~3000 to ~1100 J/g.K below glass transition (see Figure 2.3A) [1]. The specific heat capacity values for tissues and CPA permeated tissues in cryogenic temperaure still remain largely unavailable (see Table A1.7 in Appendix 1).

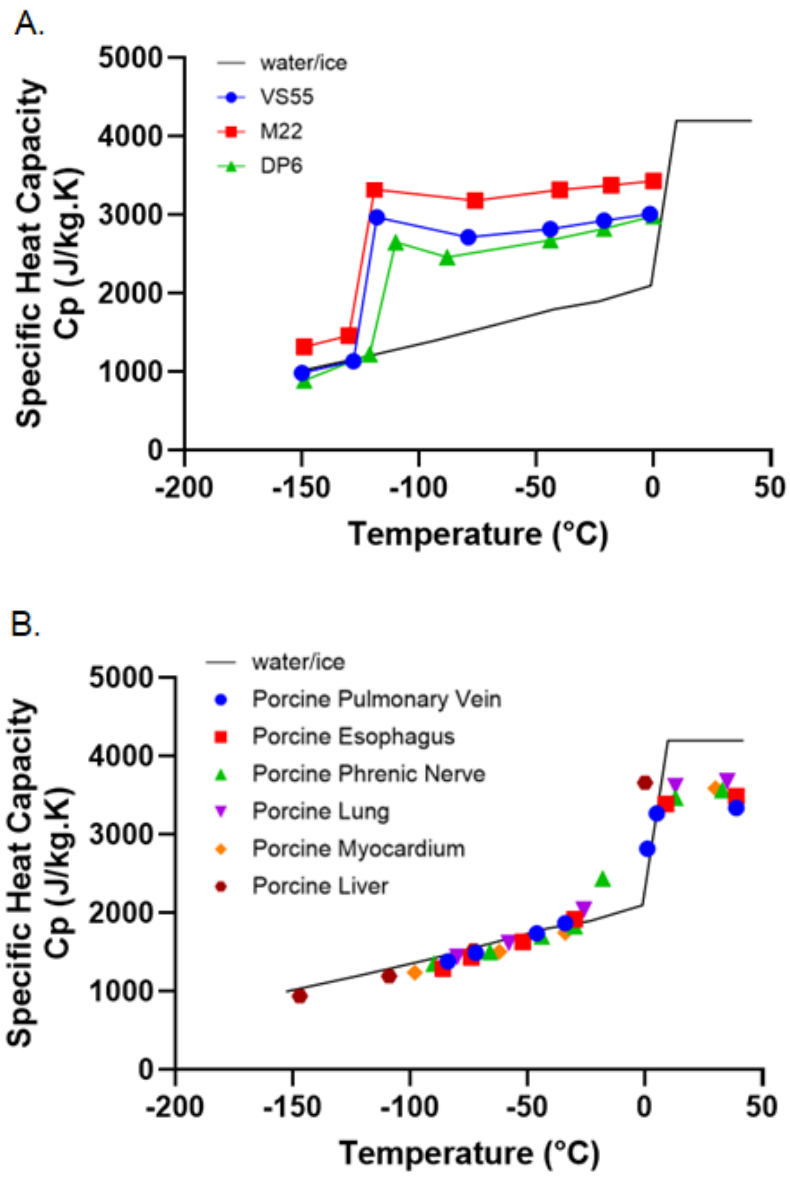


Figure 2.3 Specific heat of A. CPAs and B. tissues in cryogenic temperatures compiled from literature. See Table A1.5-A1.7 in Appendix 1 for comprehensive data values.

## Density and thermal expansion of CPAs and tissues

Density is another thermophysical property which plays an important role in buoyancy driven natural heat convection in fluids and material deformation in solids. During cryopreservation, CPA is going from a fluid state to a solid-glassy state. Tissues permeated with CPAs behave more like solids once vitrified and therefore are subjected to thermal stress induced fractures. The coefficient of thermal expansion, which is a derived property of material density, governs, for instance,

whether thermal stresses can cause a fracture in a vitrified organ. Using thermomechanical properties (thermal expansion coefficient of material, Poisson's ratio, Young modulus) and temperature gradients across the sample, fracture or physical cracking/fractures inside an organ during rewarming and cooling can be predicted by comparing thermal stress to the tensile yield strength of material as given in [30] thermal shock equation. Coefficient of thermal expansion can be usually measured through a uniaxial tensile test for solids or by measuring pressure response to the changing volume of fluid, in a closed system for tissues permeated with CPAs [31]. Density and coefficient of thermal expansion of a CPA can increase upto ~7% (for M22) from room temperature to cryogenic temperature (see Figure 2.4) [32]. Further these properties also increase ~4-7% in CPA permeated tissues compared to CPA solution alone density values, a comprehensive summary of density and thermal expansion can be found elsewhere [32-34].

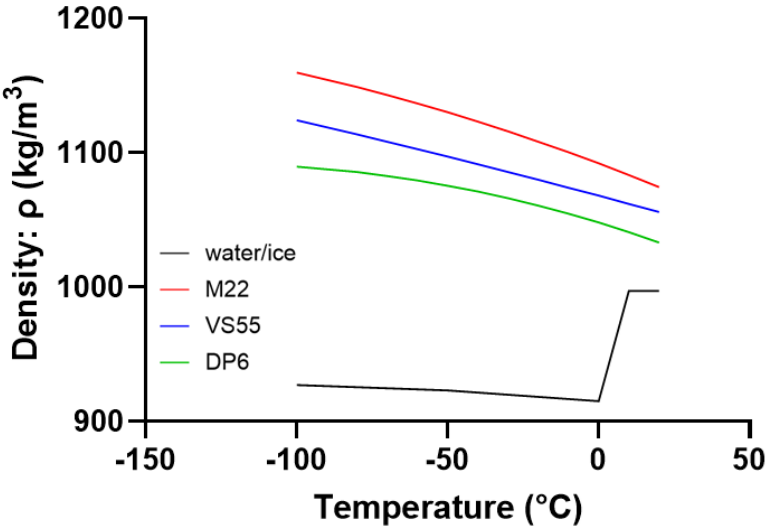


Figure 2.4 Reprensetative plot of density vs. temperature for CPAs plotted using literature data values from [32] for CPAs and [35] for water/ice.

# References For Chapter 2


1. Phatak, S., et al., *Measurement of specific heat and crystallization in VS55, DP6, and M22 Cryoprotectant systems with and without sucrose.* Biopreservation and Biobanking, 2018. **16**(4): p. 270-277.
2. Ehrlich, L.E., et al., *Thermal conductivity of cryoprotective agents loaded with nanoparticles, with application to recovery of preserved tissues and organs from cryogenic storage.* Plos one, 2020. **15**(9): p. e0238941.

3. Choi, J. and J.C. Bischof, *Review of biomaterial thermal property measurements in the cryogenic regime and their use for prediction of equilibrium and non-equilibrium freezing applications in cryobiology.* Cryobiology, 2010. **60**(1): p. 52-70.
4. Ehrlich, L.E., et al., *Thermal Analyses of a Human Kidney and a Rabbit Kidney During Cryopreservation by Vitrification.* Journal of biomechanical engineering, 2018. **140**(1): p. 0110051-0110058.
5. Joshi, P., et al., *Thermal Analyses of Nanowarming-Assisted Recovery of the Heart From Cryopreservation by Vitrification.* Journal of Heat Transfer, 2022. **144**(3): p. 031202.
6. Choi, J.H. and J.C. Bischof, *A quantitative analysis of the thermal properties of porcine liver with glycerol at subzero and cryogenic temperatures.* Cryobiology, 2008. **57**(2): p. 79-83.
7. Bowman, H.F., E.G. Cravalho, and M. Woods, *Theory, measurement, and application of thermal properties of biomaterials.* Annual review of biophysics and bioengineering, 1975. **4**(1): p. 43-80.
8. Lipkin, M. and J.D. Hardy, *Measurement of some thermal properties of human tissues.* Journal of applied physiology, 1954. **7**(2): p. 212-217.
9. Mcintosh, R.L. and V. Anderson, *A comprehensive tissue properties database provided for the thermal assessment of a human at rest.* Biophysical Reviews and Letters, 2010. **5**(03): p. 129-151.
10. Valvano, J.W., J. Cochran, and K.R. Diller, *Thermal conductivity and diffusivity of biomaterials measured with self-heated thermistors.* International Journal of Thermophysics, 1985. **6**: p. 301-311.
11. Bhattacharya, A. and R.L. Mahajan, *Temperature dependence of thermal conductivity of biological tissues.* Physiological measurement, 2003. **24**(3): p. 769.
12. Giering, K., et al., *Review of thermal properties of biological tissues*. 1995: Bellingham, WA: SPIE Opt. Eng. Press.
13. Tsiganov, D., *Cryomedicine: processes and apparatus.* SAYNS-PRESS, Moscow, 2011: p. 304.
14. Natesan, H. and J.C. Bischof, *Multiscale Thermal Property Measurements for Biomedical Applications.* ACS Biomaterials Science & Engineering, 2017. **3**(11): p. 2669-2691.
15. Jiang, Z., et al., *Coupled experimental-modeling analyses of heat transfer in ex-vivo VS55-perfused porcine hepatic tissue being plunged in liquid nitrogen for vitreous cryopreservation.* International Journal of Heat and Mass Transfer, 2017. **106**: p. 970-979.
16. Agafonkina, I., et al., *Thermal properties of human soft tissue and its equivalents in a wide low-temperature range.* Journal of Engineering Physics and Thermophysics, 2021. **94**: p. 233-246.
17. Bald, W. and J. Fraser, *Cryogenic surgery.* Reports on Progress in Physics, 1982. **45**(12): p. 1381.
18. Ehrlich, L.E., et al., *Large thermal conductivity differences between the crystalline and vitrified states of DMSO with applications to cryopreservation.* PLoS One, 2015. **10**(5): p. e0125862.
19. Ehrlich, L.E., J.A. Malen, and Y. Rabin, *Thermal conductivity of the cryoprotective cocktail DP6 in cryogenic temperatures, in the presence and absence of synthetic ice modulators.* Cryobiology, 2016. **73**(2): p. 196-202.
20. Li, Y., et al., *Measurement of thermal conductivities of two cryoprotective agent solutions for vitreous cryopreservation of organs at the temperature range of 77 K–300 K using a thermal sensor made of microscale enamel copper wire.* Biopreservation and Biobanking, 2017. **15**(3): p. 228-233.
21. Rinfret, A., *Factors affecting the erythrocyte during rapid freezing and thawing.* Annals of the New York Academy of Sciences, 1960. **85**(2): p. 576-594.

22. Xie, H. and S. Cheng, *A fine needle probe for determining the thermal conductivity of penetrable materials.* Measurement Science and Technology, 2001. **12**(1): p. 58.
23. Lubner, S.D., et al., *Reusable bi-directional 3 ω sensor to measure thermal conductivity of 100-μ m thick biological tissues.* Review of Scientific Instruments, 2015. **86**(1): p. 014905.
24. Cherneeva, L., *Study of thermal properties of foods.* Report of Vnikhi (Scientific Research Institute of the Refrigeration Industry), Gostorgisdat, Moscow, 1956.
25. Chato, J. *Thermal Problems in Biotechnology*. in *ASME*. 1968.
26. I., M.E., *THERMAL CONDUCTIVITY OF BIOLOGICAL TISSUES IN THE DOMAIN OF WATER CHANGE OF PHASE.* 1984, Kholodilnaya Tekhnika- n. 4.
27. Bianchi, L., et al., *Thermophysical and mechanical properties of biological tissues as a function of temperature: a systematic literature review.* International Journal of Hyperthermia, 2022. **39**(1): p. 297-340.
28. Chato, J.C., *Measurement of thermal properties of biological materials.* Heat transfer in medicine and biology: analysis and applications, 1985. **1**: p. 167-192.
29. Birge, N.O., *Specific-heat spectroscopy of glycerol and propylene glycol near the glass transition.* Physical Review B, 1986. **34**(3): p. 1631.
30. Steif, P.S., M.C. Palastro, and Y. Rabin, *The effect of temperature gradients on stress development during cryopreservation via vitrification.* Cell preservation technology, 2007. **5**(2): p. 104-115.
31. Eisenberg, D.P., M.J. Taylor, and Y. Rabin, *Thermal expansion of the cryoprotectant cocktail DP6 combined with synthetic ice modulators in presence and absence of biological tissues.* Cryobiology, 2012. **65**(2): p. 117-125.
32. Solanki, P.K. and Y. Rabin, *Perspective: Temperature-Dependent Density And Thermal Expansion Of Cryoprotective Agents.* CryoLetters, 2022. **43**(1): p. 1-9.
33. Rios, J.L.J. and Y. Rabin, *Thermal expansion of blood vessels in low cryogenic temperatures, Part II: Vitrification with VS55, DP6, and 7.05 M DMSO.* Cryobiology, 2006. **52**(2): p. 284-294.
34. Y, R. and P. J, *Thermal expansion of blood vessels and muscle specimens permeated with DMSO, DP6, and VS55 at cryogenic temperatures.* Annals of biomedical engineering, 2005. **33**(9).
35. Fukusako, Shoichiro, *Thermophysical properties of ice, snow, and sea ice*. International Journal of Thermophysics 11 1990: 353-372.

# Chapter 3. Thermal Modeling to predict the limits for bulk vitrification

This chapter presents the computational heat transfer modeling predictions for success and failure (ice formation and fracture) from mL to Liter scale samples. This body of work has been published as an article in Cryoletters. The publication is reproduced here:

- **Gangwar, Lakshya**, et al. "Perspective: A Guide to Successful ml to L Scale Vitrification and Rewarming." CryoLetters 43.6 (2022): 303-315.

# Overview

Cryopreservation by vitrification to achieve an “ice free” glassy state is an effective technique for preserving biomaterials including cells, tissues, and potentially even whole organs. The major challenges in cooling to and rewarming from a vitrified state remain ice crystallization and cracking/fracture. Ice crystallization can be inhibited by the use of cryoprotective agents (CPAs) though the inhibition further depends upon the rates achieved during cooling and rewarming. The minimal rate required to prevent any ice crystallization or recrystallization in a given CPA is called the critical cooling rate (CCR) or critical warming rate (CWR), respectively. On the other hand, physical cracking is mainly related to thermomechanical stresses, which can be avoided by maintaining temperature differences below a critical threshold. Here we use thermal modeling to help us understand the magnitude and trajectory of these challenges as we scale the biomaterial volume for a given CPA from the milliliter to liter scale. First, we solved the governing heat transfer equations in a cylindrical geometry for three common vitrification cocktails (i.e., VS55, DP6, and M22) to estimate the cooling and warming rates during convective cooling, warming and nanowarming (volumetric heating). Second, we estimated the temperature difference ($\Delta T$) and compared it to a tolerable threshold ($\Delta T_{max}$) based on a simplified “thermal shock” equation for the same cooling and rewarming conditions. Not surprisingly, we found that M22 achieves vitrification more easily during convective cooling and rewarming for all volumes compared to VS55 or DP6 due to its considerably lower CCR and CWR. Further, convective rewarming (boundary rewarming) leads to larger temperature differences and smaller rates compared to nanowarming (volumetric rewarming) for all CPAs with increasing failure at larger volumes. As more and larger systems are vitrified and rewarmed with standard CPA cocktails, this work provides a practical guide to successful implementation based on the characteristic length (Volume/Surface Area) of the system and the specific conditions of cooling and warming.

**Nomenclature**

| | |
|---|---|
| $L_c$ | Characteristic length (cm) |
| $D$ | Diameter of the geometry (cm) |
| $h$ | Effective heat transfer coefficient (W/m$^{2}$-°C) |
| $T_{cool}$ | Ambient temperature for convective cooling (°C) |
| $T_{warm}$ | Ambient temperature for convective warming (°C) |
| $C_P$ | Specific heat at constant pressure (J/kg-°C) |
| $\Delta T$ | Temperature difference between center & edge (°C) |
| $q_V^{'''}$ | Volumetric heat generation (source) term (W/m$^{3}$) |
| *CPA* | Cryoprotective agent |
| *CCR* | Critical cooling rate (°C/min) |
| *CWR* | Critical warming rate (°C/min) |
| $SAR_{Fe}$ | Specific absorption rate (W/gFe) |

**Greek Symbols**

| | |
|---|---|
| ß | Coefficient of linear thermal expansion (1/°C) |
| $\rho$ | Density (kg/m$^{3}$) |
| σ | Thermal stress (MPa) |

**Subscripts**

| | |
|---|---|
| *Center* | center of geometry |
| *Edge* | edge of geometry |

# Introduction

Cryopreservation by vitrification has been increasingly studied in various biomaterials, including cells, tissues, organs, and organisms, since the first practical demonstrations in the 1980s [1, 2] [3, 4] [5–7] [8, 9]. Vitrification involves rapidly cooling a sample to below its glass transition temperature (Tg) to surpass significant ice crystallization (ice nucleation and growth) and form a glassy (amorphous) state [4, 10]. The cooling rate required to achieve the vitrified state should be at least higher than the critical cooling rate (CCR), which is defined as the minimum rate needed to avoid any significant ice crystallization (such as ice formation restricted to 0.2% of solution mass) [11]. Similarly, the rewarming rate should be greater than the critical warming rate (CWR) to prevent devitrification and/or ice recrystallization. Here, practical vitrification success is usually assumed if the ice can be confined to less than 0.2–0.5% of solution mass [7, 12]. Perhaps most importantly, once vitrified, a biomaterial can in theory be stored in this state indefinitely as metabolism effectively ceases at cryogenic temperatures.

Vitrification has been demonstrated and applied successfully in a variety of systems ranging from embryos [13] to rabbit kidneys since 1984 [4] but rewarming from a vitrified state remains the major hurdle in successful cryopreservation, especially in larger volume systems [14]. For instance, convectively vitrified rabbit kidneys have only been rewarmed successfully once in the past [14], suggesting scale up for larger volumes such as human organs by convection alone will be difficult or impossible. Nanowarming is an emerging volumetric rewarming technology that may address this limitation through the use of radiofrequency-activated magnetic nanoparticles (e.g., iron-oxide nanoparticles IONPs). These IONPs can be perfused throughout the organ vasculature prior to vitrification and heated by magnetic hysteresis losses in the presence of an alternating magnetic field generated by a radiofrequency coil [15, 16]. Recent studies in organs such as rat kidneys and hearts have shown promising results in terms of achieving rapid heating rates (~60°C/min and ~70°C/min) uniformly throughout the organ [17–19]. This effectively changes the paradigm from failures most commonly occurring during warming to failures now during cooling when working at human organ scales [20]. This failure can occur due to slow rates (i.e., cooling rate < CCR) and excessive thermomechanical stresses induced by cooling restricted to the edges of the container. Both of these issues are being actively investigated by careful analysis of human-scale kidney cooling and assessing the benefits of different containers to avoid stress accumulation, i.e., cryobags with expandable boundaries [21] [22, 23].

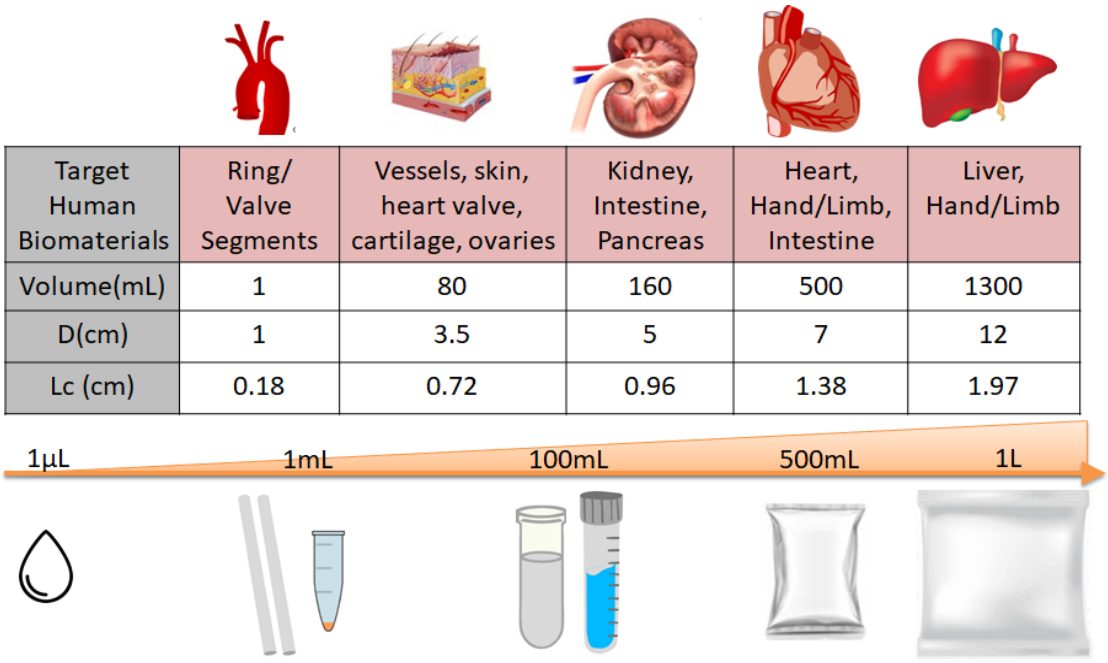


| Target Human Biomaterials | Ring/ Valve Segments | Vessels, skin, heart valve, cartilage, ovaries | Kidney, Intestine, Pancreas | Heart, Hand/Limb, Intestine | Liver, Hand/Limb |
|---|---|---|---|---|---|
| Volume(mL) | 1 | 80 | 160 | 500 | 1300 |
| D(cm) | 1 | 3.5 | 5 | 7 | 12 |
| Lc (cm) | 0.18 | 0.72 | 0.96 | 1.38 | 1.97 |

Figure 3.1. Representative dimensions and the corresponding characteristic length scales for common bulk systems that undergo vitrification.

While many previous studies have focused on assessing vitrification success and failure in systems of various sizes, we have not found a clear, practical guide for vitrification in bulk systems that can help guide convection or nanowarming choices to achieve the necessary CCR and CWR and avoid thermal stress–generated cracks. Here we provide practical guidance on how to avoid ice formation as well as thermal stress–induced fractures, using several convective cooling and rewarming boundary conditions. In the case of nanowarming, iron oxide nanoparticles (IONPs) are assumed to be distributed throughout the modeled geometry with a constant heat generation per mg Fe [24]. Correlations for cooling and warming rates and temperature differences ($\Delta T$) as a function of the experimental conditions (i.e., characteristic length, convective condition, and CPA choice—VS55, M22, or DP6) have been derived. In summary, this work provides simple guidance on how to achieve vitrification success for given experimental conditions.

## Materials and Methods

A 2-D axisymmetric, finite cylindrical geometry is assumed for the bulk biomaterial undergoing cryopreservation. Heat transfer inside the geometry is assumed to occur primarily through conduction due to the very high viscosity of CPAs at cryogenic temperatures (i.e., the domain is assumed to be a solid in modeling) [25]. Five different volumes of finite cylinders are analyzed,

ranging from 1mL to >1L relevant to different biomaterial sizes, with varying diameters and heights, as listed in Figure 3.1. Characteristic length (Lc) is computed for each volume as the ratio of volume to total surface area of the cylinder. Equation 3.1 is the general form of the governing equation for the model, and additional details about boundary conditions, initial conditions, and non-homogenous terms are further provided in Table 3.1 and Figure 3.2. The geometry (containing the biological material such as organs, tissues, etc.) is assumed to be fully equilibrated with the CPA, so properties are assumed to be uniform. The thermal and mechanical properties of each CPA are assigned to the geometry as listed in Table 3.2. A finite element analysis (FEA) was performed in the commercial package COMSOL 5.4 using the heat transfer module to solve the governing heat equation for the defined geometry. Domain point probes were attached at the center (r, z = 0) and edge (defined as 10% of the distance from the boundary in order to avoid immediate edge effects at the convective boundary).

Three different cases were analyzed for each given volume, namely convective cooling, convective warming, and nanowarming, as shown in Figure 2. Further, each case was simulated for three

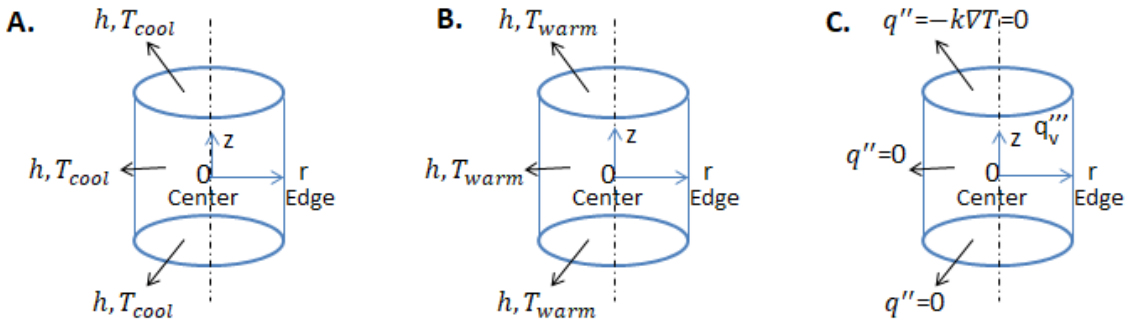


Figure 3.2. Schematic of modeled cylindrical geometry in FEA for (A.) convective cooling, (B.) convective warming, and (C.) nanowarming, depicting corresponding boundary conditions

common CPAs, VS55, DP6, and M22 [13, 26, 28], resulting in nine numerical temperature solutions for a given volume (for a total of 9×5 = 45 numerical simulations for five different volumes ranging from mL to L range in this study).

$$\rho C_P \frac{\partial T}{\partial t} = \frac{1}{\mathrm{r}}\frac{\partial}{\partial \mathrm{r}}\left(kr\frac{\partial T}{\partial r}\right) + \frac{\partial}{\partial \mathrm{z}}\left(k\frac{\partial T}{\partial z}\right) + q_v''' \quad (3.1)$$

Table 3.1. Governing equations, boundary conditions, and initial conditions simulated for all three different cases analyzed in this study and relevant to cryopreservation by vitrification.

| Case | Convective Cooling | Convective Warming | Nanowarming |
|---|---|---|---|
| Governing Equation | $q_v''' = 0$ | $q_v''' = 0$ | $q_v''' = SAR_{Fe} * C_{Fe}$ |
| Initial Condition | $\mathrm{T} = 0°\mathrm{C}$ | $\mathrm{T} = -150°\mathrm{C}$ | $\mathrm{T} = -150°\mathrm{C}$ |
| Boundary Condition | $-k\nabla T = h\,(T - T_{cool})$<br>$h = 100\frac{W}{m^2K}$<br>$T_{cool} = -150°\mathrm{C}$ | $-k\nabla T = h\,(T - T_{warm})$<br>$h = 100\frac{W}{m^2K}$<br>$T_{warm} = 37°\mathrm{C}$ | $q'' = -k\nabla T = 0$<br>Adiabatic |

An IONP concentration ($C_{Fe}$) of 10 mgFe/mL was assumed to be distributed uniformly throughout the modeled biomaterial geometry, based upon organ perfusion work in recent studies [17, 18]. The IONP specific absorption rate ($SAR_{Fe}$) was defined as the volumetric power deposited through hysteresis losses of the IONP within the biomaterial while placed within a radiofrequency coil (i.e., an alternating magnetic field). For the purpose of simplification, we assume $SAR_{Fe}$ is constant at 651 W/gFe (temperature average) for a field of 64 KA/m and 185 KHz, as reported previously [15, 17, 18], since SAR temperature dependence doesn't affect the results across size scale. This value was applied for IONPs in all CPAs modeled, VS55, M22, and DP6. Multiplying by the IONP concentration yields the volumetric heat generation term ($q_V'''$) for nanowarming. Center cooling rates and warming rates were estimated as the temperature averages (ΔT/time) in the range of 0°C to -100°C, as ice growth rates in the studied CPAs are practically negligible outside this range [32–35] [36, 37]. In practical scenarios, the temperature range for the rates should be limited till $T_{melt}$ of a CPA, but for this study 0°C was chosen for convenience since melt temperatures for all three CPAs (DP6, VS55, M22) are quite different. Therefore, our range of estimated cooling and warming rates provides a worst-case analysis. These calculated cooling and warming rates were then compared to the CCRs and CWRs of the CPAs analyzed for evaluating failure due to ice crystallization during cooling and/or recrystallization (and/or devitrification) during rewarming. These critical rates have been listed in Table 3.2 for VS55, DP6, and M22.

For evaluating fracture failure resulting from thermal stresses, temperature difference, $\Delta T$, is used to compute thermal stresses using the simplified form of the thermal shock equation, and these stresses are then compared to the tensile yield strength of the CPA from the literature [38].

Table 3.2. Thermo-physical properties and critical rates of VS55, DP6, and M22

| CPA | Thermal Conductivity: k (W/m.K) | Specific Heat: Cp (kJ/kg.K) | Density: ρ (kg/m3) | Coefficient of linear thermal expansion: β (1/ºC) | CCR (ºC/min) | CWR (ºC/min) |
|---|---|---|---|---|---|---|
| VS55 | 0.3 [29] | 3.011(-1.5ºC) 2.925(-21ºC) 2.819(-44.5ºC) 2.715(-78.8ºC) 2.968(-118ºC) 1.134(-128ºC) 0.985(-150ºC) [47] | 1100 [16] | $1.785*10^{-4}$ [27] | <~1 [33] | ~50 [33] |
| DP6 | 0.3 [29] | 2.984 (0ºC) 2.824(-21ºC) 2.675(-44ºC) 2.460(-88ºC) 2.653(-110ºC) 1.224(-121ºC) 0.888(-149ºC) [47] | 1100 [16] | $1.893*10^{-4}$ [27] | ~40 [46] | ~200 [46] |
| M22 | 0.3 [29] | 3.43 (0ºC) 3.378 (-18ºC) 3.318 (-40ºC) 3.180(-76ºC) 3.324(-119ºC) 1.461(-130ºC) 1.318 (-149ºC) [47] | 1100 [16] | $2.52*10^{-4}$ [30, 31] | 0.1 [13, 28, 49, 50] | 0.4 [13, 28, 49, 50] |

Further, for ease, the calculated ΔT can also be compared to a tolerable value $\Delta T_{max}$ derived for each CPA (VS55, DP6, and M22) from the simplified form of the "thermal shock equation" as shown below:

$$\sigma = g\left(\frac{E\beta\Delta T}{1\text{-}v}\right) \quad (3.2)$$

$$\Delta T_{max} = \sigma_{tensile}\,\frac{(1-v)}{gE\beta} \quad (3.3)$$

where g is the geometric coefficient (0.5 for cylindrical geometry), ν is Poisson's ratio (adapted as 0.2 for typical brittle materials), E is the modulus of elasticity (adapted as 1 GPa for organic materials) and σ is the tensile yield strength of CPA (adapted as 3.2 MPa), based upon prior literature [38].

For simplification and lack of adequate availabile data for all three CPAs, we used the tensile strength (~3.2 MPa) of a closely related CPA (7M DMSO) for all three CPAs analyzed here [38]. Previous studies have measured thermal expansion and strain within CPAs such as DMSO, VS55, DP6, and recently M22 [26, 27, 30]. For our simple analysis, we assumed a constant value of the coefficient of linear thermal expansion, as shown in Table 3.2, which if anything, would reduce at lower temperatures [27, 40] and hence decrease the estimated thermal stresses. Hence, our assumption results in a worst-case scenario analysis.

Further, it is to be noted that in such a high-viscosity regime, linear thermal expansion coefficients (thermal strain cycles) of CPAs (VS55 and DP6) don't differ greatly during cooling vs. rewarming. Now, to consider the fracture failure mode, the largest occurring temperature difference ΔT |Tcenter-Tedge|, is estimated in the region between -115 °C (~set temperature of DP6; Tset is 5 to -10°C higher than Tg, glass transition temperature) down to -150 °C (storage temperature). This is due to the fact that regions well below the set temperature (10–15°C below) are most vulnerable to cracking due to the regime's very high-viscosity, elastic, solid-like behavior, where significant stresses start to arise and are proportional to the temperature difference in geometry [38, 39]. During rewarming, the temperature difference, ΔT, is estimated when the center is still at -150°C whereas the edge is either in the glassy region or above it.

It is to be noted that ΔT in the region when the geometric center is still in the cryogenic temperature range and the edge is heated to around melt temperature is also critical to evaluate if any part of the geometry (more likely near the boundary) experience suprazero temperatures, which could potentially enhance CPA toxicity and hence induce another mode of failure, though this was not

the focus of this study [28, 41–42] [43]. The details about initial and boundary conditions utilized in numerical FEA simulations for convective cooling, convective warming, and nanowarming are laid out in Table 3.1. Convective cooling is modeled as cooling inside a controlled-rate freezer (CRF) (for instance, Planar Kryo 560 II), wherein the flow of liquid nitrogen (LN2) vapors cool samples from their boundaries inward. For a best case of maximum cooling, we assume the chamber temperature is maintained at a temperature similar to the storage temperature, i.e., Tcool (-150°C). Further, for simplicity, we assumed a value for the heat transfer coefficient inside the CRF based on the literature [17] which is in the range of heat transfer coefficients for forced convection in gases. For the convective rewarming case, the sample geometry was assumed to be submerged in a heated water bath maintained at $T_{warm}$ (37°C) to achieve a convective heat flux at the boundary with a free convection heat transfer coefficient, as mentioned in Table 3.2 [44, 48]. The effect of the change in the heat transfer coefficient (h) on cooling and warming rates diminishes as the size of the system increases. Similarly, to analyze the ideal and best case of nanowarming, we assume an adiabatic boundary condition.

# Results

For all the cases, the temperature solution was numerically computed using FEA in COMSOL 5.4, where the model geometry was designed and simulated. During convective cooling, the geometry is subjected to convective heat flux, wherein the temperature starts at 0°C and the whole geometry reaches the ambient cold temperature of -150°C, the storage temperature of a vitrified biomaterial. Figure 3 shows the numerical results for the cooling rates and temperature differences for the convective cooling cases. As expected, the center of the geometry cools more slowly than the edge due to convective heat transfer (loss) occurring from the surroundings, i.e., the boundary of geometry, which can be seen in Figures 3.3A and 3.3C.

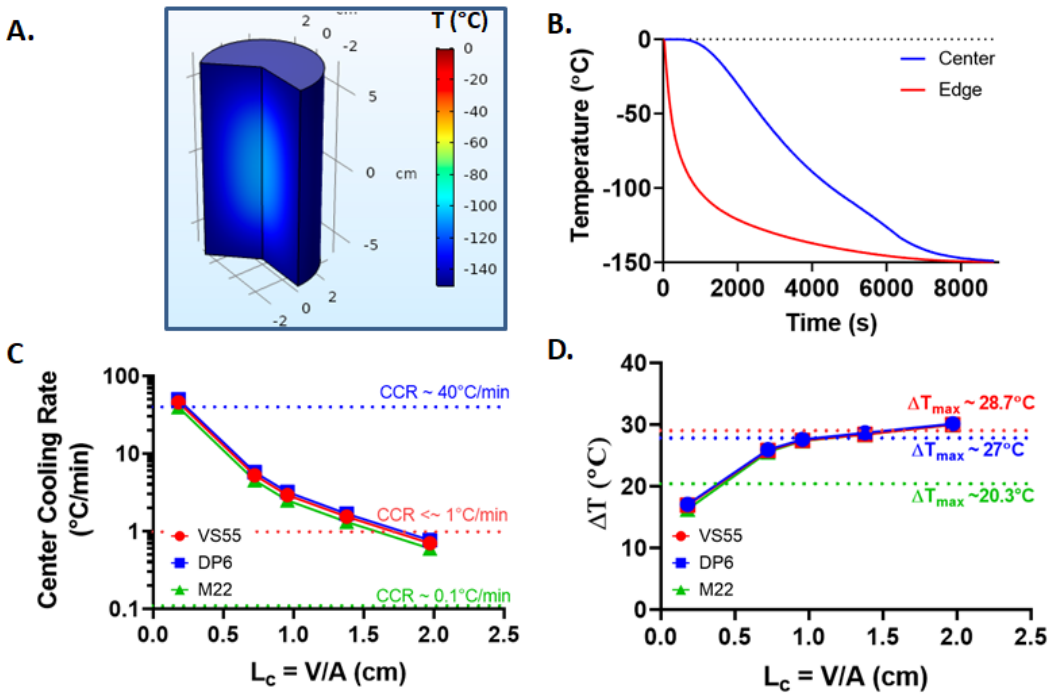


Figure 3.3. Convective cooling: For a representative case of $L_C$ = 1.38 cm (or 500mL) M22 system (A.) Temperature distribution inside the geometry around Tg (~120°C). (B.) Convective cooling temperature curve. (C.) Center cooling rate variation with characteristic length of geometry for all the three CPAs. (D.) Plot of temperature difference (ΔT) with characteristic length ($L_C$) of geometry.

This means that the center of the geometry would be the limiting factor for achieving sufficient cooling rates (i.e., higher than CCR) to avoid any ice formation during the vitrification process. As the center of geometry is at the highest risk of ice crystallization, ensuring success at the center (center cooling rate > CCR) would naturally imply all the other regions of geometry having achieved successful vitrification. It is observed that significantly larger cooling rates (~50°C/min) can be achieved for a smaller characteristic length ($L_C$ < ~0.18cm). As can be seen in Figure 3C, cooling rate decreases rapidly with increasing Lc (or volume) of the cylinder; therefore, for larger $L_C$ (or volumes), a CPA with a significantly low CCR is the ideal candidate for successful vitrification, e.g., M22 in our analysis. The temperature differences are higher for a larger characteristic length, as could be expected due to the convective heat flux boundary. However, the gradients seem to flatten with further increase in $L_C$ (> ~1cm) (or volume). Table 3.3 contains the computed center cooling and warming rates and the maximum temperature differences (ΔT) based on the numerical solution for all characteristic lengths (or volumes) and boundary conditions.

Table 3.3. Numerical simulation results for convective cooling, convective warming and nanowarming for all the cases.

| Convective Cooling | | | VS55 | | | DP6 | | | M22 | | |
|---|---|---|---|---|---|---|---|---|---|---|---|
| | | | $CR_{Center}$ (°C/min) | ΔT (°C) | σ (MPa) | $CR_{Center}$ (°C/min) | ΔT (°C) | σ (MPa) | $CR_{Center}$ (°C/min) | ΔT (°C) | σ (MPa) |
| Volume (mL) | D (cm) | Lc (cm) | CCR<~1 | $\Delta T_{max}$ ~28.7 | $\sigma_{max}$~3.2 | CCR~40 | $\Delta T_{max}$ ~27 | $\sigma_{max}$~3.2 | CCR~0.1 | $\Delta T_{max}$ ~20.3 | $\sigma_{max}$~3.2 |
| 1 | 1 | 0.18 | 45.95 | 17.08 | 1.91 | 50.06 | 16.95 | 2.0 | 39.76 | 16.28 | 2.56 |
| 80 | 3.5 | 0.72 | 5.27 | 25.96 | 2.89 | 5.76 | 25.83 | 3.05 | 4.54 | 25.58 | 4.03 |
| 160 | 5 | 0.96 | 2.92 | 27.60 | 3.08 | 3.2 | 27.45 | 3.25 | 2.5 | 27.38 | 4.31 |
| 500 | 7 | 1.38 | 1.54 | 28.67 | 3.19 | 1.68 | 28.42 | 3.36 | 1.32 | 28.41 | 4.47 |
| 1300 | 12 | 1.97 | 0.70 | 30.15 | 3.36 | 0.77 | 30.0 | 3.54 | 0.60 | 30.0 | 4.72 |
| Convective Warming | | | VS55 | | | DP6 | | | M22 | | |
| | | | $CR_{Center}$ (°C/min) | ΔT (°C) | σ (MPa) | $CR_{Center}$ (°C/min) | ΔT (°C) | σ (MPa) | $CR_{Center}$ (°C/min) | ΔT (°C) | σ (MPa) |
| Volume (mL) | D (cm) | Lc (cm) | CWR~50 | $\Delta T_{max}$ ~28.7 | $\sigma_{max}$~3.2 | CWR~200 | $\Delta T_{max}$ ~27 | $\sigma_{max}$~3.2 | CWR~0.4 | $\Delta T_{max}$ ~20.3 | $\sigma_{max}$~3.2 |
| 1 | 1 | 0.18 | 50.12 | 18.06 | 2.01 | 50.76 | 17.91 | 2.12 | 43.6 | 18.33 | 2.89 |
| 80 | 3.5 | 0.72 | 5.7 | 31.54 | 3.52 | 5.8 | 30.81 | 3.64 | 5.05 | 31.8 | 5.00 |
| 160 | 5 | 0.96 | 3.36 | 35.97 | 4.01 | 3.4 | 35.19 | 4.16 | 2.91 | 37.79 | 5.95 |
| 500 | 7 | 1.38 | 1.75 | 43.61 | 4.86 | 1.78 | 42.97 | 5.08 | 1.52 | 47.26 | 7.44 |
| 1300 | 12 | 1.97 | 0.85 | 56.34 | 6.28 | 0.86 | 55.68 | 6.59 | 0.74 | 59.02 | 9.29 |
| Nanowarming | | | VS55 | | | DP6 | | | M22 | | |
| | | | $CR_{Center}$ (°C/min) | ΔT (°C) | σ (MPa) | $CR_{Center}$ (°C/min) | ΔT (°C) | σ (MPa) | $CR_{Center}$ (°C/min) | ΔT (°C) | σ (MPa) |
| Volume (mL) | D (cm) | Lc (cm) | CWR~50 | $\Delta T_{max}$ ~28.7 | $\sigma_{max}$~3.2 | CWR~200 | $\Delta T_{max}$ ~27 | $\sigma_{max}$~3.2 | CWR~0.4 | $\Delta T_{max}$ ~20.3 | $\sigma_{max}$~3.2 |
| 1 | 1 | 0.18 | 126 | NA | | 133 | NA | | 108 | NA | |
| 80 | 3.5 | 0.72 | 126 | | | 133 | | | 108 | | |
| 160 | 5 | 0.96 | 126 | | | 133 | | | 108 | | |
| 500 | 7 | 1.38 | 126 | | | 133 | | | 108 | | |
| 1300 | 12 | 1.97 | 126 | | | 133 | | | 108 | | |

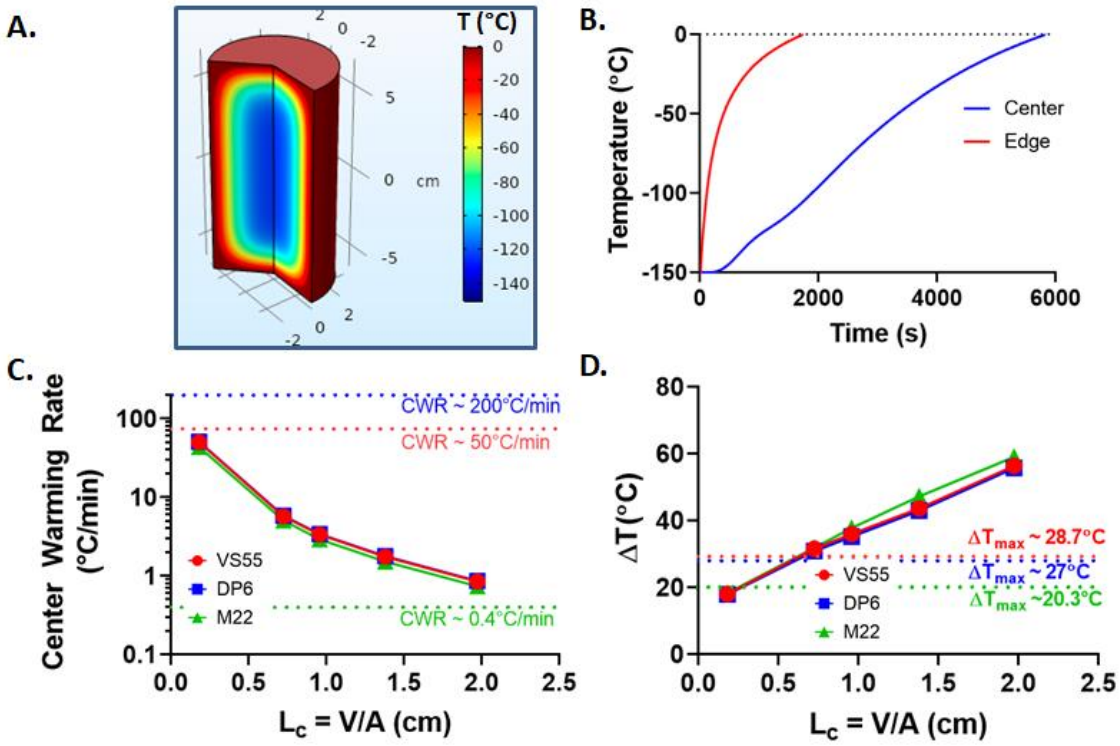


Figure 3.4. Convective warming: For a representative case of $L_C$ = 1.38 cm (or 500mL) M22 system (A.) Temperature distribution inside the geometry around Tg (~120°C). (B.) Convective warming temperature curve. (C.) Center warming rate variation with characteristic length of geometry for all the three CPAs. (D.) Plot of temperature difference (ΔT) with characteristic length ($L_C$) of geometry.

For the case of convective warming, faster warming occurs on the edges compared to the center of geometry. Thus, the center is the limiting region for achieving sufficient warming rates to avoid devitrification (and/or ice recrystallization). We have plotted these rates in Figure 3.4C. Indeed, rates actually fall below 1 °C/min for volumes greater than 1L ($L_C$ > 1.9cm) for all three CPAs. For all five volumes, the center warming rates and maximum temperature differences along with thermal stresses are tabulated in Table 3.3. As can be seen, successful rewarming for DP6 and VS55 becomes more challenging even for smaller $L_C$ (or volumes) due to the high CWR required (since CWRs are order of magnitude or more larger than CCRs) [46, 51, 54]. Further, in Figure 3.4B, the edge of the geometry heats up quickly, reaching a suprazero temperature while the rest of the geometry is still at cryogenic temperatures, leading to large temperature gradients, which could be detrimental due to excessive thermal stresses and other factors. While this study focuses on ice

formation and fractures as the only modes of failure, other modes such as CPA toxicity could become important at high suprazero temperatures especially if held for longer time [41, 54].

Nanowarming is performed from the storage temperature of -150°C and terminated when the geometry reaches 0°C. Due to the internal heat generation and an ideal, i.e., adiabatic, boundary condition, the whole geometry heats up at the same rate, with DP6 at around 133 °C/min, VS55 at 126 °C/min, and M22 at 108 °C/min. Further, the heat generation during nanowarming relies only on the IONPs and an external alternating magnetic field. Thus, heating can be both rapid and independent of sample size (volume), unlike convective or other boundary rewarming methods. The warming rates of the center during nanowarming can be seen in Figure 3.5C and are notably higher than those for convective warming for all the CPAs. Since the IONPs are assumed to be uniformly distributed, the heat generation during nanowarming is quite uniform and does not lead to temperature gradients, as shown in Figure 3.5D.

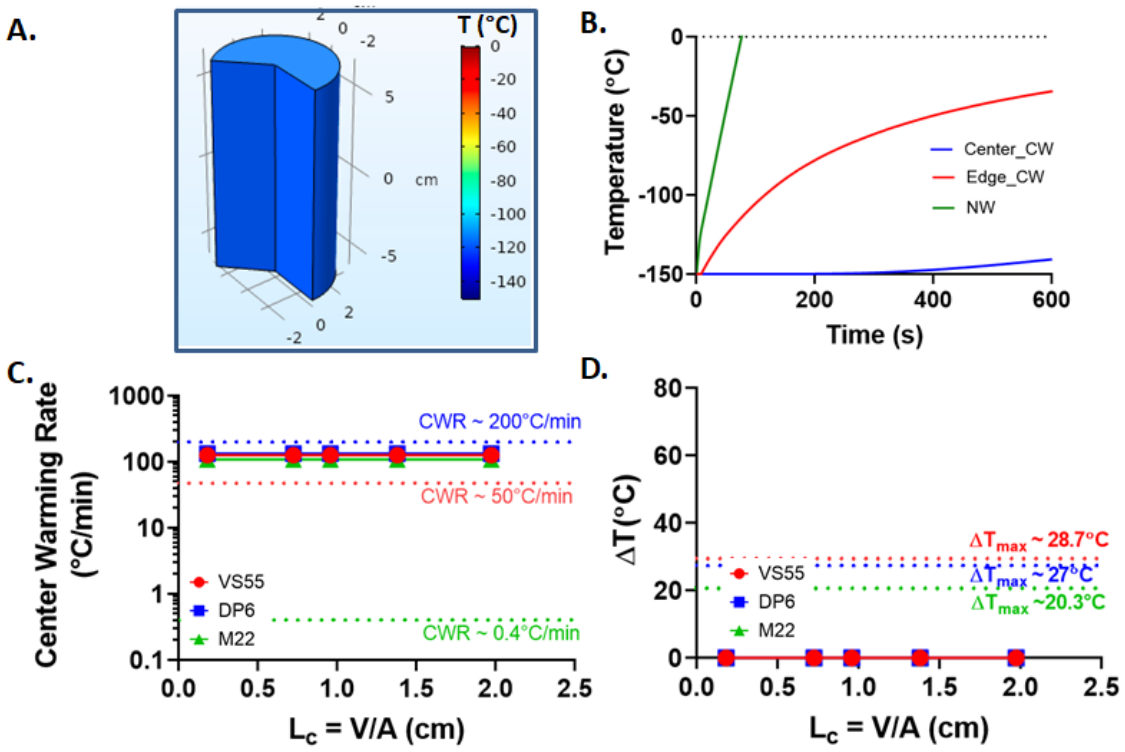


Figure 3.5. Nanowarming: For a representative case of $L_C$ = 1.38 cm (or 500mL) M22 system (A.) Temperature distribution inside the geometry around Tg (~120°C). (B.) Nanowarming temperature curve compared to convective warming. (C.) Center warming rate variation with characteristic length of geometry for all the three CPAs. (D.) Plot of temperature difference (ΔT) with characteristic length ($L_C$) of geometry.

Among the three CPAs studied, DP6 achieved the highest cooling and warming rates. VS55 demonstrated slightly lower rates than DP6, and M22 had the lowest rates among all three CPAs. This is likely due to M22 having the highest specific heat, followed by VS55, and then DP6 (Table 3.2). It should be noted that in practice nanowarming might be performed in the absence of perfect insulation at the boundary. Under these conditions, some natural convective heat flux from the surroundings would be expected to increase the warming rates and might introduce non-uniformity (i.e., temperature gradients).

To further generalize the findings, we normalized the computed cooling and warming rates to the CCR and CWR of each CPA, which are plotted in Figure 3.6. These normalized figures help to clearly map success and failure during vitrification and rewarming (e.g., normalized values at >1 imply success and <1 failure). A parametric non-linear fit has been performed on these normalized values and given below in equations 3.4 and 3.5.

$$log(\frac{CR}{CCR} or \frac{WR}{CWR}) = a1 \ log\, Lc[cm] + a2 \qquad (3.4)$$

$$log(\frac{\Delta T_{max}}{\Delta T}) = b1 \ log\, Lc[cm] + b2 \qquad (3.5)$$

Table 3.4. Coefficient of Fits for the normalized CR, WR & ΔT Equations (3.4) & (3.5)

| CPA | Fit Coefficient | | | |
|---|---|---|---|---|
| | a1 | a2 | b1 | b2 |
| Convective Cooling | | | | |
| VS55 | -1.605 | 0.465 | -0.257 | 0.028 |
| DP6 | -1.603 | -1.098 | -0.258 | 0.005 |
| M22 | -1.609 | 1.399 | -0.278 | -0.117 |
| Convective Warming | | | | |
| VS55 | -1.595 | -1.189 | -0.426 | -0.114 |
| DP6 | -1.589 | -1.847 | -0.449 | -0.153 |
| M22 | -1.589 | 0.852 | -0.474 | -0.291 |

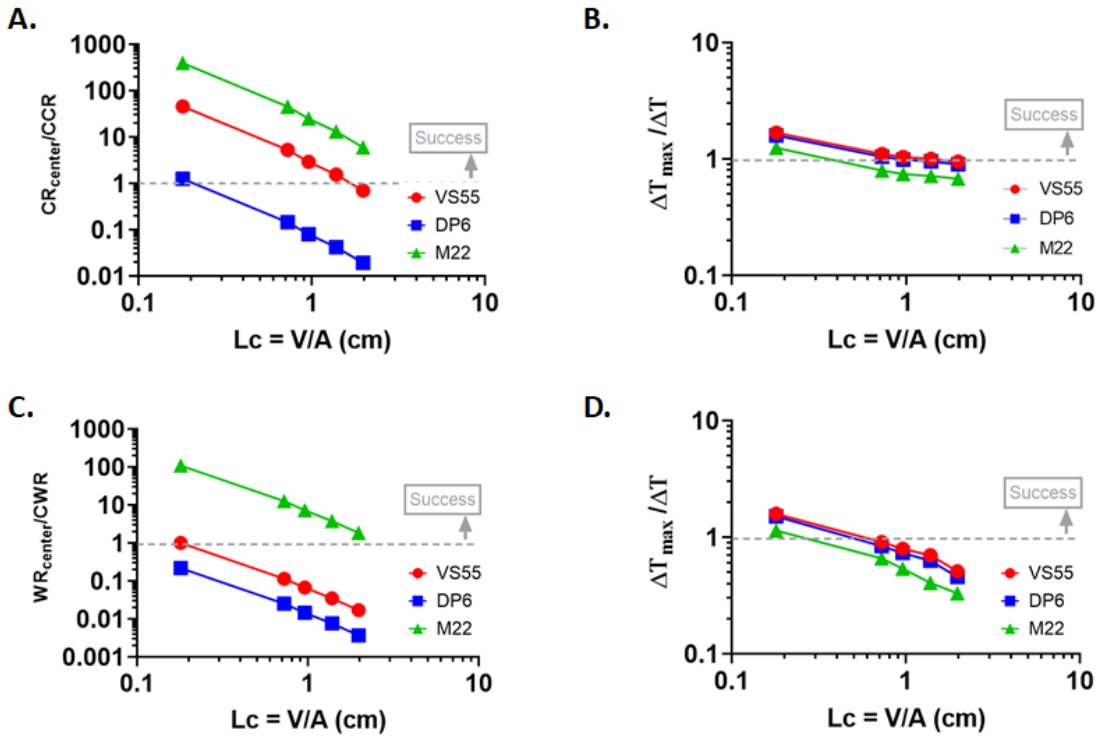


Figure 3.6 (A. & C.) Plots of non-linear fits for the normalized center cooling and warming rates to critical cooling (CCR) and critical warming rate (CWR) of the chosen CPAs during convective cooling and convective warming respectively. (B. & D.) Plots of non-linear fits for the normalized temperature difference (ΔT) to the maximum temperature difference (ΔTmax) calculated from "simplified thermal shock equation" of the chosen CPAs during convective cooling and convective warming respectively.

As seen in Figure 3.6A and 3.6C these normalized values clearly separate out for the three CPAs analyzed, thereby highlighting the importance of failure thresholds (i.e. CCR, CWR, and ΔTmax) and better fit of a CPA in potential success during vitrification and rewarming. For convective cooling, normalized CR of M22 seems to be above 1 (success) irrespective of $L_C$ (or volume) of geometry as opposed to VS55 where normalized CR falls below 1 (failure) for Lc approximately >1.8 cm, evident in Figure 3.6A. Similarly, for convective warming, M22 seems to be the only CPA that displays normalized WR >1 (success) for all the characteristic lengths of the geometry analyzed ($L_c$ < 3.2 cm), as in Figure 3.6C. DP6 seems to be the most unlikely candidate to achieve success during convective cooling or rewarming, as seen in Figures 6A and 6C. Table 3.5 provides a summary of the critical $L_c$ beyond which failure is likely to occur for any of the CPAs studied, i.e., $L_c$ for normalized value (CR/CCR, WR/CWR or $\Delta T_{max}/\Delta T$) = 1.

Table 3.5. Characteristic length ($L_C$) corresponding to potential failure either due to ice formation or thermal cracking for VS55, DP6 and M22

| CPA | | $L_C$ (cm) | |
|---|---|---|---|
| | | Ice Formation | Cracking/ Fracture |
| VS55 | Convective Cooling | 1.95 | 1.28 |
| DP6 | | 0.21 | 1.04 |
| M22 | | 7.4 | 0.38 |
| VS55 | Convective Warming | 0.18 | 0.54 |
| DP6 | | 0.07 | 0.46 |
| M22 | | 3.43 | 0.24 |

M22 seems to be the most ideal candidate for convective cooling and rewarming as its normalized CR and WR are greater than 1 for all characteristic lengths analyzed, which can be attributed to the fact it has an incredibly low CCR (0.1 °C/min) and CWR (0.4 °C/min) [49–50]. For fracture, VS55 and DP6 seem to be better as their critical $L_C$ seems to be >1 for convective cooling and ~0.5 during convective rewarming, as opposed to M22 being 0.38 and 0.28 respectively, which can be explained by the higher value of the linear thermal expansion coefficient of M22 assumed in this study. VS55 seems to work well during convective cooling for Lc up to 1.28 cm, where both the normalized CR and $\Delta T$ are > 1, but is not as viable an option during convective rewarming for $L_C$ < 0.18cm. For DP6, success during convective cooling is more difficult to achieve (critical $L_C$ ~ 0.21 cm) and almost impossible for convective rewarming (critical $L_C$ ~ 0.07 cm), as evident in Figure 3.6B and Table 3.5. Therefore, the best performing CPA is M22 even though it has the potential of higher thermal stress, which needs to be evaluated further. Additionally, steps such as annealing and slow cooling below glass transition temperature are known to be helpful in mitigating large temperature differences or thermal stresses (and hence fractures) when transitioning into the glassy phase, but they were not considered in this study. It is to be noted that $\Delta T_{max}$ would be higher, therefore, in a case of a cryobag (more similar to an ideal plate shape) as the geometric coefficient (g) in the thermal shock equation is smaller, i.e., g = 1/3 for a plate shape as opposed to g = 1/2 for a cylindrical shape [39]. Further, the threshold $\Delta T_{max}$ here is quite conservative and will vary depending upon the above assumed parameters. For instance, the coefficient of linear thermal expansion (ß) depends on temperature range as opposed to constant assumption here. For the cryogenic range, it decreases, thereby increasing this threshold

value and decreasing the estimated thermal stresses. Hence, the estimate here would be the worst-case scenario for evaluating fracture failure. Finally, it should be noted that the applicability of simplified thermal shock equation for thermal stresses predictions at larger scale volumes (or $L_C$) would need to be further evaluated experimentally for understanding role of thermal gradients in fracture failure.

To apply the results of this study in practical lab scenarios, it is important to understand and calculate the characteristic length (Lc) of the sample for any desired cooling or rewarming conditions. To correlate a lab experiment scenario prediction based upon these numerical model results, here we compare the literature data for a rat kidney [17] consisting total cryopreserved volume of 30mL (kidney + surrounding CPA solution) in a 5.5×4.4×1.5cm cryobag, with our modeling predictions. Characteristic length (Lc) for the above cryobag scenario can be calculated as ~0.75cm, using which we can then estimate a cooling rate of 7 °C/min from Figure 3.3, which is close to the experimentally calculated value of 6.5 °C/min. Similarly, during nanowarming, the predicted warming rate is around 51 °C/min, which broadly agrees with the reported value of 55 °C/min measured during experiments. It is to be noted that for the nanowarming case, the warming rates are independent of the size of the system (or Lc). Therefore, the same heating rate should exist for different geometries for a fixed IONP concentration and other assumptions such as the adiabatic ambient medium. In this study, the IONP concentration of 10 mgFe/mL is assumed to be uniformly distributed throughout the geometry; for other scenarios, one can still roughly estimate the nanowarming rates based upon linear normalization with the chosen IONP concentration in their experiments. Therefore, for the scenario of the rat kidney, discussed above, WR was predicted using this model as 126×(4 mgFe/mL/10 mgFe/mL), which comes out to be 50.6 °C/min.

Lastly, it should be noted that these results are applicable for a convective heat transfer coefficient of ~100 W/m$^2$K during convective cooling and convective rewarming. Therefore, for conditions with a significantly different h, the results would be expected to vary. For instance, for straws with microliter volumes, where h ~10,000 W/m2K as the boiling convection coefficient in LN2, the predicted CR using this model would be smaller than that expected based solely on experiments (underprediction) [52, 53].

# Discussion

This study demonstrates the conditions for the success and failure of vitrification and rewarming for various characteristic length systems and cooling or rewarming scenarios. Empirical fit equations (4–6) have been derived for the variation of cooling rates, warming rates, and maximum temperature gradients, with the characteristic length of geometry applicable to the corresponding volume of biomaterial (i.e., VS55, DP6, or M22). These equations (3.4–3.5) can be utilized for estimating cooling or warming rates along with temperature gradients for a given volume (or characteristic length) system, which can help predict success or failure during vitrification and/or rewarming. More specifically, we show that CPAs with low critical cooling and warming rates along with smaller linear thermal expansion coefficients have higher probabilities of success at larger volumes (~1L) or larger characteristic lengths. Convective rewarming can be used for volumes with smaller characteristic lengths (Lc < ~0.2cm) for most CPAs tested. However, it becomes inadequate to accomplish sufficient warming rates and uniformity to avoid any ice formation or cracking for larger volumes [44, 55–57]. Volumetric rewarming through nanowarming is one alternative to extend the range of successful rewarming for some CPAs. Studies in the past have shown that modification of common CPAs such as DP6 by the addition of sugars (e.g., sucrose) or polymers (e.g., PEG400) can enhance the vitrification tendency leading to superior glass formation [57–59]. Hence, further investigation of other CPAs, or modified CPAs, will continue to be an important area of research for cryopreserving larger volumes and characteristic length systems. Future studies should continue to experimentally examine the rates and gradients for validation of success of larger volumes (Liter systems with >1.5cm characteristic lengths). Unfortunately, a reduction in cooling rates during convection will always result with an increase in characteristic length unless a volumetric cooling technique can be discovered or invented. In summary, this work expands upon existing techniques to provide practical guidelines to avoid ice crystallization and cracking during cooling and warming from a vitrified state across mL to L size scales several well-known CPAs.

# References for Chapter 3


1. Pegg DE (2007) Cryopreservation and freeze-drying protocols, 39-57. doi: 10.1007/978-1-59745-362-2_3
2. Finger EB, Bischof JC (2018) Current opinion in organ transplantation 23(3), 353-360. doi: 10.1097/mot.0000000000000534.
3. Giwa S, Lewis JK, Alvarez L, Langer R, Roth AE, Church GM, Markmann JF, Sachs DH, Chandraker A, Wertheim JA, Rothblatt M, Boyden ES, Eidbo E, Lee WPA, Pomahac B, Brandacher G, Weinstock DM, Elliott G, Nelson D, Acker JP, Uygun K, Schmalz B, Weegman BP, Tocchio A, Fahy GM, Storey KB, Rubinsky B, Bischof J, Elliott JAW, Woodruff TK, Morris GJ, Demirci U, Brockbank KGM, Woods EJ, Ben RN, Baust JG, Gao D, Fuller B, Rabin Y, Kravitz DC, Taylor MJ, Toner M (2017) Nature biotechnology 35(6), 530-542. doi: 10.1038/nbt.3889.
4. Fahy GM, MacFarlane DR, Angell CA, Meryman HT (1984) Cryobiology 21(4), 407-426. doi: 10.1016/0011-2240(84)90079-8.
5. Arav A, Patrizio P (2019) Clinical Medicine Insights: Reproductive Health, 13, 1179558119884945. doi: 10.1177/1179558119884945.
6. Lujić J, Marinović Z, Sušnik Bajec S, Djurdjevič I, Kása E, Urbányi B, Horváth Á (2017) Cryobiology 76, 154-157. doi: 10.1016/j.cryobiol.2017.04.005.
7. Fahy GM, Wowk B, Wu J, Phan J, Rasch C, Chang A, Zendejas E (2004) Cryobiology 48(2), 157-178. doi: 10.1016/j.cryobiol.2004.02.002.
8. Daly J, Zuchowicz N, Nuñez Lendo CI, Khosla K, Lager C, Henley EM, Bischof J, Kleinhans FW, Lin C, Peters EC, Hagedorn M (2018) Scientific Reports 8(1), 1-10. doi: 10.1038/s41598-018-34035-0.
9. Khosla K, Kangas J, Liu Y, Zhan L, Daly J, Hagedorn M, Bischof J (2020) Advanced biosystems 4(11), 2000138.
10. Mullen SF, Fahy GM (2011) In: Donnez J, Kim SS (eds) Principles and Practice of Fertility Preservation Cambridge University Press, Cambridge, 145-163.
11. Boutron P (1993) Cryobiology 30(1), 86-97
12. Boutron P, & Mehl P, (1990) Theoretical prediction of devitrification tendency: determination of critical warming rates without using finite expansions. Cryobiology 27(4), 359-377. doi: 10.1016/0011-2240(90)90015-v.
13. Rall WF, Fahy GM (1985) Nature 313(6003), 573-575.
14. Fahy GM, Wowk B, Pagotan R, Chang A, Phan J, Thomson B, Phan L (2009) Organogenesis 5(3), 167-175. doi: 10.4161/org.5.3.9974.
15. Manuchehrabadi N, Gao Z, Zhang J, Ring HL, Shao Q, Liu F, McDermott M, Fok A, Rabin Y, Brockbank KG, Garwood M, Haynes CL, Bischof JC (2017) Science translational medicine, 9(379), eaah4586. doi: 10.1126/scitranslmed.aah4586
16. Etheridge ML, Xu Y, Rott L, Choi J, Glasmacher B, Bischof JC (2014) Technology, 2(03), 229-242.
17. Sharma A, Rao JS, Han Z, Gangwar L, Namsrai B, Gao Z, Ring HL, Magnuson E, Etheridge M, Wowk B (2021) Vitrification and Nanowarming of Kidneys. Advanced Science 8(19), 2101691. doi: 10.1002/advs.202101691.
18. Gao Z, Namsrai B, Han Z, Joshi P, Rao JS, Ravikumar V, Sharma A, Ring HL, Idiyatullin D, Magnuson EC (2022) Advanced Materials Technologies 7(3), 2100873. doi: 10.1002/admt.202100873.
19. Chiu-Lam A, Staples E, Pepine CJ, Rinaldi C (2021) Science advances 7(2), eabe3005. doi: 10.1126/sciadv.abe3005.
20. Fahy GM, Saur J, Williams RJ (1990) Cryobiology 27(5), 492-510.

21. Solanki PK, Bischof JC, Rabin Y (2017) Cryobiology 76, 129-139.
22. Solanki PK, Rabin Y (2021) Cryobiology 100, 180-192. doi: 10.1016/j.cryobiol.2021.01.002.
23. Ehrlich LE, Fahy GM, Wowk BG, Malen JA, Rabin Y (2018) Journal of biomechanical engineering 140(1). doi: 10.1115/1.4037406.
24. Gao Z, Ring HL, Sharma A, Namsrai B, Tran N, Finger EB, Garwood M, Haynes CL, Bischof JC (2020) Advanced Science 7(4), 1901624. doi: 10.1002/advs.201901624.
25. Eisenberg DP, Steif PS, Rabin Y (2014). Cryogenics 64, 86-94. doi: 10.1016/j.cryogenics.2014.09.005.
26. Plitz J, Rabin Y, and Walsh JR (2004) Cell Preservation Technol. 2, 215-226.
27. Rios JLJ & Rabin Y (2006) Cryobiology 52(2), 284-294.
28. Fahy GM, Wowk B, Wu J, Paynter S (2004) Cryobiology 48(1), 22-35.
29. Ehrlich LE, Gao Z, Bischof JC, & Rabin Y (2020) Plos one 15(9), e0238941. doi: 10.1371/journal.pone.0238941.
30. Solanki P & Rabin Y (2022) CryoLetters 43(1), 1 – 9 (2022).
31. Solanki PK (2020) Doctoral dissertation, Carnegie Mellon University. doi: 10.1184/R1/19148930.v1.
32. Wowk B (2010) Cryobiology 60(1), 11-22. doi: 10.1016/j.cryobiol.2009.05.007
33. Mehl PM (1993) Cryobiology 30(5), 509--518. doi: 10.1006/cryo.1993.1051.
34. Baicu S, Taylor MJ, Chen Z, Rabin Y (2007) Cell preservation technology 4(4), 236-244. doi: 10.1089/cpt.2006.9994.
35. Taylor M, Song Y, Brockbank K (2004) CRC Press, Boca Raton, 603-641.
36. Hey JM, & Macfarlane DR (1998) Cryobiology 37(2), 119-130. doi: 10.1006/cryo.1998.2108
37. Hey JM, & Macfarlane DR (1996) Cryobiology 33(2), 205-216. doi: 10.1006/cryo.1996.0021
38. Rabin Y, Steif PS, Hess KC, Jimenez-Rios JL & Palastro MC (2006) Cryobiology 53(1), 75-95. doi: 10.1016/j.cryobiol.2006.03.013.
39. Steif PS, Palastro MC & Rabin Y (2007) Cell preservation technology 5(2), 104-115. doi: 10.1089/cpt.2007.9994.
40. Rabin Y & Plitz J (2005) Annals of Biomedical Engineering, 33(9), 1213-1228. doi: 10.1007/s10439-005-5364-0.
41. Clark P, Fahy GM, & Karow Jr AM (1984) Cryobiology 21(3), 274-284. doi: 10.1016/0011-2240(84)90323-7.
42. Best BP (2015) Cryoprotectant Toxicity: Facts, Issues, and Questions. Rejuvenation research 18: 422-436 DOI 10.1089/rej.2014.1656
43. Joshi P, Ehrlich LE, Gao Z, Bischof JC, Rabin Y (2022) Thermal Analyses of Nanowarming-Assisted Recovery of the Heart From Cryopreservation by Vitrification. Journal of Heat Transfer 144: 031202
44. Manuchehrabadi N, Shi M, Roy P, Han Z, Qiu J, Xu F, Lu TJ, Bischof J (2018) Annals of Biomedical Engineering 46(11) 1857-1869. doi:10.1007/s10439-018-2063-1
46. Rabin Y, Taylor MJ, Walsh JR, Baicu S, & Steif PS (2005) Cell preservation technology 3(3), 169–183. doi: 10.1089/cpt.2005.3.169.
47. Phatak S, Natesan H, Choi J, Brockbank KG & Bischof JC (2018) Biopreservation and Biobanking 16(4), 270-277. doi: 10.1089/bio.2018.0006.
48. Incropera FP, DeWitt DP, Bergman TL, Lavine AS (1996) Vol. 6, p. 116 New York: Wiley.
49. Fahy GM, Wowk B & Wu J (2006) Rejuvenation research, 9(2), 279-291. doi: 10.1089/rej.2006.9.279
50. Wowk B, Fahy GM (2005) Cryobiology 51, 362.
51. Han Z, Bischof JC (2020) CryoLetters, 41(4), 185-193.

52. Kuleshova LL, Lopata A (2002) Fertility and sterility 78(3), 449-454. doi: 10.1016/s0015-0282(02)03305-8.
53. Vutyavanich T, Sreshthaputra O, Piromlertamorn W & Nunta S (2009) Journal of assisted reproduction and genetics 26(5), 285-290. doi: 10.1007/s10815-009-9324-8.
54. Brockbank KG, Wright GJ, Yao H, Greene ED, Chen ZZ & Schenke-Layland K (2011) The Annals of thoracic surgery 91(6), 1829-1835.
55. Brockbank KG, Chen ZZ, & Song YC (2010) Cryobiology 60(2), 217-221.
56. Brockbank KG, Chen ZZ, Greene ED & Campbell LH (2015) In Cryopreservation and freeze-drying protocols pp. 399-421. Springer, New York, NY.
57. Wowk B, Fahy GM, Ahmedyar S, Taylor MJ & Rabin Y (2018) Cryobiology, 82, 70-77. doi: 10.1016/j.cryobiol.2018.04.006.
58. Sutton RL (1992) Cryobiology 29(5), 585-598. doi: 10.1016/0011-2240(92)90063-8.
59. Kuleshova LL, Macfarlane DR, Trounson AO & Shaw JM (1999) Cryobiology 38(2), 119-130. doi: 10.1006/cryo.1999.2153.

# Chapter 4. Dielectric properties of CPA mixtures in suprazero to subzero temperature range

This chapter presents the dielectric properties (constant and loss) for common organ vitrification CPAs (M22, VS55, DP6) and their components. It provides the basic understanding of dielectric property of a mixture of CPA components with application in dielectric rewarming and eddy heating estimation during RF rewarming. The paper manuscript for this chapter is in preparation. The manuscript is reproduced here:

**Gangwar, Lakshya**, et. al. "  Dielectric properties of cryoprotective cocktails (VS55, M22, DP6) and their constituents in suprazero to subzero temperature range relevant for electromagnetic rewarming technologies in cryopreservation." (2024) In preparation

# Overview

Electromagnetic (EM) rewarming approaches such as nanowarming have drastically improved the possibility of organ banking by allowing successful organ cryopreservation and transplant. EM heating of cryopreserved biomaterials consisting of cryoprotective agents (CPAs) is mainly governed by its dielectric properties (dielectric constant-polarization and dielectric loss- energy dissipation). Hence, understanding how the individual CPA components produce dielectric behavior in CPA mixtures relevant for organ cryopreservation is required for effectively rewarming a vitrified biomaterial system composed primarily of cryoprotectant mixtures and water. In this study we measured dielectric properties as function of composition (mole fraction of components) of CPA mixtures, frequency (1 to 3 GHz range) and temperature (20° to -30°C range). An open-ended coaxial probe is used to measure CPA dielectric properties (loss ε'' and constant ε') experimentally inside a control rate freezer (CRF) producing low subzero temperatures. Computational FEM is also performed in COMSOL 5.4 to evaluate and confirm penetration depth of RF fields from probe into the CPA samples being measured experimentally. Dielectric loss and constant are reported for CPAs (M22, DP6, VS55) in 20 to -40°C and their individual components (DMSO, Formamide, EG, PG) and binary mixtures at room temperature. The present work demonstrates the dielectric loss of CPA cocktail mixtures varies with temperature and frequency and in general decreases at subzero temperatures at higher frequencies (~3GHz) and increases at smaller end of frequencies analyzed (~200MHz). We also found that dielectric loss of CPA mixtures can be higher than its individual two CPA components. This is related to the relaxation time and bonding at molecular level. On a high level, this study contributes towards organ cryopreservation as it allows a. the estimation of the amount of eddy heating relevant for uniform nanowarming in a RF coil, b. understanding the feasibility of direct coupling electromagnetic rewarming approaches such as microwave or dielectric heating.

# Introduction

Cryopreservation has become a forefront technology in extending shelf life of biomaterials such as cells, tissues, and organs for biomedical applications such as cell therapy, regenerative medicine, and fertility preservation. Various ways to cryopreserve a biomaterial exists from storage at subzero temperatures via supercooling and partial freezing, and in lower cryogenic temperatures via freezing and vitrification. After a biomaterial is cooled to these storage temperatures, it requires "optimum" thawing before its end use (example, cells for therapies, tissues for drug testing, organs

for transplant). For organ cryopreservation, where vitrification is the most promising technique for indefinite shelf life, this thawing/heating demands a rapid and uniform rewarming in order to achieve successful cryopreservation outcome. One approach is using electromagnetic (EM) fields for rewarming a cryopreserved biomaterial which has been applied in different forms (dielectric [1, 2], microwave [3, 4], radio-frequency-RF [5, 6]) to date since the first attempts of thawing an organ using electromagnetic (EM) wave in mid-1970s [3, 7]. So far RF rewarming also called as nanowarming has been most promising in scalability to larger volumes (size of human organs) in terms of achieving uniformity and rapid warming rates. Dielectric properties govern the heat dissipation (dielectric loss) and electric polarization (dielectric constant) of a material in the presence of an alternating electromagnetic field. Knowledge of dielectric properties as function of temperature is crucial in characterizing and dictating heating of a cryopreserved sample from subzero or cryogenic temperatures.

Eddy current heating, which is direct mode of coupling of EM waves with cryoprotective agent (CPA) and organs is one challenge which needs to be evaluated when scaling up RF rewarming. To rewarm a cryopreserved organ, indirect approaches such as nanowarming, metal form heating relies upon on the heat generation by external heaters in form of magnetic nanoparticles, metallic foils, etc. whereas direct coupling approaches such as microwave/dielectric rewarming utilizes heat generation directly from cryoprotectants via relaxation of constituent polar molecules in water and CPAs. Dielectric loss depends upon frequency and temperature and exhibits a distinct peak with frequency and temperature as shown in Figure 4.1. In the presence of applied alternating electric field, the polar molecules rotation is resisted by intermolecular forces and hence the dielectric relaxation time depends upon the physical state and viscosity. At higher temperatures (very low viscosity), relaxation time of CPAs are much shorter than time period of applied alternating E field therefore the dipoles can catch up to the changing field and loss values are small. As we go lower in temperature, relaxation time increases due to higher viscosity and when the relaxation time matches the time period of alternating field ($\tau = 1/f$), the distinct peak of dielectric loss is observed. At further lower temperatures, mobility of molecules reduces drastically as viscosity of CPAs increases exponentially therefore the relaxation times are extremely longer than time periods of alternating field and no perturbation/energy loss occurs i.e. dielectric loss decreases to diminishing values. At higher frequencies, implies shorter time period of alternating EM field, the peak of dielectric loss with temperature would move to higher temperatures (right in Figure 4.1) since the relaxation times of dipolar molecules in CPAs is shorter at higher temperatures because of lower viscosity and hence would match the time period of applied alternating field for producing the

highest loss peak. Dielectric properties of CPAs and tissues permeated with CPAs have been measured in past though most of them are either limited to single component CPAs at higher frequencies (not relevant for RF rewarming-nanowarming) as listed in Table 4.1. Therefore, to our knowledge dielectric properties for contemporary more promising organ vitrification CPA mixtures such as VS55, M22, and DP6 are unavailable in literature for any temperature range (near room temperature-suprazero >0°C to subzero <0°C and cryogenic temperature <-100°C).

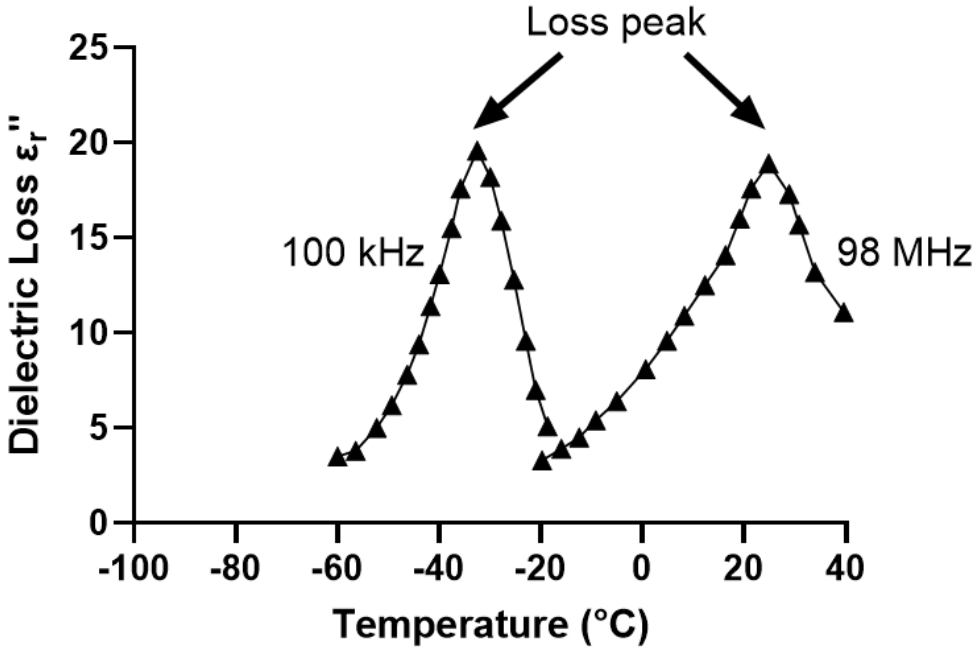


Figure 4.1. Dielectric loss as function of temperature plotted at two different frequencies (100MHz and 98MHz) for a representative CPA-glycerol using data values from literature [8, 9, 11]. Loss peak is shown with black arrows.

Here we measure dielectric constant and loss for a range of frequency (100MHz-3 GHz) and temperature (-30 to 20°C). We further investigate the effect of a single component CPA in a binary mixture of CPA+CPA and CPA+water. This would allow in design and assessment of CPAs for safe rapid and uniform EM rewarming of vitrified large-scale biomaterials such as organs.

Table 4.1: Literature summary of dielectric property measurement of CPAs in a wide frequency and temperature range relevant for cryopreservation applications (arranged by year).

| Sample CPA | Frequency Range | Temperature Range | Measurement Technique | Year and Reference |
|---|---|---|---|---|
| 100w/w% Glycerol | 6 MHz to 98 MHz | -20° to 50°C | - | 1926 [8] |

| | | | | |
|---|---|---|---|---|
| 100w/w% Glycerol | 30 Hz to 100 kHz | -80° to -20°C | - | 1934 [9] |
| 1.4M DMSO+ MS perfusate<br>3M Glycerol+EC1 perfusate<br>3M Glycerol+HP6 perfusate<br>Rabbit kidney+ Glycerol+HP6/EC1 | 84 MHz to 2.45 GHz | -30° to 20°C | OECP | 1987 [10] |
| 50, 60w/w% DMSO<br>50, 60, 85w/w% Glycerol<br>55, 60w/w% EG<br>45, 60, 80w/w% PG | 100 MHz to 2.02 GHz | -80° to 20°C | OECP | 1996 [11] |
| 1.3M DMSO+ HP9 perfusate | 434 MHz | -83° to 8°C | Resonant cavity | 1999 [12] |
| 50% DMSO with and without CPT perfusate | 27 MHz to 2.54 GHz | -75° to 25°C | Shielded coaxial open-circuit | 2000 [13] |
| DMSO+PVP<br>EG+PVP<br>PG+PVP | 434 MHz | -70° to 0°C | Single-mode resonant cavity | 2017 [14] |

# Methods

Coaxial probe description

Open-ended coaxial probe (OECP)- Keysight 85070E (high temperature probe, Keysight Technologies, CA, USA) was utilized to determine the dielectric properties of CPAs. OECP method, as one type of guided wave method, is useful for liquid, biological specimen or semi-solids characterization [15-17]. It is also classified as reflectometric method [18] since signal was generated and received from the same open-ended port. The advantage of coaxial probe method lies in its high accuracy, stable platform, noninvasive nature for measuring the electrical properties of materials and wide frequency band of operation [19, 20]. A calibration process is required for OECP measurement to refer the measured CPA value to the probe aperture plane. The process for known materials (usually air and water) was done for probe system before any measurement. The CPA measurement setup is shown in Figure 4.1A-D. After calibration, one port signal was sent

from the probe end to the CPA materials under test (MUT) and then returned. The CPA holder was adapted as ~10 ml for small volume study as shown in Figure 4.1A. To determine the dielectric properties of CPAs, the calculation of algorithm by using reflection signal is required. The dielectric property is represented by relative permittivity $\varepsilon_r = \varepsilon_r' - j\,\varepsilon_r''$ where $\varepsilon_r'$ is the relative dielectric constant and $\varepsilon_r''$ is the relative dielectric loss factor. Besides, the measured value of signal, is represented by the term of reflection loss $\Gamma^* = \Gamma\cos\varphi + j\Gamma\sin\varphi$, where $\Gamma$ is magnitude of the reflection coefficient and $\varphi$ is the phase. The translation of reflection loss to relative permittivity was adapted by the rational function method (RFM), which is recommended to apply for materials with high loss tangent (>0.5) [21-23]. RFM method offers improved accuracy ($\varepsilon_r' = \varepsilon_r' + 0.05|\varepsilon_r|$, $\varepsilon_r'' = \varepsilon_r'' + 0.05|\varepsilon_r|$) and allows the uncertainties in dielectric measurements to be quantified.

The brief relationship between reflection loss and relative permittivity is described as [24]:

$$\varepsilon_r' = \frac{-2\Gamma\sin\varphi}{\omega Z_0 C_0(1+2\Gamma\cos\varphi+\Gamma^2)} - \frac{C_f}{C_0} \quad (4.1)$$

$$\varepsilon_r'' = \frac{1-\Gamma^2}{\omega Z_0 C_0(1+2\Gamma\cos\varphi+\Gamma^2)} \quad (4.2)$$

Where $Z_0$ is characterization impedance of probe, $C_0$ is characterization capacitance of probe, $C_f$ is fringing capacitance of probe, which was determined by the calibration of water and air, $\varepsilon_r^*$ is relative permittivity of MUT.

CPA preparation

Individual CPA components used were Dimethyl Sulfoxide (DMSO), Ethylene Glycol (EG), Propylene Glycol (PG), Formamide bought from Sigma Aldrich (St. Louis, MO). CPA binary mixtures are prepared using graduated cylinders in volume (%v/v) ratio from which mole fraction is calculated later. Lastly, preparation of CPA cocktail mixtures was performed based upon components and composition listed in literature for M22 [25], DP6 [26] and VS55 [5]. Carrier solutions used were Euro-Collins (EC) for VS55, DP6 and LM5 for M22 and were also tested as part of individual components of CPA cocktail mixtures.

COMSOL modeling

Finite element analysis (FEM) was performed using the RF module of commercial package COMSOL 5.4 accessed using MSI, UMN. The modeled geometry is shown in Figure 2A with coaxial probe and sample around it. The wave equation is solved numerically to find electric field spatial distribution generated by open ended coaxial probe in the sample. The boundary conditions

and initial conditions are listed in Table 4.2. Lumped coaxial port was input to coaxial probe with 1.78V (15dB) voltage for 50-ohm impedance and a 90° port phase. Sample was assumed to be water as the worst-case analysis of smallest penetration depth.

Table 4.2: Details about COMSOL electric field modelling for OECP

<table>
<tr><td>Boundary Location</td><td>Boundary Condition</td><td>Initial Condition</td></tr>
<tr><td>r = 0 for all z</td><td>Symmetry</td><td rowspan="5">E =0</td></tr>
<tr><td>r = 0.5mm, 0 < z <15.5mm</td><td rowspan="2">Continuity</td></tr>
<tr><td>r = 1.65mm, 0 < z <15.5mm</td></tr>
<tr><td>r = 2.3mm, 0 < z <15.5mm</td><td rowspan="2">Perfect Electric Conductor</td></tr>
<tr><td>0< r <0.5mm & 1.65< r <2.3 mm, z = 15.5 mm</td></tr>
</table>

Dielectric measurement setup at subzero temperature

Measurement setup included various components such as VNA, OECP, CRF, laptop, thermometer and the sample CPA subjected to various temperatures. Figure 4.2E-G describes the permittivity measurement sequence steps. A vector network analyzer (VNA) with a probe system was calibrated so that the reflection coefficient measurements are referenced to the probe aperture plane. After calibration, the VNA sends a signal from one port to the liquids in the holder and then receives the reflection coefficient from the liquid-MUT. Measured frequency range is from 0.2 to 3 GHz. A 10 mL volume of sample is used for all the dielectric measurements. Sample is poured in a beaker as shown in Figure 4.2C, D and the coaxial probe is immersed/submerged (~ 5mm) under the sample. A T-type thermocouple (omega) is put near the probe at the top of the sample to monitor measurement temperature. The probe and sample setup is placed inside a control rate freezer (CRF) (Planar Kryo 560-II, Middlesex, UK). The cooling profile is set up at the fastest cooling rate (40°C/min) to the required measurement temperature (20, 10, 0, -10, -20, -30°C) and sample is kept for 10 min after reaching the desired temperature monitored by thermocouple reading using a thermometer. Data acquisition is then saved in ENA to record the ε', ε''. Sample is poured in a beaker as shown in Figure 4.2A and the coaxial probe is immersed/submerged (~ 5mm) under the sample.

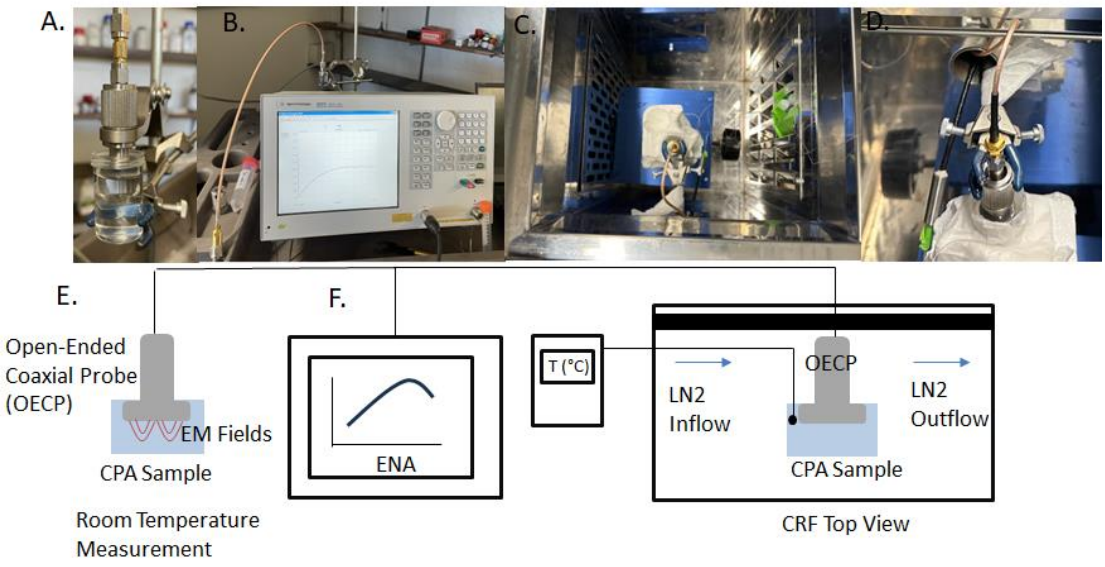


Figure 4.2. Measurement Setup. A. Photo of OECP submerged in CPA for room temperature measurement. B. Photo of VNA used along with OECP. C, D. OECP inside control rate freezer (CRF) for subzero temperature measurement. E. Schematic of OECP measurement alongside data acquisition by F. VNA. Schematic showing OECP inside CRF.

## Results

We first calculated penetration depth of RF fields for our open-ended coaxial probe. COMSOL Depth of ~1mm is found where electric fields fall to 1/e (~37%) of its maximum value as shown in Figure 4.3C. Further, as expected farther away from probe the field falls in radial as well as z direction. These results are assuming water as the measurement sample, now given that pure water has higher dielectric loss than CPAs therefore it will have most absorption and hence smallest penetration depth therefore our analysis gives the minimum penetration depth. Since, at higher frequencies, penetration depth seems to be reduced further as expected in Figure 4.3C (~1.2mm at 200MHz to ~0.8 mm at 3GHz). Therefore, we submerged the probe inside the CPA samples at least 0.8 mm deep for ensuring accurate bulk penetration. Our probe measurement was first calibrated to the literature values of water and CPAs-glycerol and DMSO where it agrees majorly (for 85% glycerol measured ε', ε'' as ~ 20.6, 16.9 at 0.98 GHz and 13.4, 12.3 at 2 GHz respectively which agrees with reported values in past 21, 17 at 0.98 GHz and 14, 12 at 2.02 GHz [11]).

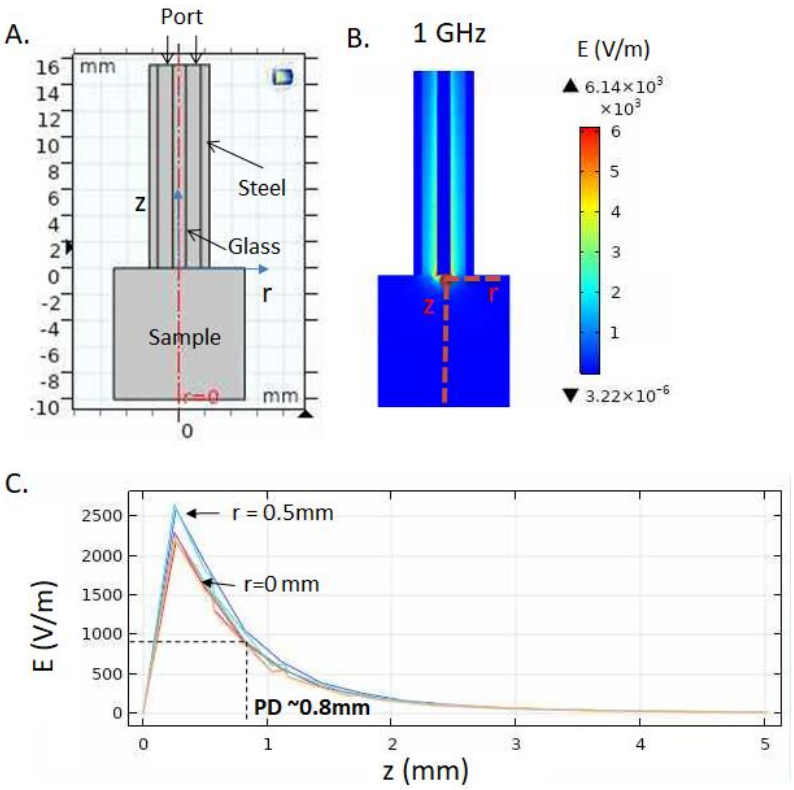


Figure 4.3. A. Modeled COMSOL geometry of coaxial probe with CPA. B. Representative case of electric field distribution around the probe at 1 GHz. C. Plot of electric field vs depth (z) direction at 1 GHz at different radial locations. Penetration depth is estimated as PD: z @ E = 1/e $E_{max}$ ~ 37% $E_{max.}$

Dielectric behavior for individual CPA components as function of frequency (1-3 GHz)

First, we measured dielectric constant and loss for binary aqueous CPA mixtures as function of frequency to understand the effect of components in a CPA cocktail. This was performed at room temperature as a simple case to avoid any temperature dependence and isolate effect of chemical mixture addition. It is observed that DMSO-water mixtures show unique behavior with mixture loss value being higher than the individual component i.e. 100% DMSO and pure water (100% water) as plotted in Figure 4.4C. The red region in heat map plot of Figure 4.4C shows the intermediate concentration/mole fraction of DMSO where the maximum dielectric loss is highest than any other combination tested. PG water mixture also shows a similar behavior as seen in Figure 4.4B. Formamide mixture on the other hand shows more common behavior with dielectric loss values within the bounds of pure water and 100% formamide (evident in Figure 4.4A).

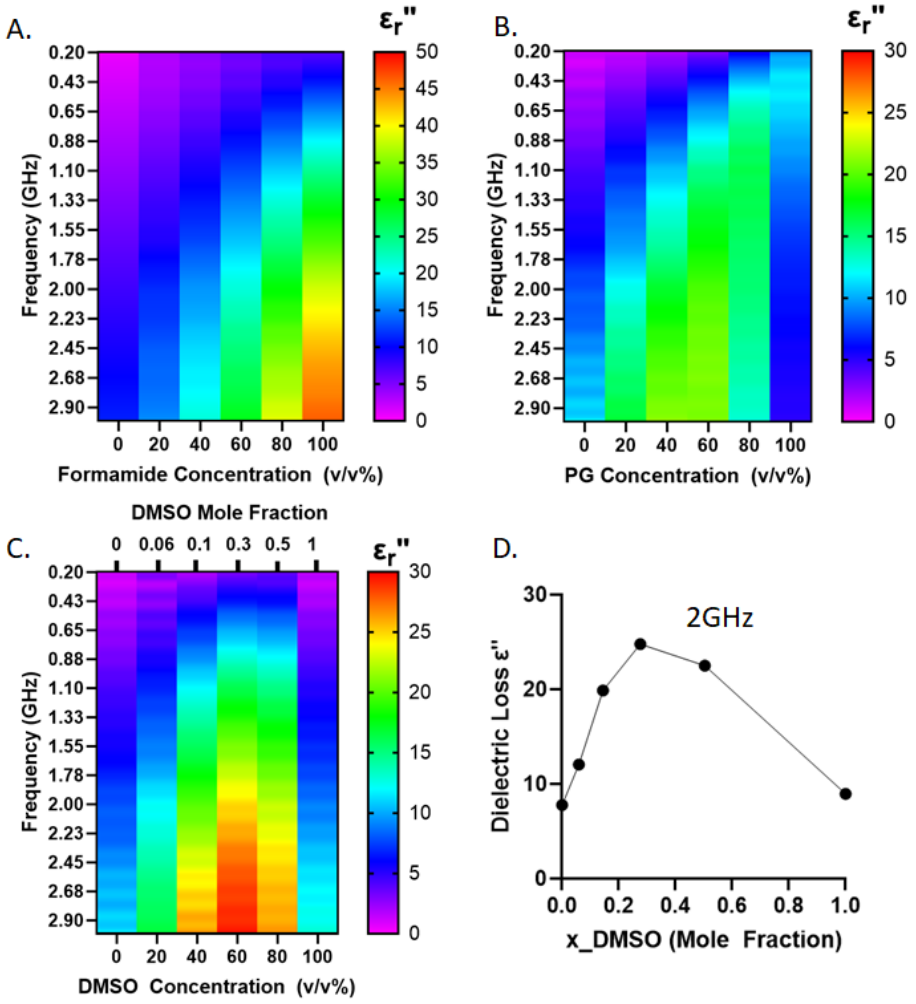


Figure 4.4. A. Heat map plot showing the dielectric loss for A. Formamide+water, B. Propylene Glycol (PG)+water and C. DMSO+water mixture for the complete frequency range. D. Dielectric loss as function of DMSO mole fraction at a representative frequency of 2 GHz.

Further, binary mixture of two CPA components such as DMSO+PG and DMSO+Ethanol revealed that roughly closer to ~80%v/v DMSO combination with PG (20%v/v) or Ethanol (20%v/v) produces the highest dielectric loss (ε''~15-17 yellow region in Figure 4.5A and B).

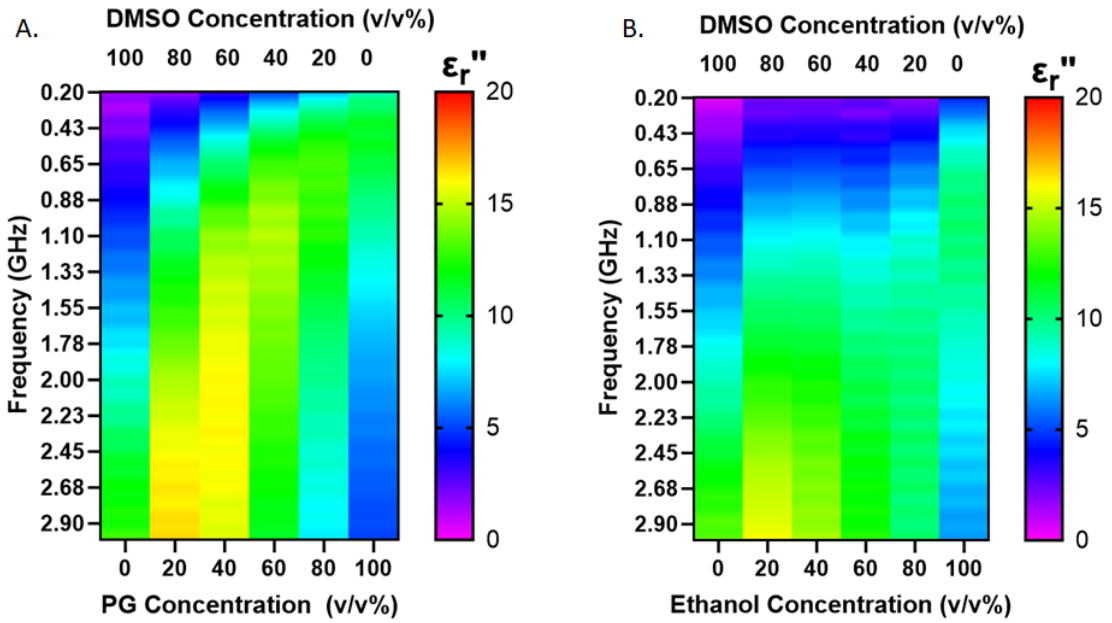


Figure 4.5. Heat map plot showing the dielectric loss for binary CPA+CPA mixtures A. DMSO+PG B. DMSO+Ethanol for the complete frequency range. Concentration (%v/v) is listed on bottom and top for each component.

After learning from mixture behavior, we investigated common organ vitrification CPA cocktails namely M22, VS55 and DP6 to understand the contribution of individual constituents/components in a CPA cocktail. All these measurements were performed at room temperature for simplicity. Dielectric loss of individual CPA components was measured where formamide seems to have highest (ε''~25-60) and propylene glycol exhibit the lowest (5-20). Carrier solutions such as LM5 dielectric loss doesn't change significantly (~10) over the frequency range analyzed (0.2-3 GHz) whereas EC loss seems to decrease from 20 to ~10 as increasing frequency from 1 to 3GHz. DMSO loss increases as we move from low to high frequency whereas PG decreases (Figure 4.4A). All the 3 CPA cocktail mixtures i.e. M22, DP6, VS55 interestingly show similar dielectric loss at room temperature throughout the frequency range analyzed (1 to 3 GHz).

As can be seen in Figure 4.6D a peak (inverted U-curve) for dielectric loss factor occurs at near 0°C for all 3 CPA cocktails. This peak shifts to lower temperatures (towards cryogenic) at lower frequencies (Figure 4.6C- peak not visible <-40°C). Hence, at very low frequencies (kHz to few MHz) the dielectric loss peak shifts to further lower/cryogenic temperatures which has been observed in past studies as well [11, 13]. Note that VS55 showed the highest dielectric loss values

(peak~ 39) when compared to M22 (peak~33) and DP6 (peak~ 32) in the whole measured frequency and temperature range.

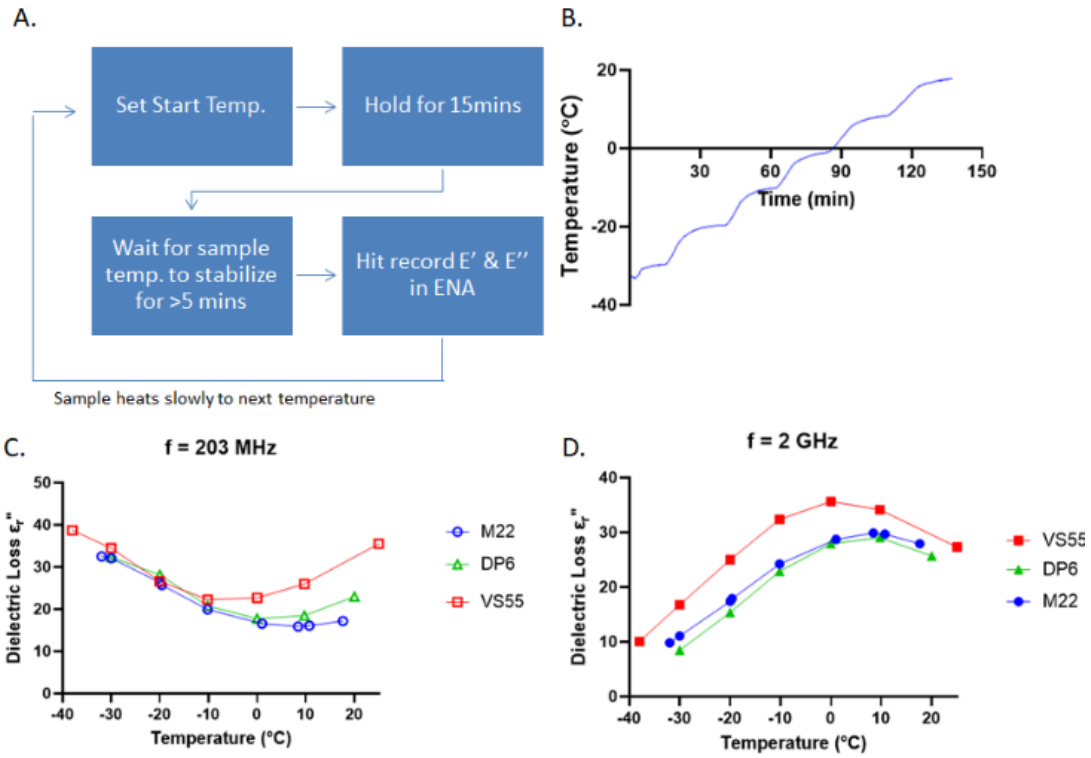


Figure 4.6. A. Flowchart showing the steps executed in subzero dielectric measurement of CPAs in CRF. B. Temperature vs time curve for CPA sample during dielectric measurement with OECP. Dielectric loss for all the 3 CPA cocktail mixtures M22, VS55, DP6 as function of subzero temperatures at two representative frequencies C. ~200 MHz, D. 2 GHz.

Further, we plotted a heat map plot to visualize the dielectric loss behavior with frequency and temperature as shown in Figure7. Dielectric loss peak moves to lower temperature at lower frequencies (see red color region in heat map of Figure 6A).

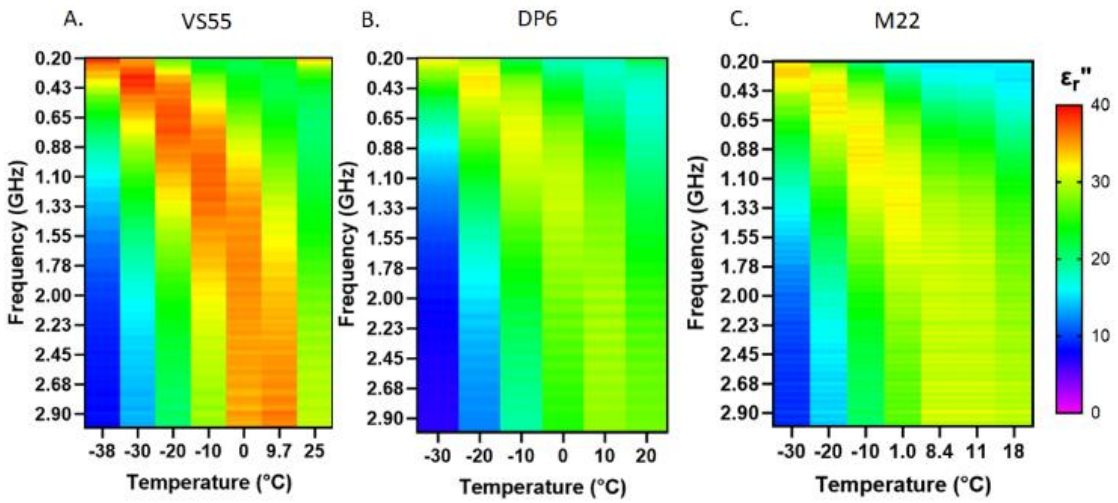


Figure 4.7. Heat map color plots of measured dielectric loss for CPAs: A. VS55, B. DP6 and C. M22 as function of frequency and temperature.

# Discussion

The behavior of mixture dielectric loss tendency to be higher than its individual components has been observed in literature such as for DMSO-water aqueous mixtures [27]. Interestingly, it was observed that dielectric rotational relaxation time peaked at an intermediate mole fraction (~0.33) of DMSO which agrees with our observation (Figure 3D). It was suggested due to decrease in number of hydrogen (H) bonds among water molecules with increase in DMSO mole fraction because of increase in number of H-bonds between DMSO and water molecules which may be stronger and have longer lifetime. It can be conceived that dipole-dipole interactions among these DMSO mixtures would affect the rotational dielectric relaxation in CPA solutions. DMSO molecules reduced the potential barrier for dipole reorientation in a mixture solution. Another study [28] reported in past, that static dielectric constant and relaxation time for DMSO binary mixtures such as DMSO-ethanol, DMSO-propan-1-ol where it was found that solute-solvent interactions in a mixture govern the relaxation time behavior. Therefore, CPAs with DMSO rich mixtures may show this increase in dielectric loss at intermediate molar fractions (or concentrations) of DMSO dominating the mixture dielectric behavior.

Note that dielectric loss shows a typical peak with temperature (inverted U-curve) because the relaxation heat losses are maximum where the relaxation time $\tau$ (governed by physical state and viscosity) is equal to the time of applied alternating electric field ($1/f_p$). Now as the temperature is further lowered to cryogenic below its glass transition temperature, viscosity of CPA solutions increases exponentially which would imply excessively longer relaxation times (to resist molecular viscous forces) and therefore negligible dielectric loss values due to lack of mobility of polar molecules in glassy solid-like state. To heat at MHz frequencies using dielectric rewarming, dielectric loss of CPA would need to be balanced especially at near zero temperatures (above its melt temperature) to control ionic heating and avoid thermal runaway [10]. Since dielectric loss is a function of temperature, therefore the warming rate would also vary with temperature. As the sample is heated from lower temperatures (e.g., from -100°C) dielectric loss (and so is warming rate) will increase to a peak and then decrease back near zero temperature (for a CPA with inverted U-curve dielectric loss). One way to avoid this temperature dependency (or non-uniformity) of warming rate could be by frequency sweep from smaller to larger (e.g., 27 MHz to 2.5 GHz in case of 50%DMSO [13]) as temperature is raised from low (~ -100°C) to high (~0°C) during transient rewarming. This is possible because dielectric loss peak value shifts to higher temperatures at larger frequencies. Though spatial non-uniformity in dielectric rewarming would still be a challenge because of shorter penetration depths and uneven CPA (hence polar molecules) distribution inside tissue of a perfused organ. These guidelines would guide in design of CPA and their carrier solutions for nanowarming (require smaller dielectric loss and electrical conductivity) and dielectric rewarming (larger dielectric loss with peak loss at lower subzero temperatures). One concept to be yet fully explored is combination of dielectric heating with RF rewarming i.e. nanowarming. It is known that theoretical nanoparticle heating (specific absorption rate-SAR) increases with frequency before it may saturate in MHz ranges [29, 30] which needs to be tested experimentally. If so, this can help in achieving successful rewarming rates at very low IONPs concentration (~0.1-1 mgFe/mL) as shown in one study [31] than currently used in organs (~10 mgFe/mL in vasculature [5, 32-35]).

Moreover, recent study [36] has shown unique ways where dielectric property measurement can also serve as ischemia-injury or quality assessment during normothermic machine perfusion for cryopreserving organ. Therefore, future work should investigate not only the CPA dielectric properties in further lower temperatures (< -40°C) but also electrical properties for tissues and organs perfused with CPAs which can be directly corelated to a cryopreservation protocol.

# Conclusion

This study we investigated dielectric properties of common organ vitrification CPA solutions (M22, DP6, VS55) and their components where all three CPAs seem to have similar dielectric loss with decreasing loss at lower temperatures for larger frequencies (>2GHz) and increasing loss at smaller frequencies (<400MHz). For CPA mixtures, dielectric loss can be higher than its individual components loss values due to effects such as polar molecules H-bonding rearrangements. Formamide seems to be the highest lossy component over others and should be included in dielectric heating CPA design whereas be omitted for RF rewarming (nanowarming) to avoid thermal runaway (induced by eddy heating). Overall, the temperature heat map plots provide a firsthand guide for choosing the best frequency and CPA for subzero rewarming of cryopreserved biomaterials (such as partial freezing, supercooling). Future work should investigate dielectric properties of organ vitrification CPAs and tissues permeated with them at cryogenic temperatures (<-40°C to -150°C) for rewarming of vitrified organs.

# References for Chapter 4


1. Wowk, B., et al., *27 MHz constant field dielectric warming of kidneys cryopreserved by vitrification.* Cryobiology, 2024. **115**: p. 104893.
2. Ren, S., et al., *Single-mode electromagnetic resonance rewarming for the cryopreservation of samples with large volumes: A numerical and experimental study*. Biopreservation and Biobanking, 2022. **20**(4): p. 317-322.
3. Rajotte, R., et al., *Preservation studies on canine kidneys recovered from the deep frozen state by microwave thawing.* Proceedings of the IEEE, 1974. **62**(1): p. 76-85.
4. Burdette, E.C., et al., *Microwave thawing of frozen kidneys: A theoretically based experimentally-effective design.* Cryobiology, 1980. **17**(4): p. 393-402.
5. Sharma, A., et al., *Vitrification and Nanowarming of Kidneys.* Advanced Science, 2021. **8**(19): p. 2101691.
6. Etheridge, M.L., et al., *RF heating of magnetic nanoparticles improves the thawing of cryopreserved biomaterials.* Technology, 2014. **2**(03): p. 229-242.
7. Ecker, H., E. Burdette, and F. Cain. *Simultaneous microwave and high frequency thawing of cryogenically preserved canine kidneys*. in *Record of the IEEE International Symposium on Electromagnetic Compatibility*. 1976.
8. Mizushima, S.-i., *On the anomalous dispersion and absorption of electric waves. I.* Bulletin of the Chemical Society of Japan, 1926. **1**(3): p. 47-53.
9. Morgan, S., *Two types of dielectric polarization.* Transactions of The Electrochemical Society, 1934. **65**(1): p. 109.
10. Marsland, T., S. Evans, and D. Pegg, *Dielectric measurements for the design of an electromagnetic rewarming system.* Cryobiology, 1987. **24**(4): p. 311-323.
11. Michelson, S. and S. Evans, *Dielectric properties of supercooled cryoprotectant agents.* Physics in Medicine & Biology, 1996. **41**(10): p. 2053.

12. Robinson, M.P. and D.E. Pegg, *Rapid electromagnetic warming of cells and tissues.* IEEE transactions on biomedical engineering, 1999. **46**(12): p. 1413-1425.
13. Evans, S., *Electromagnetic rewarming: the effect of CPA concentration and radio source frequency on uniformity and efficiency of heating.* Cryobiology, 2000. **40**(2): p. 126-138.
14. Pan, J., et al., *Determination of dielectric properties of cryoprotective agent solutions with a resonant cavity for the electromagnetic rewarming in cryopreservation.* Biopreservation and Biobanking, 2017. **15**(5): p. 404-409.
15. Aydinalp, C., et al., *Characterization of Open-Ended Coaxial Probe Sensing Depth with Respect to Aperture Size for Dielectric Property Measurement of Heterogeneous Tissues.* Sensors (Basel), 2022. **22**(3).
16. Dilman, I., M.N. Akinci, and M. Cayoren, *Complex Dielectric Permittivity Measurements Using a Rational Functional Method with Arbitrary Open-Ended Coaxial Probes*, in *2021 29th Telecommunications Forum (TELFOR)*. 2021. p. 1-4.
17. Shim, J.-Y. and J.-Y. Chung, *Complex Permittivity Measurement of Artificial Tissue Emulating Material Using Open-Ended Coaxial Probe.* IEEE Sensors Journal, 2020. **20**(9): p. 4688-4693.
18. Aydinalp, C., et al., *Characterization of Open-Ended Coaxial Probe Sensing Depth with Respect to Aperture Size for Dielectric Property Measurement of Heterogeneous Tissues.* Sensors, 2022. **22**(3).
19. Aimoto, A. and T. Matsumoto, *Noninvasive method for measuring the electrical properties of deep tissues using an open-ended coaxial probe.* Medical Engineering & Physics, 1996. **18**(8): p. 641-646.
20. Raghavan, S. and M. Ramaraj, *An Overview of Microwave Imaging towards for Breast Cancer Diagnosis.* Piers 2012 Moscow: Progress in Electromagnetics Research Symposium, 2012: p. 627-630.
21. Habibi, M., D.P. Klemer, and V. Raicu, *Two-dimensional dielectric spectroscopy: Implementation and validation of a scanning open-ended coaxial probe.* Review of Scientific Instruments, 2010. **81**(7).
22. Cole, K.S. and R.H. Cole, *Dispersion and absorption in dielectrics I. Alternating current characteristics.* Journal of Chemical Physics, 1941. **9**(4): p. 341-351.
23. Evans, S. and S.C. Michelson, *Intercomparison of dielectric reference materials available for the calibration of an open-ended probe at different temperatures.* Measurement Science and Technology, 1995. **6**(12): p. 1721-1732.
24. *<cdc_10047_DS1.pdf>*.
25. Fahy, G.M., et al., *Physical and biological aspects of renal vitrification.* Organogenesis, 2009. **5**(3): p. 167-175.
26. Y, R., et al., *Cryomacroscopy of vitrification, Part I: A prototype and experimental observations on the cocktails VS55 and DP6.* Cell preservation technology, 2005. **3**(3).
27. Lu, Z., et al., *Dielectric relaxation in dimethyl sulfoxide/water mixtures studied by microwave dielectric relaxation spectroscopy.* The Journal of Physical Chemistry A, 2009. **113**(44): p. 12207-12214.
28. Khirade, P., et al., *Static dielectric constant and relaxation time measurements on binary mixtures of dimethyl sulfoxide with ethanol, 2-ethoxyethanol, and propan-1-ol at 293, 303, 313, and 323 K.* Journal of Chemical & Engineering Data, 1999. **44**(5): p. 879-881.
29. Rosensweig, R.E., *Heating magnetic fluid with alternating magnetic field.* Journal of magnetism and magnetic materials, 2002. **252**: p. 370-374.
30. Jordan, A., M.L. Etheridge, and J.C. Bischof, *-Magnetic Nanoparticles for Cancer Therapy*, in *Physics of Thermal Therapy*. 2016, CRC Press. p. 310-335.
31. Pan, J., et al., *Investigation of electromagnetic resonance rewarming enhanced by magnetic nanoparticles for cryopreservation.* Langmuir, 2018. **35**(23): p. 7560-7570.

32. Chiu-Lam, A., et al., *Perfusion, cryopreservation, and nanowarming of whole hearts using colloidally stable magnetic cryopreservation agent solutions.* Science advances, 2021. **7**(2): p. eabe3005.
33. Sharma, A., et al., *Cryopreservation of whole rat livers by vitrification and nanowarming.* Annals of Biomedical Engineering, 2023. **51**(3): p. 566-577.
34. Gao, Z., et al., *Vitrification and rewarming of magnetic nanoparticle-loaded rat hearts.* Advanced Materials Technologies, 2022. **7**(3): p. 2100873.
35. Han, Z., et al., *Vitrification and nanowarming enable long-term organ cryopreservation and life-sustaining kidney transplantation in a rat model.* Nature Communications, 2023. **14**(1): p. 3407.
36. Hou, J., et al., *Utilization of dielectric properties for assessment of liver ischemia reperfusion injury in vivo and during machine perfusion.* Scientific Reports, 2022. **12**(1): p. 11183.

# Chapter 5. Physical Success of Cryopreservation in Liter Volumes

This chapter presents the work of the first successful physical demonstration of vitrification in a human organ scale (up to 3L CPA and porcine liver) and nanowarming (up to 2L CPA). The body of work is in submission. The manuscript is reproduced here:

**Gangwar, Lakshya**, et. al. " Physical success of cryopreservation by vitrification and nanowarming in human organ scale volumes." (2024) In Submission.

# Overview

Advances in scalable vitrification ("ice free" cryopreservation) may one day support organ banking, thereby revolutionizing transplant medicine. However, achieving a glassy or vitrified state and returning from it has never been demonstrated in the literature at the human organ scale. One reason is that rewarming sufficiently rapidly and uniformly to avoid crystallization, or cracking is much more difficult to achieve than during cooling. To address this, our group has spent the last decade developing nanowarming, a volumetric rewarming approach that achieves fast and sufficiently uniform rewarming through radiofrequency activation of iron oxide nanoparticles (IONP) entrained in cryoprotective agents (CPAs). Using convective cooling protocols optimized through heat transfer modeling to vitrify and nanowarming to rewarm, we tested 0.5 – 3 L volumes of three common CPA solutions: M22, VS55, and 40% EG+0.6M Sucrose. First, we demonstrate our ability to cool faster than the critical cooling rates (CCR) of the CPAs while also maintaining adequate uniformity to avoid cracks. Vitrification success was verified by optical, thermometric, and micro-CT inspection. While both M22 and EG+Sucrose were able to vitrify in 0.5 L, 1 L bags, only M22 was able to vitrify at 3 L and VS55 did not vitrify in any tested volumes. As further proof of principle for scaled vitrification, a porcine liver (~1L) was perfusion loaded with 40% EG+0.6M Sucrose and was successfully vitrified. Uniform volumetric rewarming was then achieved in a 2 L volume (M22 with ~5 mgFe/mL IONP) using nanowarming at ~85 °C/min with a 120 kW radiofrequency (RF) coil (35 kA/m and 360 kHz). This work demonstrates that human organ scale vitrification and rewarming is physically possible, thereby contributing to technology that may one day allow human organ banking.

# Introduction

Vitrification, or the rapid cooling of biologic material to an ice-free glassy state at ultralow temperature, is a potential method to achieve indefinite cryopreservation of cells, tissues, and organs for transplantation or other biomedical applications [1, 2]. Over a century ago, the first successful vitrification of frog spermatozoa was conducted by Luyet and Hodapp (in 1938) [3, 4]. Subsequently, vitrification has been performed on multiple biological systems, culminating in whole rabbit organs (a kidney) in the 10s of mL by the 1980s [1]. Since that time, slow freezing has been shown in a liter scale system [5, 6], and vitrification has been demonstrated up to 1.5L with limited success due to underlying ice formation and fracture at such large volumes. [7]. However, these studies still suffered from an inability to reproducibly rewarm these bulk systems sufficiently rapidly or uniformly while avoiding ice formation or cracking [8].

One approach to address the challenges of rewarming is through volumetric rewarming techniques such as high intensity focused ultrasound (HIFU), dielectric/microwave warming or nanowarming. HIFU heats by focusing sound/pressure waves but currently is limited to ≤ 2 mL [9]. It also has the inherent limitation of wave reflections, acoustic impedance mismatch at interfaces, cavitation, and the possibility of burning when in the liquid phase above the melting temperature ($T_m$) [10, 11]. In the case of dielectric/microwave rewarming (heating of dipolar molecules by electromagnetic (EM) waves), volumes can approach ~100 mL in CPA systems [12] and, most recently, in rabbit kidneys (~50 mL) [13]. However, this approach also has several limitations, including small penetration depths, inability to heat in the vitrified "solid" state, and potential for "thermal runaway" near the melt [14]. A further volumetric approach entitled "nanowarming" where heat is generated in presence of alternating magnetic fields via magnetic nanoparticles which are perfused inside the organ vasculature. This approach nanowarming, in theory, is fully scalable to human organ scales. So far, we and others have published on sample volumes up to 80 mL CPA mL and 30 mL biological nanowarming at rates up to 50 -100 °C/min [15-20].

To achieve vitrified cryopreservation of human organs, we anticipate needing 0.5 - 1 Liter cryobags for hearts and kidneys, while human livers may require ≥ 3 L volumes [21]. Nanowarming heating rates are produced from iron-oxide nanoparticles (IONPs) which are perfused inside the vasculature of an organ therefore heating is generated within an organ or sample volume. Therefore, the scale of sample does not matter in nanowarming rates rather amount of IONPs, and magnetic field, frequency dictate the heating rates. However, convective cooling will be directly impacted by the size of the system, with the cooling rate at the center of the sample decreasing as the size of the system increases [22]. This may lead to insufficient cooling rates and/or physical fractures/cracking due to thermal gradients and ensuing stress beyond a CPA's tensile strength [23]. In other words, in contrast to prior studies in rodent and rabbit organs where rewarming was the main barrier to success [refs], cooling conditions may be the rate-limiting step in vitrifying and rewarming human organ scale volumes.

This study was designed to specifically test whether physical vitrification and nanowarming can be achieved in human organ scale volumes. Here, we report the successful vitrification of CPA samples up to 3L and nanowarming up to 2L from the vitrified cryogenic state. We further demonstrate physical vitrification in a CPA-perfused liver (~1L porcine liver). In summary, this study demonstrates that bulk systems equal to the size of human organs can be vitrified and nanowarmed, as verified by optical, thermometric, and µCT. These findings lay the groundwork

for scaling up cryopreservation to clinical-scale human organs using common CPAs and carefully designed cooling and nanowarming protocols.

Table 5.1: Literature review of scale from major studies where vitrification and rewarming of biological systems (organs) and physical systems (CPAs) have been reported.

| Volume | Biological system | Technique | Notable References (Author & Journal) |
|---|---|---|---|
| 5 µL | Frog Spermatozoa | Vitrification and Convective Rewarming | [3] |
| 0.2 mL | Human Ovarian Tissue | Vitrification and Convective Rewarming | [24] |
| 0.2 mL | Mouse Embryos | Vitrification and Convective Rewarming | [25] |
| 10 mL | Rabbit Kidney | Vitrification | [1] |
| 1-2 mL | Rabbit Jugular Vein & Articular Cartilage | Vitrification and Convective rewarming | [26, 27] |
| 5-10 mL | Sheep Ovaries | Vitrification and Convective rewarming | [28] |
| 10-20 mL | Rat Heart + IONPs+CPA surrounding solution | Vitrification and Nanowarming | [18, 19] |
| | | | [15-17] |
| 20-25 mL | Rat Kidney + IONPs + CPA surrounding solution | | |
| | | | [20] |
| 25-30 mL | Rat Liver + IONPs + CPA surrounding solution | | |

| | | | |
|---|---|---|---|
| 1-80mL | Porcine Arteries, Heart Valves, CPA+IONPs Solutions | | [8] |
| 80-90 mL | Porcine & Sheep Heart Valves + CPA surrounding solution | Vitrification and 2-stage Convective rewarming | [29, 30] . |
| 0.5-3L | CPAs (VS55, M22, EG+Sucrose) | Vitrification and Nanowarming | "Current study" |
| 100mL - 1.5L | Porcine & Human Organs | Vitrification and Rewarming | To be demonstrated (Future Cryopreservation Goal) |

# Methods

CPA and IONP Preparation

The three most common organ vitrification CPAs used in this study are M22, VS55, and 40%v/v EG+0.6M Sucrose, prepared according to their formulations and composition as listed in Supplementary Table S5.1. These CPAs were chosen due to their increasing use in multiple organ systems, such as VS55 in rat hearts and kidneys [15, 17-19], M22 in rabbit kidneys [31], and 40%v/v EG+0.6M Sucrose in rat livers [20].

Commercially available iron-oxide nanoparticles (IONPs) EMG308 (Ferrotec, Bedford, USA) (~10 nm) were used to prepare CPA + IONP mixture solutions. EMG308 was suspended in M22 with modified carrier solution (instead of LM5) to ensure the stability of these IONPs (see stability data Figure S5.1).

Heat Transfer Finite Element Modeling (FEM)

Computational modeling was performed using a commercial FEA package (COMSOL 5.4). A 3D CAD geometry of cryobag filled with CPA was created and simulated in COMSOL for heat transfer simulations, as shown in Figure S5.2. Three cryobag volumes were simulated (0.5, 1L, 3L) with dimensions close to experimental values of polyethylene bags used experimentally (see supplementary on cryobag FEM). Details regarding governing equations, boundary conditions, initial conditions, and geometry are provided in the supplementary text and Table S5.2. For

simplicity, all the cooling and warming rates are reported in the 0 to -100°C temperature range for experiments and modeling, as this temperature range is most prone to the growth of ice crystallization in CPAs [32]. Practically speaking, ice growth would be restricted to the Tm of CPAs (see Table S1 for $T_m$) ($T_m$ to -100°C); therefore, our rate calculations (from are conservative worst-case analyses as they encompass all the different $T_m$ of CPAs.

Vitrification Experiments

Three volumes- 0.5, 1, and 3L were evaluated for vitrification success. These volumes are in the range of the largest organs in a human, for example, the brain and liver, as also mentioned in Table 5.2. Polyethylene plastic "cryobags" of 2 mm thickness (McMaster Carr, Elmhurst, USA) were used to contain the CPA and organ samples. Cryobags were heat-sealed at the top using an external clip to minimize air pockets and avoid ice nucleation at the CPA-air interface. A controlled rate freezer (CRF) (Planar Kryo 560-II, Planar, Middlesex, UK) was used to execute cooling protocols for vitrification. Finally, vitrified samples were stored inside a -150°C cryogenic mechanical freezer (MDF-C2156VANC-PA, Panasonic, IL, USA). Physical vitrification was verified by optical transparency by visual inspection and photography. Temperature measurements were conducted using fiber optic temperature probes and a four-channel monitoring system (Qualitrol, Fairport, NY, and Micronor Sensors, Ventura, CA, USA). They were recorded at either 1 or 2-second intervals using FO Temp Assistant Software or Optilink Software (provided by the manufacturer). The probes were pre-calibrated for any offset in the cryogenic temperature range.

Porcine Liver Perfusion and Vitrification

The University of Minnesota's Institutional Animal Care and Use Committee (IACUC) approved this study. Porcine livers were recovered from male, 20-30kg, Yorkshire pigs from local vendors. Animals were injected intravenously with 300 IU heparin prior to euthanasia. After euthanasia, the abdomen was rapidly opened, the abdominal aorta and portal vein were cannulated, the thoracic aorta was cross-clamped, the suprahepatic vena cava (SHVC) was vented, and organs were flushed immediately with 5L of a cold Histidine-Tryptophan-Ketoglutarate (HTK) solution. Once the flush was complete, the liver was explanted and placed in cold HTK solution for transport. After back table preparation, the porcine liver was perfused via the portal vein with 40%EG+0.6M Sucrose in a step-loading protocol similar to that published for rat liver literature [20]. Specifically, 10%EG and 25%EG were perfused for 15 minutes each, followed by 40%EG+0.6M sucrose for 70 minutes at a constant flow rate of ~65 mL/min, as shown in Figure S5.5. More details can be found in the supplementary information.

μCT Imaging for verification of vitrification

In addition to taking photos of CPAs, we used microcomputed tomography (μCT) to verify physical vitrification. We designed a new micro-CT scanning container to hold 0.5-1L samples, scaled up from the previous 20 mL system [33] and sufficient for porcine livers. The samples were scanned in a micro-CT imaging system NIKON XT H 225 (Nikon Metrology, MI, USA) for 500mL volumes. Detailed information about μCT settings and image reconstruction can be found in supplementary information.

Nanowarming Experiments

To enable nanowarming of liter scale CPA samples, we used a custom-built 120 kW Radiofrequency coil (RF coil) (AMF Life Systems, Auburn Hills, MI, USA). Coil details are given in Table S5.4. First, 0.5, 1, and 2L M22 with EMG308 were vitrified in heat-sealed cryobags with cylindrical shapes that fit within the RF coil. Three fiber optic temperature probes were placed in the center, left, and right regions of the cryobag ~4cm apart for all volumes 0.5, 1, and 2L with the help of a 3D printed jig (Figure S19). After vitrification, samples were stored overnight at -150°C in a cryogenic freezer (MDF-C2156VANC-PA, Panasonic, IL) prior to nanowarming. During rewarming, the temperature is recorded every 1 sec after vitrified cryobags were placed inside an insulated RF Coil holder situated in the center of the coil treatment region.

RF Coil Characterization (120kW)

Our custom-built RF coil was characterized by measuring magnetic field variation from low to high values and the field strength spatial distribution. To determine magnetic field strength (axial and radial component), we used a 2D high frequency RF probe (AMF Life Systems) placed inside the RF coils. We used an oscilloscope (LA354, LeCroy, NY) to record the voltage signals, which were then converted to magnetic field values. Using modeled magnetic field distribution, we compared spatial uniformity between the previously characterized 15kW [8] and the new 120 kW RF coils, as shown in Figure S5.14. Note that the larger power rating is needed to produce a uniform magnetic field within larger coil volumes up to 2.5 L. The supplementary materials provide a detailed description of the RF coil in Figures S5.15-S5.16 and Table S3.

SAR Measurements

Specific absorption rates (SAR) measurements were executed on a 1mL sample volume of CPA with nanoparticles (EMG-308, pIONPs) in a cryovial. The cryovial was placed inside the RF coils

(15, 120kW system) within a 3D-printed holder, and the temperature was recorded using fiber optic temperature probes. SAR was then calculated using the time rise method described in detail in the literature [34, 35] (Figure S5.17).

Data analysis

All the graphs in the figures are plotted using GraphPad Prism 10. A total of 3 replicates are conducted for all the cooling, nanowarming, and SAR experiments. The number of replicates is listed in each figure legend. Theoretical SAR is calculated using MATLAB, and numerical FEM is performed in COMSOL.

# Results

The steps required for vitrification and nanowarming of liter-scale volumes are overviewed in Figure 5.1. First, liter volumes of a CPA (0.5-3L) are placed inside cryobags. The cryobags are placed inside a controlled rate freezer (CRF), where cooling protocols are executed. After vitrification, the samples are stored at cryogenic temperature (-150C) until rewarming. Traditional rewarming employs convection using a water bath, which at these scales results in ice recrystallization and/or fractures (failure modes) due to insufficient rewarming rates (slow) and thermal stresses (non-uniform) (lower section of the flow chart). For nanowarming (top section of the flow chart), the cryobag is vitrified with iron oxide nanoparticles (IONPs) suspended in the CPA. The vitrified cryobag is placed inside the RF coil, alternating magnetic fields are turned on, and rewarming occurs by oscillation of the IONP as they traverse their hysteresis cycle [36]. This leads to successful (rapid, uniform) rewarming, avoiding crystallization or cracking failure modes.

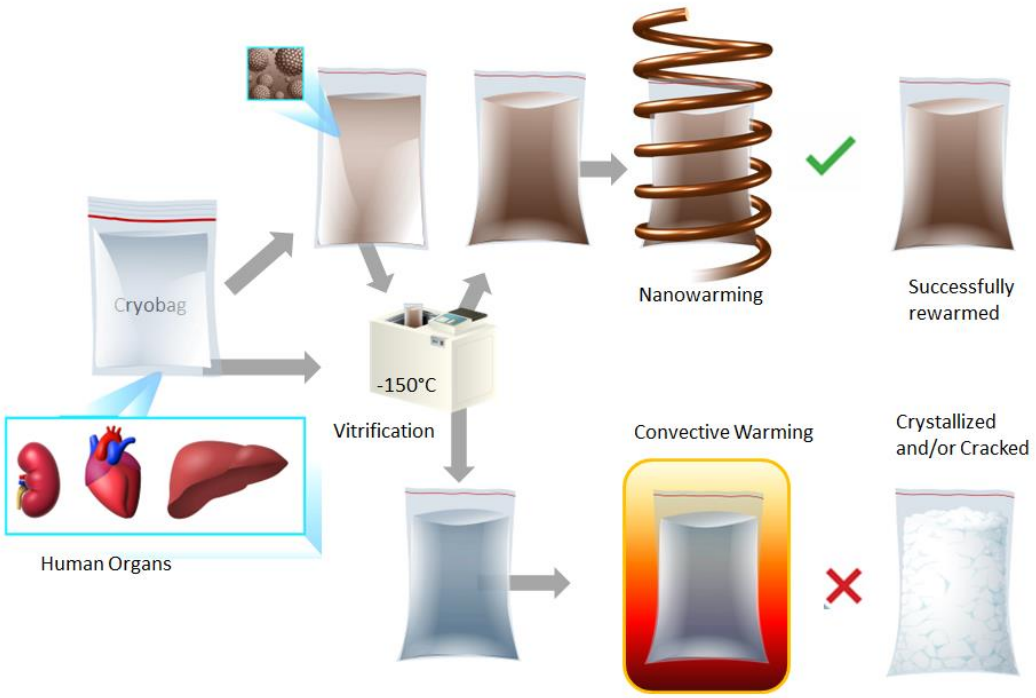


Figure 5.1: Schematic flow of steps (left to right) in liter scale vitrification and rewarming. Liter volumes of a CPA (0.5-3L) are put inside a sufficiently large cryobag. These larger cryobags can potentially hold a human organ for reference. Cryobag is then placed inside a controlled rate freezer (CRF) where vitrification cooling protocol is executed. For nanowarming (top section of the flow chart), the cryobag is vitrified with iron oxide nanoparticles (IONPs) suspended in the CPA. The vitrified cryobag is placed inside the RF coil, alternating magnetic fields are turned on, and rewarming occurs by oscillation of the IONP as they traverse their hysteresis cycle. This leads to successful (rapid, uniform) rewarming, avoiding crystallization or cracking failure modes. Traditional rewarming employs convection using a water bath, which at these scales results in ice recrystallization and/or fractures (failure modes) due to insufficient rewarming rates (slow) and thermal stresses (non-uniform) (lower section of the flow chart).

The success or failure of vitrification in these systems can be verified by optical, thermal, and µCT measurements. Visually, ice can be identified as round spherulites during crystallization (Figure S5.8A) or by opaque, milky-white/cloudy appearance throughout the sample in case of complete crystallization (Figure S5.8B). Another mode of physical failure is fractures or cracking, which can be recognized in CPA geometry, as observed in Figure S5.9 as the presence of linear opacities. In the absence of failure modes (partial/complete crystallization and fractures), the CPAs look clear, transparent, and glassy, implying successful vitrification, as shown in Figure 5.2. In the case of

organs, failure can be assessed visually on the surface, and µCT is used to assess for internal ice or cracking. Vitrified material is more radiodense (higher Hounsfield Units, HU) on µCT than ice, and cracks can be detected directly by abrupt changes in radiodensity [15, 18] (see Figure S5.13).

Modeling the cooling and warming of the (0.5, 1, and 2.5 L) cryobag systems was performed by heat transfer simulation. Convection occurred as a boundary condition but is neglected within the specimen due to the high viscosity of CPAs in subzero temperatures (below their melting temperature $T_m$) and glassy phase (solid behavior) at cryogenic temperatures. Therefore, the general form of the governing equation for cooling and warming is the conduction heat equation:

$$\rho C_P \frac{\partial T}{\partial t} = \nabla \cdot (k\nabla T) + q_v''' \qquad (5.1)$$

Where r is density, $C_p$ is specific heat, q''' is volumetric heating (generated from IONP = $SAR_V$), etc.

Finite element modeling of Eqn. 5.1 was used to guide modeling for the development of a successful cooling protocol. First, the cryobag geometry is assumed to be filled with CPA with the thermal properties of M22, which has been used for both CPA and CPA-loaded organs, as shown in Table S5.2 [37]. Cooling was predicted from 0 °C with the same initial condition and boundary cooling at ~-40°C/min (maximum CRF cooling rate). Two important modeling outcomes are the cooling rate between $T_m$ and $T_g$ to avoid ice formation and the thermal gradient in the glassy region (below $T_g$) to avoid fracture/cracking failure. Upon reaching a temperature of -122°C, just above $T_g$, the system is annealed (held at constant temperature) to achieve thermal equilibration, as shown in Figure S5.4. Note that larger volumes and $L_C$ (V/SA) result in different thermal histories and longer annealing time, as shown in Table 5.2. After annealing, the system is cooled slowly (<1 °C/min) down to -150°C for storage to avoid thermal stress cracks by keeping temperature differences (< 20 °C gradient) in the brittle glassy phase [38]. The system is then stored at -150°C until rewarming. Temperature distribution across cryobag geometry is plotted in Figure S5.12 for the three CPA volumes. Measured CR in region of ice formation drops with increased volumes from ~1.4°C/min for 0.5L ($L_C$~1.2cm), to ~1°C/min for a 1L ($L_C$~1.4cm), and finally ~0.5°C/min for 3L ($L_C$~2.2cm) cryobag.

Table 5.2: Summary of cooling protocols and achieved cooling rate for each vitrification volume.

| **CRF Cooling Protocol** | **0.5 L** | **1 L** | **3 L** |
|---|---|---|---|
| Characteristics Length: $L_C$ | 1.2 cm | 1.4 cm | 2.2 cm |
| Start Temp. | 20°C | 20°C | 20°C |
| Cool to -122°C | -40°C/min | -40°C/min | -40°C/min |
| Anneal (hold) at to -122°C | 180 min | 250 min | 520 min |
| Cool to -150°C | -0.5°C/min | -0.4°C/min | -0.2°C/min |
| Hold at -150°C | 35 min | 50 min | 90 min |
| Total Protocol Time (hrs) | 4.6 | 6.2 | 12.5 |
| Modeled Center Cooling Rate (0 to -100°C) | 1.36 | 0.96 | 0.45 |

Liter-scale vitrification of CPAs

Using these developed cooling protocols (also plotted in Figure 5.3C) for different volumes, we then cooled the cryobags with CPAs (M22, VS55, 40%EG+0.6Msucrose) inside CRF at the three modeled volumes (0.5, 1 and 3L). As shown in Figure 5.2, successful vitrification in M22 is achieved for all the test volumes (0.5, 1 and upto 3L). 40%EG+0.6Msucrose also successfully vitrified with no visual ice formation upto 1L (see supplementary Figure S5.10 for photos). Further, ice formation failure is observed in VS55 due to achieved cooling rates being near or lower than its CCR for all the 3 volumes (Figure S5.10). This would be most likely due to the achieved cooling rate at the three volumes (0.5L~ 1.4°C/min, 1L~1°C/min, 3L~0.5°C/min) being very close or slightly lower than its CCR (~2.5°C/min). Using µCT scans we further confirmed our visual findings of successful vitrification in M22, 40%EG+0.6Msucrose and ice formation in VS55 as shown in Figure S5.9 (for 0.5L volumes). Temperature profile measured using a jig is shown in Figure 5.3B (See Figure S5.12 for actual jig photos). The cooling rates achieved are shown in Figure 5.3D, and temperature gradients are shown in Figure 5.3E. As before, the cooling rates drop, and gradients increase with increasing sample volume. Note that the edges cool considerably faster than the center of a cryobag. For instance, the thermal diffusivity of M22 is ~ 8 x $10^{-8}$ $m^2/s$,

suggesting the equilibration time of a 3L volume ($L_C$ = 2.2 cm) to be ~8.4 hrs, which closely matches the annealing times predicted from modeling (Table 5.2).

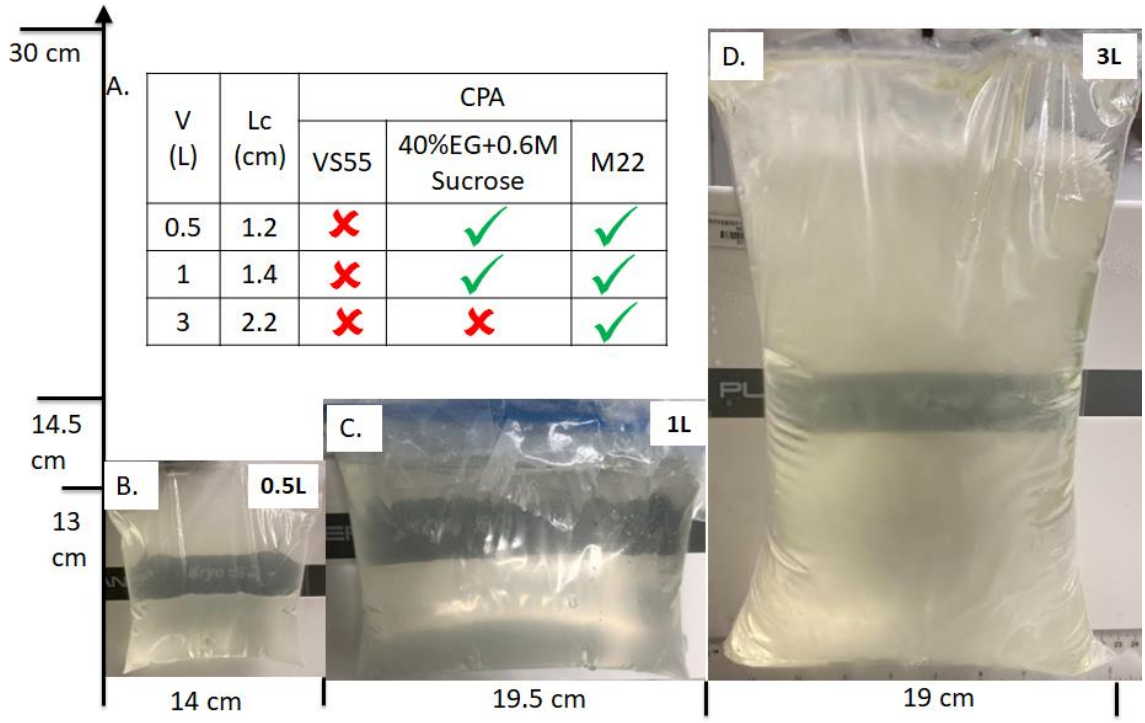


| V (L) | Lc (cm) | CPA | | |
|---|---|---|---|---|
| | | VS55 | 40%EG+0.6M Sucrose | M22 |
| 0.5 | 1.2 | ✗ | ✓ | ✓ |
| 1 | 1.4 | ✗ | ✓ | ✓ |
| 3 | 2.2 | ✗ | ✗ | ✓ |

Figure 5.2: Demonstration of physical success of vitrification in multiple volumes. A. Inset Table summarizes vitrification results for all the 3 CPAs and volumes. Photo of a successful vitrified (glass) M22 inside a cryobag for B. 0.5 Liter, C. 1 Liter, and D. 3 Liter (largest volume reported). The out of plane thicknesses are 5.5, 6.5 and 10.5 cms for 0.5, 1, 3L cryobags.

To further test our ability to physically vitrify at human organ scales, we perfused and cooled a porcine liver with 40%EG+0.6Msucrose. After perfusion loading, the organ was cooled, as shown for the 1 L cryobag in Figure 5.3. The resulting vitrified porcine liver is shown in Figure 5.4. Note the absence of ice throughout, except a small amount formed inside the portal vein and fatty tissue, which presumably did not equilibrate fully with the CPA. The bulk of the organ was confirmed to be vitrified by visual photos after liver was cut in middle. FEM modeling predicted the center cooling rate of the liver as ~4°C/min, which exceeds the CCR (<~1 °C/min) of the CPA (40%EG+0.6Msucrose), which further supports vitrification (see Figure S5.6). Effective cryobag sealing to avoid any air was beneficial in preventing open-surface ice formation and reducing the size of the system ($L_C$). Complete vacuum sealing leads to ice on superficial surfaces of liver organs because of surface containments therefore a thin layer of CPA was proven to be beneficial for

successful vitrification. Of note, this porcine liver (total volume ~1L= liver ~0.8L + surrounding CPA ~ 0.2L) leads to an $L_C$ of ~1 cm (20x24x2cm), which is smaller than the $L_C$ of an adult human liver (~2 cm) and corresponds closer to a juvenile human liver or human kidney ($L_C$~1.1 cm).

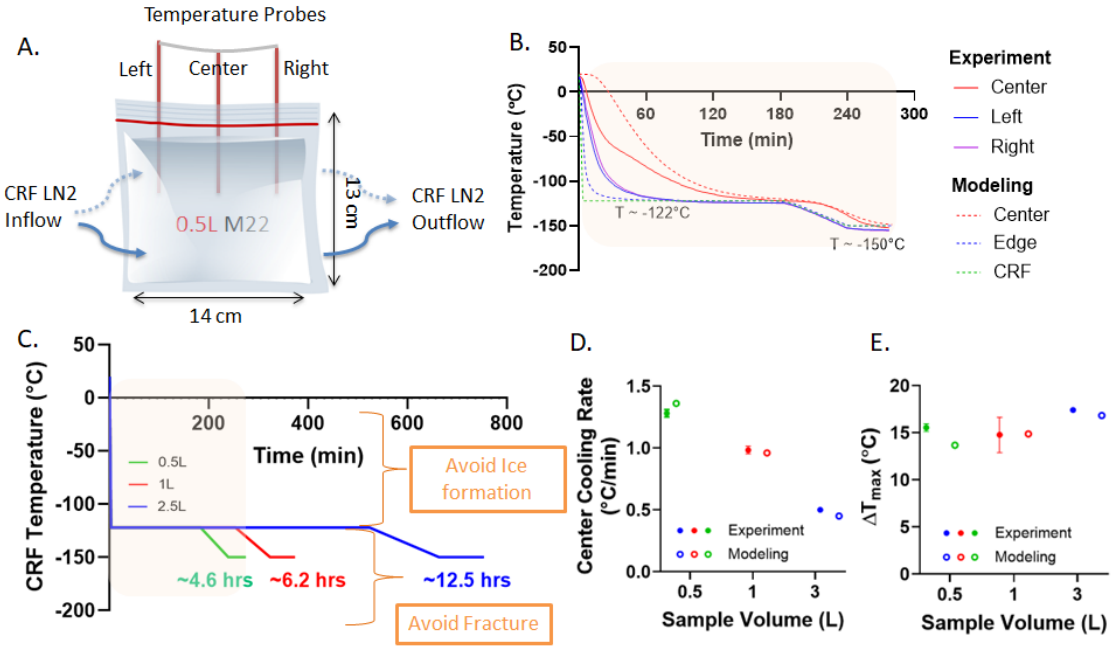


Figure 5.3: Thermal results from experimental and modeled liter scale CPA vitrification. A. Schematic for a representative case, 0.5L cryobag containing CPA with placement of three fiber optic temperature probes. Blue arrows show the direction of LN2 flow in CRF (control rate freezer). B. Experimental and predicted temperature vs. time plot for 0.5L M22. Fiber optic temperature probes were placed 3 cm apart in the center, left, and right edges of the cryobag. The dashed green line shows the programmed CRF temperature profile/protocol. C. CRF cooling protocols for 0.5L, 1L, and 3 L volumes. The region of ice formation and fracture failure is also shown with the orange arrows. (D) Scatter plot of center cooling rate (mean with standard deviation error bars; n=3) and temperature difference ($\Delta T_{max}$ in the glassy region) (mean with standard deviation error bars; n=3) for all three volumes tested for M22. Mean is calculated in ranges 0 to -100C for cooling rate and -120 to -150C for temperature difference plot. Mean cooling rates are greater than the CCR of M22 (dashed line). Temperature differences are within the allowable limit (dashed) (< 20°C) calculated from simple thermal shock equation [22]. Here we demonstrated a good correlation between experimental and modeled cooling rates during vitrification.

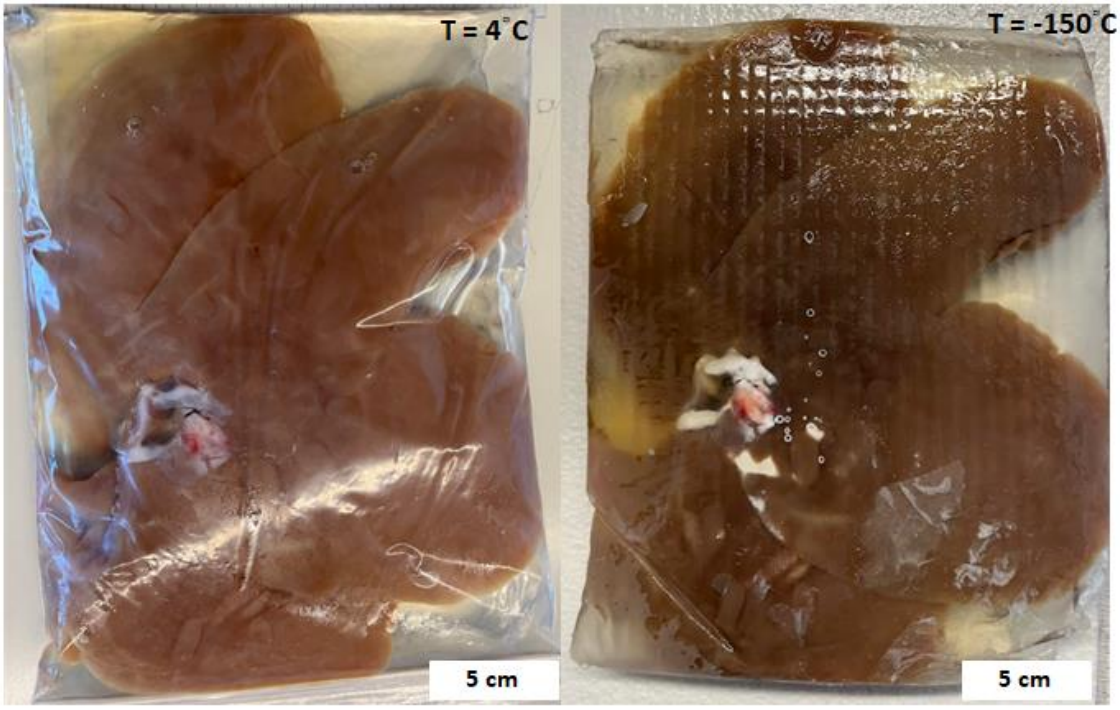


Figure 5.4: Photos of porcine liver (left) before (T = 4°C) and (right) after vitrification (T = -150°C). Pattern on the photo was due to the cryobag placement on a mesh in control rate freezer (CRF) (see Figure S7B). The cryobag was removed for the vitrified liver photo to reduce glare.

Using modeling, we can project center cooling rates for human organs based on their characteristics length ($L_C$) as compiled in Table 5.3. This is not meant to represent a specific organ exactly but rather to allow comparisons. For instance, a small organ such as an ovary can cool at ~15°C/min, whereas the liver can only cool at ~0.6°C/min. These calculations assume the organ is vitrified alone without any surrounding CPA. The addition of CPA would increase $L_C$ and decrease these estimated CRs; hence, our estimate provides a limiting best-case scenario for CRF cooling.

Table 5.3: Center cooling rates for human organs based on characteristic lengths.

| Human Organs | Approximate Volume Adult Female-Male | Dimensions* (cm) | Lc** (cm) | Center/ Minimum Cooling Rate predicted*** (°C/min) |
|---|---|---|---|---|
| Ovary | 4-6 mL [39] | 3, 2.5, 1.5 [40] | 0.35 | 14 |
| Testis | 12-18mL [41, 42] | 4 ,3, 2.5 [43] | 0.50 | 7.6 |

| | | | | |
|---|---|---|---|---|
| Eye | 6-7 mL [44] | 2.4, 2.34, 2.3 [44, 45] | 0.39 | 11.2 |
| Pancreas | 60-80mL [46, 47] | 16, 4, 2 [48] | 0.54 | 6.7 |
| Kidney | 150-200 mL [21, 49-51] | 13, 6, 3.5 [52] | 1.1 | 2.2 |
| Heart | 250-350 mL [50, 51] | 12, 8, 6 [53] | 1.3 | 1.6 |
| Lung | 400-600 mL [21, 51, 54] | 22, 8, 14 [55] | 1.9 | 0.9 |
| Brain | 1.3-1.5 L [21, 50, 51, 54] | 18, 13, 12 [56] | 2.2 | 0.7 |
| Liver | 1.5-1.8 L [21, 50, 51, 54] | 21, 15, 10.5 [57, 58] | 2.3 | 0.6 |

*Assuming adult human 64-70kg. There is a variation of ±10% between adult male vs female and right vs. left paired organs.

** Assuming shape as an ellipsoid (comparable volume)

*** Assuming h = 100W/m$^2$K in CRF [22]

Note: For lungs, the specified volume is tissue volume, whereas for $L_C$ calculations, the volume used is total volume, including air space.

Having achieved vitrification, we next evaluate the ability to scalably rewarm liter-scale CPA samples from the cryogenic vitrified state (< -120°C). Although past studies have rewarmed whole rat and rabbit organs using a 15 kW RF Coil system (AMF Life Systems) [15, 18, 20], all studies of nanowarming thus far have been limited to ~100mL (for example, 80mL for 15kW RF Coil of AMF Life Systems [8]. To scale to larger volumes, we will characterize and use a newly custom-built 120 kW RF coil (AMF Life Systems), which has a 2.5L coil capacity and larger uniform field region compared to previous RF coils, i.e., 1 kW and 15 kW systems as shown in Figure 5.5.

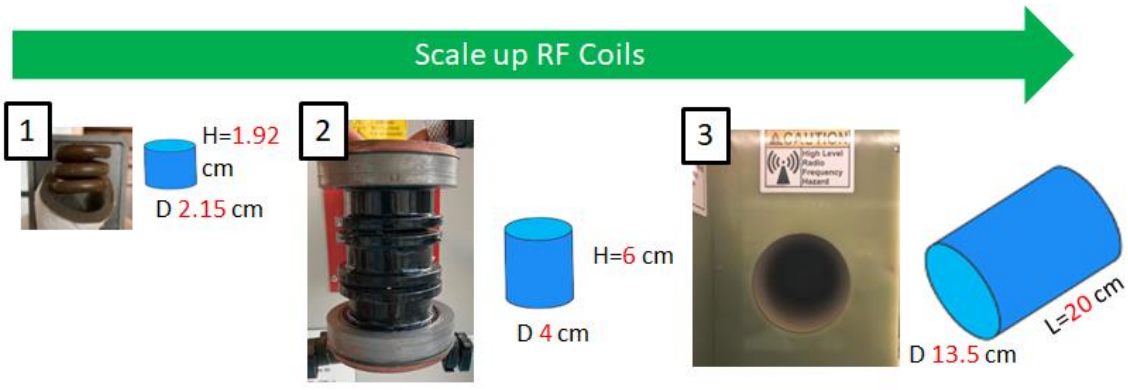


| Coil | Volume (L) | Magnetic Field (kA/m) | Frequency (kHz) | Power (kW) | (+-) % Field variation* |
|---|---|---|---|---|---|
| 1 | 0.001 | 43/35 | 180/360 | 1 | ~30 |
| 2 | 0.08 | 60/35 | 180/360 | 15 | ~6 |
| 3 | 2.5 | 35 | 360 | 120 | ~5 |

*Uniformity is given as % variation in magnetic field strength within the shown dimensions of cylindrical volume

Figure 5.5: Scale-up comparison of 1, 15, and 120 kW RF coil systems for nanowarming. A photo of the RF coil system is shown alongside the schematic of the coil's uniform volume (blue cylindrical region) with a diameter (D) and length (L) listed next to black arrows. The bottom Table compares operating power, magnetic field strength, frequency, sample volume, and uniformity. Note that the RF coil uniformity is a % variation of magnetic field strength across the RF coil volume (blue cylinders).

To ensure the ability to provide uniformity of field, we characterize the 120 kW coil here and point to prior studies to characterize the smaller coils [8, 35] (see Figure S5.15-17). We measured the magnetic field using a 2D RF probe in the 120 kW RF coil as a function of space and coil power. At full power, the RF coil generates up to 35 kA/m magnetic field strengths. This can be visualized as a linear relation between Power and Field strength, as plotted in Figure 5.6C. The magnetic field is spatially uniform (within 5% variation) for 20 cm axial distance and 6cm radial direction, as shown in Figure 5.6D. Note that the higher power of the 120 kW RF coil is a design compromise in that it allows a uniform magnetic field over the large 2.5 L volume and, hence, does not translate into a higher magnetic field intensity than the smaller coils.

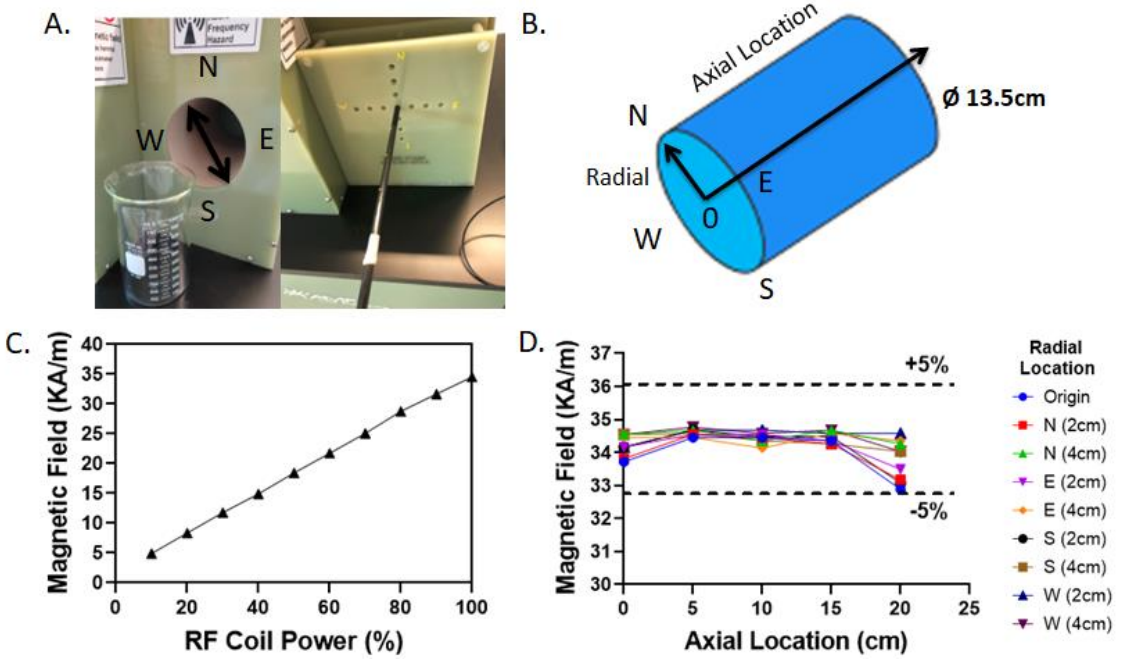


Figure 5.6: Characterization of 120kW radiofrequency (RF) coil for liter scale nanowarming. (A) Photo of the RF coil bore. RF probe placement for magnetic field measurements with labels showing North (N), South (S), East (E), and West (W) radial directions. (B) Schematic diagram of 120kW RF coil sample geometry with marked axial and radial directions. (C) Plot of measured magnetic field strength vs. coil power. (D) Plot of axial magnetic field strength vs. axial location for different radial locations. Axial location is varied by moving the probe along the axis of cylindrical sample space from 0 (inner end of coil sample space) to 20 cm (towards outer end of sample space). Radial location is varied by moving the probe radially into different holes of the jig (green rectangle box) spaced at 0, 2, and 4 cm apart.

To characterize the ability of this coil for nanowarming, we measured the specific absorption rate ($SAR_V$) for IONPs (EMG308) in CPA (M22) as a function of magnetic field and frequency at both room and cryogenic temperatures. As seen in Figure 5.7A, SAR increases with magnetic field strengths, though it slowly saturates at higher field strengths, as observed elsewhere [59]. $SAR_V$ increases at higher frequencies (~2 times more at 360 kHz than 180 kHz for 35 kA/m), meaning more heating would be achieved at 360 kHz than 180 kHz at the same field strength. Therefore, increased $SAR_V$ is expected at 360 kHz and 35 kA/m in the 120 kW coil vs. 180 kHz and 60 kA/m in the smaller 15 kW coil. Lastly, we report that $SAR_V$ increases at cryogenic temperature (by ~

1.5 times) compared to room temperature, as shown in Figure 5.7B. Further details of the SAR calculation can be found in the supplementary information.

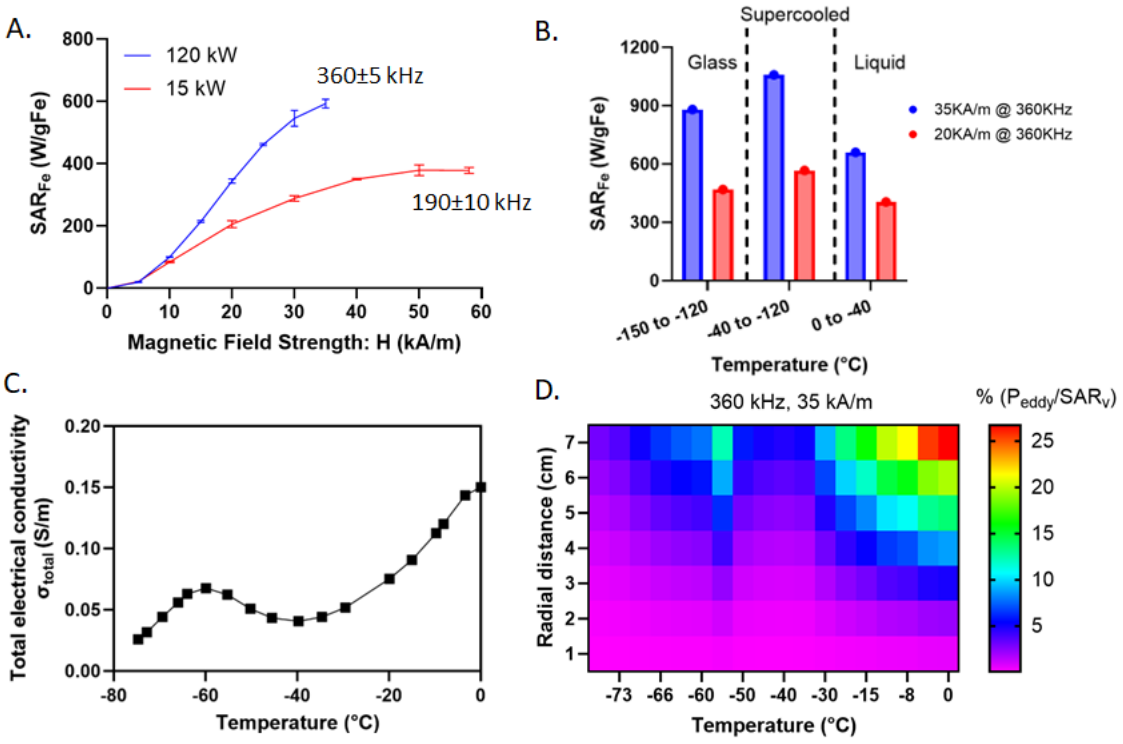


Figure 5.7: Specific absorption rate (SAR) measurements for IONPs. Nanowarming specific absorption rate (SAR) vs Eddy current heating. A. Plot of $SAR_{Fe}$ ($SAR_V$/ $C_{Fe}$) vs. magnetic field strength (H) measured at room temperature for IONPs (EMG308 in water and sIONP in M22) at two frequencies (190 and 360kHz). (B) Plot of $SAR_{Fe}$ vs. temperature for sIONPs in M22. SAR is measured from cryogenic temperature (-196°C) to room temperature (20°C) at two different field strengths (20, 35 kA/m) and 360 kHz. C. Total electrical conductivity variation at low temperature plotted using literature values from [30]. These conductivity values are used for $P_{eddy}$ estimation. D. Heat map plot of $\%P_{eddy}/SAR_V$ with temperature and radial distance (from the center of RF coil) at a fixed magnetic field strength of 35 kA/m and 360 kHz. The red/orange region shows the highest value of $P_{eddy}$, which occurs at larger radius and magnetic field strength and near zero temperatures. This red/orange region needs to be avoided to minimize any unwanted eddy current heating. The purple region shows that eddy heating is insignificant (<2% of $SAR_V$) as seen at lower radius (or field strength) at near zero temperatures and for all radii (or field strengths) at temperatures below <-40°C. For details about the calculations of Peddy, see supplementary, Figure S5.20. $SAR_V$ is calculated assuming 10mgFe/mL IONPs at $SAR_{Fe}$ ~ 1050 W/gFe in the cryogenic -90° to -40°C temperature range and $SAR_{Fe}$ ~ 680 W/gFe in >-30°C temperature range).

One possible source of non-uniformity in larger RF coils is eddy current heating, $P_{eddy}$. Past calculations [8] assuming room temperature electrical conductivity values result in a gross over-prediction of $P_{eddy}$ as both dielectric loss and ionic component contribution decrease drastically in the cryogenic temperature region [60]. Hence, we used dielectric loss and DC electrical conductivity contribution at low temperatures and calculated $P_{eddy}$ as a function of radial distance and magnetic field inside the RF coil as plotted in Figure 5.7D. As evident from Figure 5.7, even though Peddy is ~25% of $SAR_V$ (nanoparticle heating) near room temperature for the maximum radius and field strength in the 120 kW RF coil, it becomes less than 2% of $SAR_V$ at cryogenic temperatures. It can, therefore, be neglected as a source of non-uniform heating during rewarming in the vitrified phase.

To execute nanowarming at scale, we prepared M22 in aqueous solution with EMG-308 at ~10.7 mgFe/mL concentrations for 1L and ~4.6 mgFe/mL for 2L volume (concentration measured using ICP-OES). Further, the $SAR_{Fe}$ of EMG308 in M22 with and without LM5 at 35kA/m, 360kHz tested in 120kW RF coil is very similar (see Figure S5.18). Longer cylindrical form factor cryobags were used to fit in our RF coil, as shown in Figure S5.20. After 1L and 2L volumes were vitrified in the CRF, as noted above, they were rewarmed inside the 120 kW RF coil. These volumes rewarmed to 0°C within ~1min for 1L and ~2min for 2L at rates of ~170°C/min and ~85°C/min respectively (Figure 5.8C). The rate reduction at 2 L is directly attributable to reduced volumetric heating from ~50% lower IONP concentration and resulting SARv reduction of similar value. In all cases, the temperature gradient across the cryobag volume was very small (~<5°C). Warming of similarly prepared IONP CPA solutions at 0.5L and 1L volume were found to be the same and, therefore, independent of size (see Figure S5.21).

As a final proof of principle, we nanowarmed a high concentration of IONP in CPA (100mgFe/mL) in a 1mL cryovial. The CPA is VMP without a carrier solution and is closely related to M22 [61]. The RF coil conditions were 35 kA/m and 360 kHz. We achieved warming at ~1,500°C/min, as shown in Figure S5.21. This is the fastest nanowarming rate reported thus far that we are aware of.

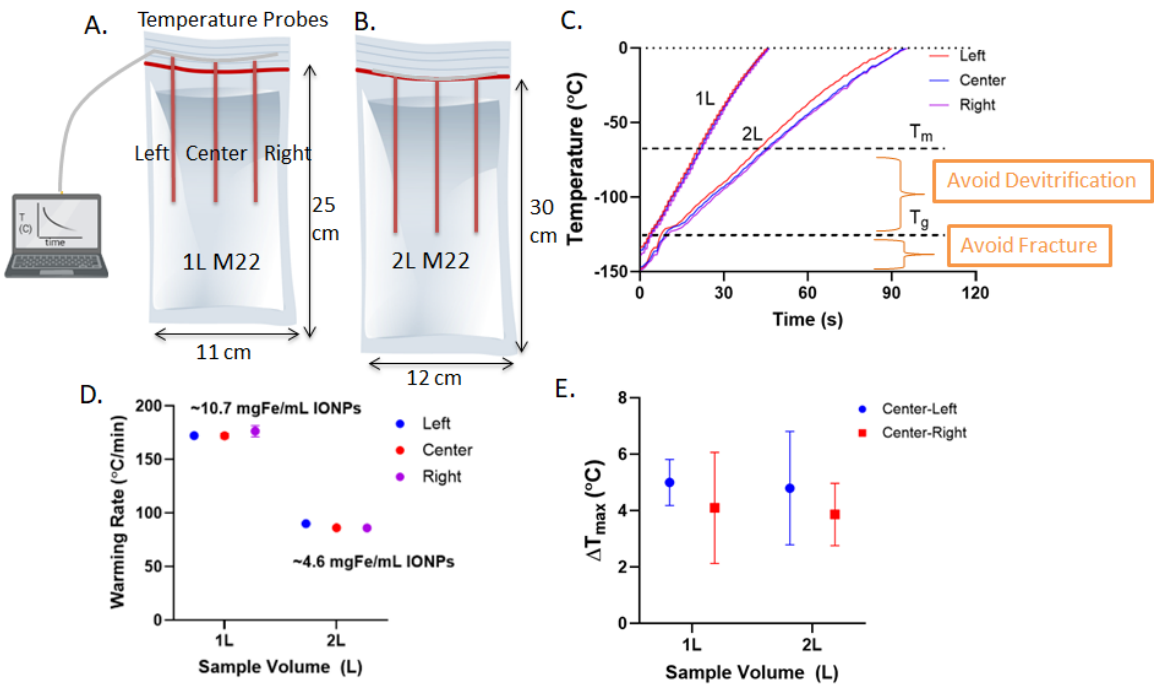


Figure 5.8: Physical demonstration of L-scale nanowarming. A, B. Schematic showing 1L, 2L cryobag containing CPA with three fiber optic temperature probe placements connected to the temperature monitoring system. The dimensions of the cryobag are listed below the black arrows. C. Temperature vs. time plot for 1L and 2L volumes of M22 with varying EMG308 concentrations (10.7mgFe/mL and 4.6mgFe/mL, respectively). Fiber optic temperature probes were placed 4 cm apart in the center, left, and right edges of the cryobag and 13cm inside for 1L and 15 cm inside for 2L cryobag. All three probes heat faster than the CWR of M22 (dashed black line). Scatter plot of D. average rewarming rate and E. temperature difference (ΔT) for 1 L and 2L M22. The average is calculated from 0 to -100°C for the warming rate and -120 to -150°C for the temperature difference plot. Average rewarming rates are greater than the CWR of M22 (~0.4°C/min). Temperature differences (ΔT between center and edges) in the glassy region are negligible (~<5°C).

## Discussion

The challenge of scaling up vitrification to human organ scale systems (Liters) is not only due to the biological complexity of large organs (compared to cells and tissues) but also the physical size itself, which affects the ability to both vitrify and rewarm. Here, we chose CPAs with low CCRs (typically <1°C/min) and yet still having evidence of biological compatibility [61, 62]. Beneficially, CPA-loaded tissues also have lower CCR than the CPA solution alone [63]. However, this benefit is likely reduced as perfused tissues equilibrate to a tissue concentration of only up to

~94-95% of full-strength CPA [16, 31]. A conservative approach would be to select a CPA where the CCR at 95% loading is lower than the achievable cooling rate (e.g., ~1°C/min in CRF for 0.5-1L). While higher concentrations of CPAs such as VS83 (83 w/w% CPA) have even lower CCR and can be more easily vitrified, this comes at the cost of increased biological toxicity relative to the CPAs chosen here [64]. To remain at a lower concentration of CPA and still achieve vitrification at higher volumes without toxicity, future work can assess the impact of ice inhibitors (IRIs), polymers (polyglycerol-PGL, polyvinyl alcohol-PVA, polyethylene glycol-PEG, x-1000, z-1000, etc.), or other cryoprotective agents [65, 66]. Furthermore, convective cooling with liquid cryogens can enhance cooling rates due to larger heat transfer coefficients [67].

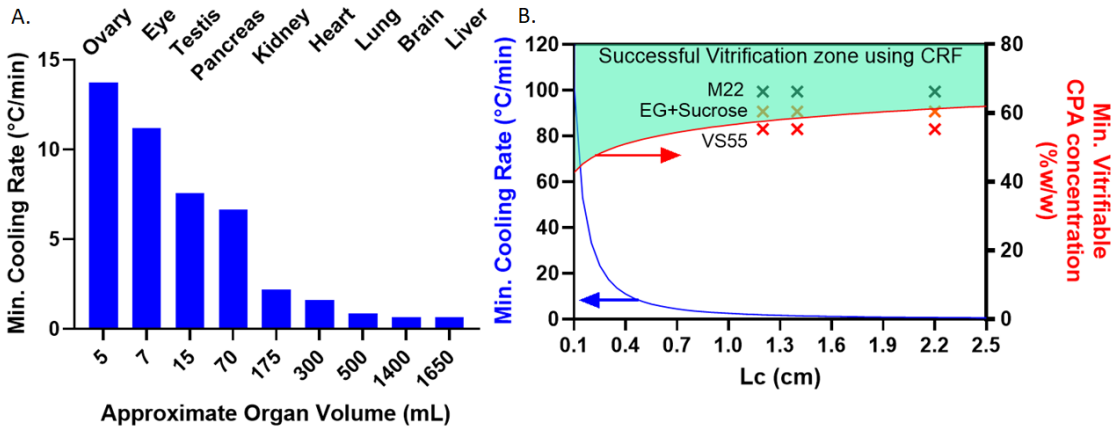


Figure 5.9: Cooling rate and vitrifiable CPA concentration predictions for human organs. A. Predicted minimum cooling rate (CR) as function of A. volume of various human organs. B. Plot of minimum cooling rate vs $L_C$ (blue curve) and minimum vitrifiable CPA concentration in CRF as function of $L_C$ (red curve). $L_C$ is calculated for various organs assuming ellipsoidal shape and minimum cooing rate occurs at center of geometry. Individual data values of $L_C$, CR and dimensions of organs can be found in supplementary Table S5. Note that to predict cooling rates at different volumes, one should calculate $L_C$ and then use blue plot in B. Cross marks in B. represents CPA concentration of M22, VS55 and 40%EG+0.6Msucrose tested experimentally. M22 is the only CPA which showed experimental success achieved at various $L_C$ (~1.2cm – 0.5L, ~1.4cm-1L, ~2.2cm-3L volume) and agrees with this modeled prediction (M22 in green region). See supplementary for calculations of required min. vitrifiable CPA concentration for a given $L_C$.

CPA constituents (polymers, sugars, salts, etc.) can also impact stability in the brittle (i.e., glassy) state. For example, the thermal expansion coefficient of M22 (~2.52 * 10^-4) is greater than VS55 (~1.84 * 10^ -4) [68], which could mean that M22 (which has polymers- that may be more thermally expansive [69]) might be more prone to fractures arising due to thermal stress for the same temperature gradient. To address this, it is crucial to thermally equilibrate samples through annealing, thereby reducing thermal gradients and stress. Without the annealing step, samples can fracture inherently due to larger thermal non-uniformity [15, 20]. After equilibration, the further CR in the glassy region (below $T_g$) must be sufficiently small to avoid thermal non-uniformity (supplementary materials: Computational modeling). Upon reaching the end temperature, a storage solution taking into account cost, durability, and brittleness of the glassy system will be needed. Typically, storage temperatures will be sufficiently below $T_g$ to avoid the danger of devitrification while also avoiding extremely low temperatures that increase whereas storing at temperature far below $T_g$ may induce more brittleness inside the samples. For instance, in one study storage of VS55 for 6 months near $T_g$ enhanced CWR from 50 to ~100°C/min [70]. For long-term storage (days to months) of human organ-scale vitrified samples, physical aging of the glass can also elevate $T_g$, decrease $T_d$ (devitrification temperature), and increase heat release at glass transition during rewarming from the vitrified state [71, 72].

To develop CRF cooling protocols (choosing annealing time, CR in the glassy region, equilibration time at storage, etc.) for volumes other than the ones analyzed in this study, we provide annealing and glassy region CR as a function of $L_C$ as plotted in Figure S5.4. These are designed to be faster than the CCR of the noted CPAs between the melt and glass transitions. Further, the $\Delta T$ within the glassy state is designed to be less than 20 °C to avoid fracture. For larger volumes, the extensive (e.g., ~12 hrs for 3L) cooling protocols highlight the need for innovation, perhaps through a combination of convective and volumetric cooling approaches. Volumetric approaches, in particular, may help address non-uniformity within convectively cooled volumes (such as in CRF).

Fortunately, volumetric rewarming is possible through nanowarming. In fact, we find a higher $SAR_{Fe}$ (specific absorption rate- see supplementary section on $SAR_V$) in the cryogenic regime, likely due to the higher susceptibility and magnetization at such low temperatures and the reduced specific heat of CPAs in the glassy region [73]. SAR of magnetic nanomaterial is a function of the magnetic field, frequency, concentration of magnetic nanomaterial (such as IONPs) and other magnetic properties, as reported in Rosenweig [74]

At low frequencies (f < 2.6 MHz see supplementary section calculations), the SAR increases with the square of the magnetic field (Eq. 5.3) and roughly the first order of frequency. At higher frequencies (f > 2.6 MHz), it is proportional to the square of the magnetic field but becomes independent of frequency. Experimentally, the SAR has been shown to saturate with magnetic field strength, as reported in the literature [59, 75] and shown in Figure 5.7A for our 120 kW, 360 kHz SAR. This means that beyond a maximum threshold field and frequency, there will not be any practical gains in SAR enhancement. This frequency is ~2.6 MHz for EMG308, and field strength appears to be ~60 kA/m as seen experimentally (Figure 5.7A).

As already noted, a potential artifact of nanowarming is eddy current heating, which is proportional to the square of both magnetic field and frequency. Penetration depth (see Eq. in supplemental) of RF waves decreases with increasing frequency as shown in Figure S5.19B. By restricting $P_{eddy}/SAR_V$ to less than 20% and penetration depth > 20 cm, we can calculate the maximum magnetic field and frequency for EMG308 as $H \leq 22$ kA/m and $f \leq 3.3$ MHz (see supplementary material). Note that these values are conservative as $P_{eddy}$ is directly proportional to $\sigma$, which we assume as 0.1 S/m, which will continue to drop at lower temperatures [60, 76].

A theoretical maximum $SAR_V$ for any IONP system can be calculated assuming a maximum packing fraction of IONPs in a CPA solution (for simple cubic packing $\phi$ =0.52), which gives ~2700 mgFe/mL as the max. IONP concentration. Now plugging max H, f criterion, maximum $SAR_V$ comes out to be ~6 x $10^9$ W/$m^3$ and $SAR_{Fe}$ as ~2300 W/gFe as plotted in Figure S18C. This option is purely hypothetical as it is unlikely that IONP can be suspended in CPAs at this concentration, let alone perfused through an organ. Nevertheless, Figure S5.19 shows the theoretical SAR as a function of IONP concentration for the different cases of EMG308, coated EMG308 as sIONP and pIONPs. Notably, a maximum $SAR_V$ has been achieved with pIONPs of ~ 1.2 x $10^7$ W/$m^3$ which was achieved with a maximum IONP concentration of ~60mgFe/mL which is significantly above what is possible for sIONP (which have a thicker silica shell) [77]. Notably, we showed rapid rewarming rates from ~90° to ~180°C/min in Liter CPA volumes using IONPs (~4.6 to 10.7 mg Fe/ml EMG-308). Further enhancement in rates upto ~1500°C/min is shown in principle with a cryovial (1mL) containing ~100mgFe/mL IONPs. Other nanomaterials such as nanowires/nanobars have also shown ultra rapid nanowarming heating rates up to ~1000°C/min in proof of principle cryovial (<1mL) samples (e.g., Cobalt Nickel nanowires in VS55) [78] which could also benefit clinical scale organ nanowarming.

While we have shown that nanowarming provides uniform and scalable heating across a wide range of sizes, the greatest benefits are likely achieved for larger organ systems. Figure 5.10 (and Table 5.4) provides a summary of estimated nanowarming and convective rewarming for a range of clinically relevant organs. While nanowarming provides substantial increases in rates and uniformity of heating of large organs, achievable convective rates may actually be higher (~ 2 times) for small, less vascularized organs (e.g. ovaries and testes) compared to nanowarming rates assuming 10mgFe/mL perfused IONP in their vasculature. However, in these cases lack of uniformity during convective rewarming may still lead to cracking. This suggests the opportunity to improve the rates achievable with nanowarming by external heating by convection, increasing magnetic field & frequency or more tunable IONP CPA loading outside of these less vascularized organs. More details for these calculations for a representative example of a human kidney can be found in the supplementary material. Finally, it should be noted that the predicted nanowarming rate for adult human kidneys is lower than previously reported rates achieved in rat kidneys (40°C/min versus >60°C/min) [16]. In this case, it is anticipated that the rates achieved in the small volume rat kidneys included contributions from ambient warming and a higher IONP concentration in the surrounding CPA than was actually achieved in the rat kidney vascular fraction.

The CPA concentration needed for physical vitrification at 0.5L (relevant for human kidney, heart) is ~ at least 7.8M (40%EG+0.6Msucrose) and increases to 9.4M (M22) at 3L scale (relevant for human liver) as the minimum expected cooling rates are below 1 °C/min (Table 3). To achieve warming rates above the CWR of those CPAs, the amount of IONP loading and SAR should be carefully assessed. For instance, Table 5.4 shows that for a human kidney, IONP concentration of ~10 mgFe/mL will provide a rewarming rate of 40°C/min, which is safely above the CWR of M22. Table 5.4 also shows that vascularized organs such as lungs and eyes will produce significantly higher nanowarming rates ~60°C/min than convection alone.

To achieve human organ vitrification and nanowarming, various logistical factors must be considered, including the containment system, CPA, and IONP type and concentration. Assuming cryobags are used to contain the organ, they will need to fit within the CRF (~21 x 21 cm opening) and RF coil (~13 cm diameter in our case). Verifying the cryogenic compatibility of the bags (i.e., polyimide, Teflon-PTFE or other suitable material) and the ability to vacuum seal to remove air interface as a nucleation site is key [30, 99]. The CPA concentration needed for physical vitrification at 0.5L (relevant for human kidney, heart) is ~ at least 7.8M (40%EG+0.6Msucrose)

and increases to 9.4M (M22) at 3L scale (relevant for human liver) as the centerline cooling rates are below 1 °C/min (Figure 5.9).

Table 5.4: Nanowarming rates for human organs loaded with 10mgFe/mL IONPs.

| Human Organs | Approximate Volume Adult Female-Male | Lc** (cm) | Estimated Vascular fraction (%) | Predicted WR @ 10mgFe/mL perfused conc. (°C/min) | Conv. Warming Rate (°C/min) |
|---|---|---|---|---|---|
| Ovary [79-81] | 4-6 mL | 0.35 | 4-6 | 8.8 | 15 |
| Testis [82-84] | 12-18mL | 0.50 | 2-3 | 4.4 | 8.5 |
| Eye [85, 86] | 6-7 mL | 0.39 | 26-37 | 56 | 12.5 |
| Pancreas [87-89] | 60-80mL | 0.54 | 20-22 | 37 | 7.5 |
| Kidney [21, 90-92] | 150-200 mL | 1.1 | 20-25 | 40 | 2.5 |
| Heart [92-94] | 250-350 mL | 1.3 | 14-20* | 30 | 1.9 |
| Lung [95, 96] | 400-600 mL | 1.9 | 34-36* | 62 | 1.0 |
| Brain [21, 97] | 1.3-1.5 L | 2.2 | 3-8 | 10 | 0.8 |
| Liver [21, 92, 98] | 1.5-1.8 L | 2.3 | 13-28 | 36 | 0.7 |

Note: References in the organ column refer to vascular fraction calculations.

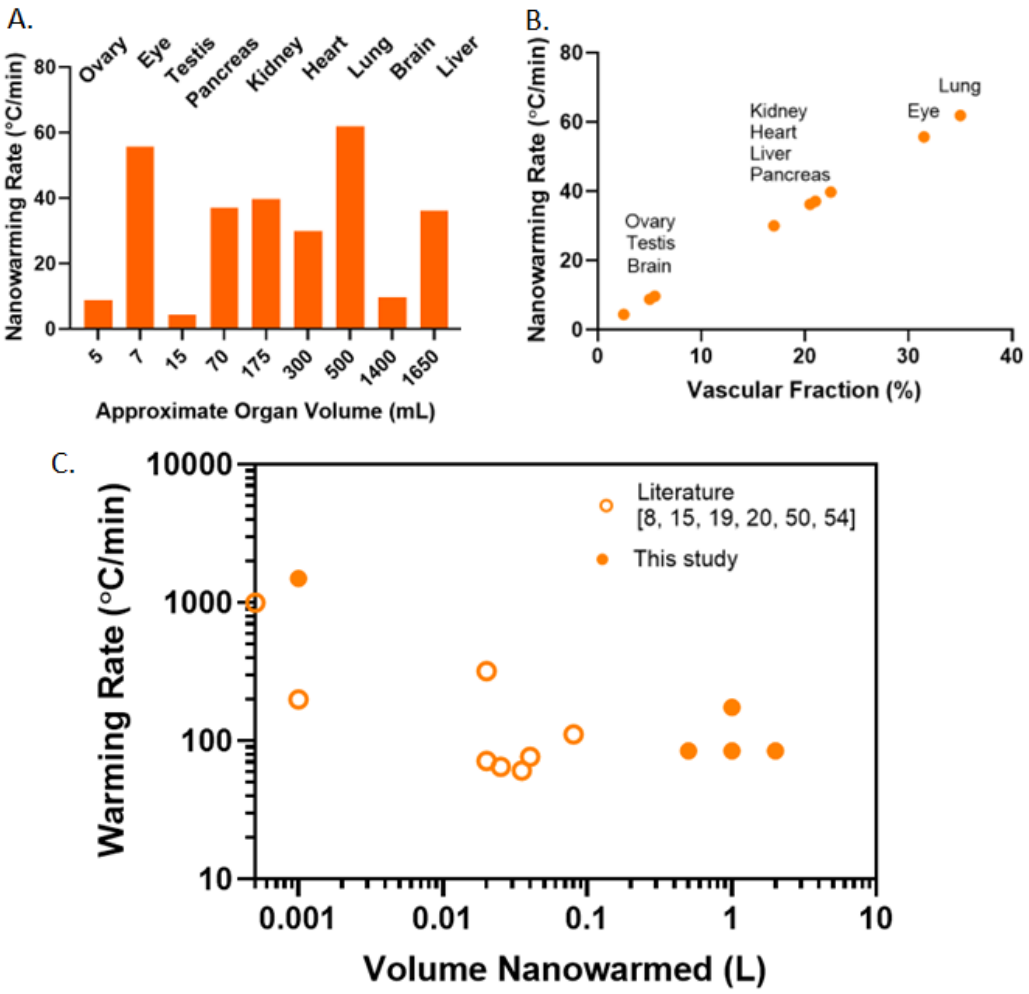


Figure 5.10: Nanowarming rate predictions for human organs. Predicted nanowarming rate vs A. total organ volume and B. vs vascular volume of various organs. Nanowarming rate is estimated for 10mgFe/mL perfused IONP concentration with $SAR_{Fe}$~1050 W/gFe (see supplementary section for calculations and Table 5.4). Nanowarming rate increases with amount of nanoparticle inside vasculature. C. Nanowarming Rates for volumes from mL to L. Open circle represent literature values (refer to Table 1.1 in chapter 1 for references and individual values). This shows that nanowarming is independent of size and scalable to human organs.

Lastly, we can estimate the requirements for IONP for nanowarming a whole human organ. Using a human kidney as an example, the amount of IONP can be estimated as ~ 0.4 gFe = 0.2 (vascular fraction) * 200 (organ volume) * 10 mgFe/mL (perfused IONP concentration). This amount should be multiplied by ~2-4 times the vascular volume to ~0.8 to 1.6 gFe in order to allow perfusion loading [15, 16]. Further, if the surrounding CPA is also loaded with IONP, it will augment the

perfused IONP amount. Thankfully, commercially available IONP (EMG308) can be bio compatibly coated with silica and PEG (i.e., sIONP) and produced at scale with reasonable costs [77].

This study is limited by assumption of CPA will fully equilibrate in tissue as organ can be successfully perfused. Further, this work is limited to physical success, therefore if biological success inside a vitrified and nanowarmed organ can be achieved with the demonstrated physical protocols remain unexplored as the vitrifiable CPA concentrations shown here may exhibit intolerable chemical toxicity to the perfused organ.

# Conclusion

This study demonstrates the ability to successfully vitrify and nanowarm at the scale of human organs, a necessary technology to support the eventuality of human organ banking. We show that by careful thermal engineering, the cooling protocols for a highly stable glass former CPAs (such as M22) implemented in a commercial control rate freezer, vitrification at multi-liter scale (first ever reported vitrification up to 3L volume and a clinical scale liver – porcine liver) can be successfully achieved in a reproducible and stable manner without any ice formation or fractures. Further, we demonstrate that such multi-liter CPA systems can be uniformly and rapidly rewarmed using a state-of-the-art 120 kW RF coil. Finally, our successful outcome of nanowarming up to 2L sample size creates a pathway that can be easily implemented to vitrify a wide range of human-sized organs.

# References for Chapter 5


1. Fahy, G.M., et al., *Vitrification as an approach to cryopreservation.* Cryobiology, 1984. **21**(4): p. 407-26.
2. Giwa, S., et al., *The promise of organ and tissue preservation to transform medicine.* Nature biotechnology, 2017. **35**(6): p. 530-542.
3. Luyet, B.J. and E.L. Hodapp, *Revival of frog's spermatozoa vitrified in liquid air.* Proceedings of the Society for Experimental Biology and Medicine, 1938. **39**(3): p. 433-434.
4. Polge, C., A.U. Smith, and A.S. Parkes, *Revival of spermatozoa after vitrification and dehydration at low temperatures.* Nature, 1949. **164**(4172): p. 666-666.
5. Kilbride, P., et al., *Cryopreservation and re-culture of a 2.3 litre biomass for use in a bioartificial liver device.* PloS one, 2017. **12**(8): p. e0183385.
6. Kilbride, P., et al., *Spatial considerations during cryopreservation of a large volume sample.* Cryobiology, 2016. **73**(1): p. 47-54.
7. Fahy, G.M., J. Saur, and R.J. Williams, *Physical problems with the vitrification of large biological systems.* Cryobiology, 1990. **27**(5): p. 492-510.

8. Manuchehrabadi, N., et al., *Improved tissue cryopreservation using inductive heating of magnetic nanoparticles.* Science translational medicine, 2017. **9**(379): p. eaah4586.
9. Olmo, A., et al., *The use of high-intensity focused ultrasound for the rewarming of cryopreserved biological material.* IEEE Transactions on Ultrasonics, Ferroelectrics, and Frequency Control, 2020. **68**(3): p. 599-607.
10. Izadifar, Z., et al., *An introduction to high intensity focused ultrasound: systematic review on principles, devices, and clinical applications.* Journal of clinical medicine, 2020. **9**(2): p. 460.
11. Xu, R., B.E. Treeby, and E. Martin, *Experiments and simulations demonstrating the rapid ultrasonic rewarming of frozen tissue cryovials.* The Journal of the Acoustical Society of America, 2023. **153**(1): p. 517-528.
12. Ruggera, P.S. and G.M. Fahy, *Rapid and uniform electromagnetic heating of aqueous cryoprotectant solutions from cryogenic temperatures.* Cryobiology, 1990. **27**(5): p. 465-478.
13. Wowk, B., et al., *27 MHz constant field dielectric warming of kidneys cryopreserved by vitrification.* Cryobiology, 2024. **115**: p. 104893.
14. Marsland, T., S. Evans, and D. Pegg, *Dielectric measurements for the design of an electromagnetic rewarming system.* Cryobiology, 1987. **24**(4): p. 311-323.
15. Sharma, A., et al., *Vitrification and Nanowarming of Kidneys.* Advanced Science, 2021. **8**(19): p. 2101691.
16. Han, Z., et al., *Vitrification and nanowarming enable long-term organ cryopreservation and life-sustaining kidney transplantation in a rat model.* Nature Communications, 2023. **14**(1): p. 3407.
17. Zhan, T., et al., *Fe3O4 nanoparticles with carboxylic acid functionality for improving the structural integrity of whole vitrified rat kidneys.* ACS Applied Nano Materials, 2021. **4**(12): p. 13552-13561.
18. Gao, Z., et al., *Vitrification and rewarming of magnetic nanoparticle-loaded rat hearts.* Advanced Materials Technologies, 2022. **7**(3): p. 2100873.
19. Chiu-Lam, A., et al., *Perfusion, cryopreservation, and nanowarming of whole hearts using colloidally stable magnetic cryopreservation agent solutions.* Science advances, 2021. **7**(2): p. eabe3005.
20. Sharma, A., et al., *Cryopreservation of whole rat livers by vitrification and nanowarming.* Annals of Biomedical Engineering, 2023. **51**(3): p. 566-577.
21. Hall, C., E. Lueshen, and A.A. Linninger, *Interspecies scaling in pharmacokinetics: a novel whole-body physiologically based modeling framework to discover drug biodistribution mechanisms in vivo.* Journal of pharmaceutical sciences, 2012. **101**(3): p. 1221-1241.
22. Gangwar, L., et al., *Perspective: A Guide to Successful ml to L Scale Vitrification and Rewarming.* CryoLetters, 2022. **43**(6): p. 303-315.
23. Rabin, Y., et al., *Fracture formation in vitrified thin films of cryoprotectants.* Cryobiology, 2006. **53**(1): p. 75-95.
24. Karimi, S., et al., *Nanowarming improves survival of vitrified ovarian tissue and follicular development in a sheep model.* Heliyon, 2023. **9**(8).
25. Rall, W.F. and G.M. Fahy, *Ice-free cryopreservation of mouse embryos at− 196 C by vitrification.* Nature, 1985. **313**(6003): p. 573-575.
26. Song, Y.C., et al., *Vitreous cryopreservation maintains the function of vascular grafts.* Nature biotechnology, 2000. **18**(3): p. 296-299.
27. Song, Y.C., et al., *Vitreous preservation of articular cartilage grafts.* Journal of Investigative Surgery, 2004. **17**(2): p. 65-70.

28. Courbiere, B., et al., *Cryopreservation of the ovary by vitrification as an alternative to slow-cooling protocols.* Fertility and sterility, 2006. **86**(4): p. 1243-1251.
29. Brockbank, K.G., et al., *Allogeneic heart valve storage above the glass transition at− 80 C.* The Annals of thoracic surgery, 2011. **91**(6): p. 1829-1835.
30. Brockbank, K.G., et al., *Vitrification of heart valve tissues.* Cryopreservation and freeze-drying protocols, 2015: p. 399-421.
31. Fahy, G.M., et al., *Physical and biological aspects of renal vitrification.* Organogenesis, 2009. **5**(3): p. 167-175.
32. Wowk, B., *Thermodynamic aspects of vitrification.* Cryobiology, 2010. **60**(1): p. 11-22.
33. Han, Z., et al., *Diffusion Limited Cryopreservation of Tissue with Radiofrequency Heated Metal Forms.* Advanced healthcare materials, 2020. **9**(19): p. 2000796.
34. Ring, H.L., et al., *The impact of data selection and fitting on SAR estimation for magnetic nanoparticle heating.* International Journal of Hyperthermia, 2020. **37**(3): p. 100-107.
35. Etheridge, M. and J. Bischof, *Optimizing magnetic nanoparticle based thermal therapies within the physical limits of heating.* Annals of biomedical engineering, 2013. **41**: p. 78-88.
36. Jordan, A., M.L. Etheridge, and J.C. Bischof, *-Magnetic Nanoparticles for Cancer Therapy*, in *Physics of Thermal Therapy*. 2016, CRC Press. p. 310-335.
37. Ehrlich, L.E., et al., *Thermal Analyses of a Human Kidney and a Rabbit Kidney During Cryopreservation by Vitrification.* Journal of biomechanical engineering, 2018. **140**(1): p. 0110051-0110058.
38. Steif, P.S., M.C. Palastro, and Y. Rabin, *The effect of temperature gradients on stress development during cryopreservation via vitrification.* Cell preservation technology, 2007. **5**(2): p. 104-115.
39. Pavlik, E., et al., *Ovarian volume related to age.* Gynecologic oncology, 2000. **77**(3): p. 410-412.
40. Giovannopoulou, E., et al., *Ovarian Morphometric and Histologic Characteristics and Correlation with Clinical Factors: A Cross-Sectional Study*. Journal of Personalized Medicine, 2023. **13**(2): p. 232.
41. Ammar, T., P. Sidhu, and C. Wilkins, *Male infertility: the role of imaging in diagnosis and management.* The British journal of radiology, 2012. **85**(special_issue_1): p. S59-S68.
42. Condorelli, R., A.E. Calogero, and S. La Vignera, *Relationship between testicular volume and conventional or nonconventional sperm parameters.* International journal of endocrinology, 2013. **2013**(1): p. 145792.
43. Kim, W., et al., *US–MR imaging correlation in pathologic conditions of the scrotum.* Radiographics, 2007. **27**(5): p. 1239-1253.
44. Silver, D. and A. Csutak, *Human eye dimensions for pressure-volume relations.* Investigative Ophthalmology & Visual Science, 2010. **51**(13): p. 5019-5019.
45. Bekerman, I., P. Gottlieb, and M. Vaiman, *Variations in eyeball diameters of the healthy adults.* Journal of ophthalmology, 2014. **2014**(1): p. 503645.
46. Yoon, J., et al., *Distribution and characteristics of pancreatic volume using computed tomography volumetry.* Healthcare Informatics Research, 2020. **26**(4): p. 321-327.
47. Saisho, Y., et al., *Pancreas volumes in humans from birth to age one hundred taking into account sex, obesity, and presence of type-2 diabetes.* Clinical anatomy, 2007. **20**(8): p. 933-942.
48. Quinlan, R., *Anatomy and embryology of the pancreas.* Shackelford's surgery of the alimentary tract, 1991. **3**: p. 3-18.
49. Cheong, B., et al., *Normal values for renal length and volume as measured by magnetic resonance imaging.* Clinical journal of the American Society of Nephrology, 2007. **2**(1): p. 38-45.

50. Freitas, R.A., *Nanomedicine, volume I: basic capabilities*. Vol. 1. 1999: Landes Bioscience Georgetown, TX.
51. Davies, B. and T. Morris, *Physiological parameters in laboratory animals and humans.* Pharmaceutical research, 1993. **10**(7): p. 1093-1095.
52. Rad, M.P., et al., *Evaluation of Normal Renal Size and its Influencing Factors: A Cross-Sectional Study on the Adult Population of Mashhad.* Caspian Journal of Internal Medicine, 2022. **13**(3): p. 623.
53. Mohammadi, S., et al., *Study of the normal heart size in Northwest part of Iranian population: a cadaveric study.* Journal of cardiovascular and thoracic research, 2016. **8**(3): p. 119.
54. ICRP, P., *Adult reference computational phantoms. ICRP Publication 110.* Ann. ICRP, 2009. **39**(2): p. 1.
55. Sharma, H., K. Prabhakaran, and L. Jain, *Morphometric analysis of human cadaveric lungs.* International Journal of Current Research and Review, 2014. **6**(22): p. 34.
56. Kariotou, F., *Electroencephalography in ellipsoidal geometry.* Journal of Mathematical Analysis and Applications, 2004. **290**(1): p. 324-342.
57. Kennedy, P.A. and G.F. Madding, *Surgical anatomy of the liver.* Surgical Clinics of North America, 1977. **57**(2): p. 233-244.
58. Demir, M., et al., *Ultrasonographic assessment of spleen, kidney and liver size in licensed football players.* Anatomy, 2018. **12**(2): p. 83-89.
59. Bordelon, D.E., et al., *Magnetic nanoparticle heating efficiency reveals magneto-structural differences when characterized with wide ranging and high amplitude alternating magnetic fields.* Journal of Applied Physics, 2011. **109**(12).
60. Robinson, M.P. and D.E. Pegg, *Rapid electromagnetic warming of cells and tissues.* IEEE transactions on biomedical engineering, 1999. **46**(12): p. 1413-1425.
61. Fahy, G.M., et al., *Improved vitrification solutions based on the predictability of vitrification solution toxicity.* Cryobiology, 2004. **48**(1): p. 22-35.
62. Fahy, G.M., et al., *Cryopreservation of organs by vitrification: perspectives and recent advances.* Cryobiology, 2004. **48**(2): p. 157-178.
63. Peyridieu, J., et al., *Critical cooling and warming rates to avoid ice crystallization in small pieces of mammalian organs permeated with cryoprotective agents.* Cryobiology, 1996. **33**(4): p. 436-446.
64. Han, Z., et al., *Model-guided design and optimization of CPA perfusion protocols for whole organ cryopreservation.* Annals of Biomedical Engineering, 2023. **51**(10): p. 2216-2228.
65. Wowk, B., et al., *Vitrification enhancement by synthetic ice blocking agents.* Cryobiology, 2000. **40**(3): p. 228-236.
66. Wowk, B., et al., *Vitrification tendency and stability of DP6-based vitrification solutions for complex tissue cryopreservation.* Cryobiology, 2018. **82**: p. 70-77.
67. Incropera, F.P., et al., *Fundamentals of heat and mass transfer*. Vol. 6. 1996: Wiley New York.
68. Solanki, P.K. and Y. Rabin, *Perspective: Temperature-Dependent Density And Thermal Expansion Of Cryoprotective Agents.* CryoLetters, 2022. **43**(1): p. 1-9.
69. Holliday, L. and J. Robinson, *The thermal expansion of composites based on polymers.* journal of Materials Science, 1973. **8**: p. 301-311.
70. PM, M., *Nucleation and Crystal Growth in a Vitrification Solution Tested for Organ Cryopreservation by Vitrification.* Cryobiology, 1993. **30**(5).
71. Chang, Z.H. and J.G. Baust, *Physical aging of glassy state: DSC study of vitrified glycerol systems.* Cryobiology, 1991. **28**(1): p. 87-95.
72. Struik, L.C.E., *Physical aging in plastics and other glassy materials.* Polymer Engineering & Science, 1977. **17**(3): p. 165-173.

73. Etheridge, M.L., et al., *RF heating of magnetic nanoparticles improves the thawing of cryopreserved biomaterials.* Technology, 2014. **2**(03): p. 229-242.
74. Rosensweig, R.E., *Heating magnetic fluid with alternating magnetic field.* Journal of magnetism and magnetic materials, 2002. **252**: p. 370-374.
75. Sharma, A., et al., *Physical characterization and in vivo organ distribution of coated iron oxide nanoparticles.* Scientific reports, 2018. **8**(1): p. 1-12.
76. Evans, S., *Electromagnetic rewarming: the effect of CPA concentration and radio source frequency on uniformity and efficiency of heating.* Cryobiology, 2000. **40**(2): p. 126-138.
77. Gao, Z., et al., *Preparation of Scalable Silica-Coated Iron Oxide Nanoparticles for Nanowarming.* Advanced Science, 2020. **7**(4): p. 1901624.
78. Shore, D., et al., *Nanowarming using Au-tipped Co 35 Fe 65 ferromagnetic nanowires.* Nanoscale, 2019. **11**(31): p. 14607-14615.
79. Tanaka, N., L. Espey, and H. Okamura, *Increase in ovarian blood volume during ovulation in the gonadotropin-primed immature rat.* Biology of Reproduction, 1989. **40**(4): p. 762-768.
80. Noorafshan, A., et al., *Stereological study of the effects of letrozole and estradiol valerate treatment on the ovary of rats.* Clinical and Experimental Reproductive Medicine, 2013. **40**(3): p. 115.
81. Jokubkiene, L., et al., *Assessment of changes in volume and vascularity of the ovaries during the normal menstrual cycle using three-dimensional power Doppler ultrasound.* Human reproduction, 2006. **21**(10): p. 2661-2668.
82. Turner, T., K. Brown, and C. Spann, *Testicular intravascular volume and microvessel mitotic activity: effect of experimental varicocele.* Journal of andrology, 1993. **14**(3): p. 180-186.
83. Saalu, L., et al., *Moringa oleifera Lamarck (drumstick) leaf extract modulates the evidences of hydroxyurea-induced testicular derangement.* 2011.
84. Gaytan, F., et al., *Morphometric aspects of rat testis development.* Journal of anatomy, 1986. **145**: p. 155.
85. Rust, R., et al., *A revised view on growth and remodeling in the retinal vasculature.* Scientific reports, 2019. **9**(1): p. 3263.
86. Campbell, J., et al., *Detailed vascular anatomy of the human retina by projection-resolved optical coherence tomography angiography. Sci Rep 7: 42201*. 2017.
87. Pisania, A., et al., *Quantitative analysis of cell composition and purity of human pancreatic islet preparations.* Laboratory investigation, 2010. **90**(11): p. 1661-1675.
88. St Clair, J.R., et al., *Contrast-enhanced ultrasound measurement of pancreatic blood flow dynamics predicts type 1 diabetes progression in preclinical models.* Nature communications, 2018. **9**(1): p. 1742.
89. Xie, Q., et al., *Whole-organ CT perfusion of the pancreas: impact of iterative reconstruction on image quality, perfusion parameters and radiation dose in 256-slice CT-preliminary findings.* PloS one, 2013. **8**(11): p. e80468.
90. Chade, A.R., *Renal vascular structure and rarefaction.* Comprehensive Physiology, 2013. **3**(2): p. 817.
91. Garcia-Sanz, A., et al., *Three-dimensional microcomputed tomography of renal vasculature in rats.* Hypertension, 1998. **31**(1): p. 440-444.
92. Šebestík, V., et al., *Red cell, plasma and whole blood volumes in organs of normal and hypersplenic rats.* Blut, 1974. **29**: p. 203-209.
93. Toyota, E., et al., *Dynamic changes in three-dimensional architecture and vascular volume of transmural coronary microvasculature between diastolic-and systolic-arrested rat hearts.* Circulation, 2002. **105**(5): p. 621-626.

94. Wacker, C.M., et al., *Determination of regional blood volume and intra-extracapillary water exchange in human myocardium using Feruglose: first clinical results in patients with coronary artery disease.* Magnetic Resonance in Medicine: An Official Journal of the International Society for Magnetic Resonance in Medicine, 2002. **47**(5): p. 1013-1016.
95. Crapo, R.O., J.D. Crapo, and A.H. Morris, *Lung tissue and capillary blood volumes by rebreathing and morphometric techniques.* Respiration Physiology, 1982. **49**(2): p. 175-186.
96. Nielsen, A.B., et al., *Association between pulmonary vascular volume and cardiac structure and function in patients with atrial fibrillation.* The American Journal of Cardiology, 2023. **205**: p. 182-189.
97. Kaliss, N. and D. Pressman, *Plasma and blood volumes of mouse organs, as determined with radioactive iodoproteins.* Proceedings of the Society for Experimental Biology and Medicine, 1950. **75**(1): p. 16-20.
98. Schwarzbauer, C., J. Syha, and A. Haase, *Quantification of regional blood volumes by rapid T1 mapping.* Magnetic resonance in medicine, 1993. **29**(5): p. 709-712.
99. Huang, H., M.L. Yarmush, and O.B. Usta, *Long-term deep-supercooling of large-volume water and red cell suspensions via surface sealing with immiscible liquids.* Nature communications, 2018. **9**(1): p. 3201.

# Supplementary Information for Chapter 5

## S5.1 Preparation of CPAs and Iron-oxide nanoparticle solutions

The preparation of the CPAs was completed by weight percent (M22, VS55) and volume percent (EG+sucrose) and was completed using a volumetric flask. The preparation of M22 consisted of dissolving PVP (2500kDa) in the liquid reagents and adding 3-Methoxy, 1,2-propanediol last before filling the volumetric flask to volume with Milli-Q (MQ) water. The preparation of VS55 and EG+Sucrose involved dissolving the solid reagents (HEPES and sucrose respectively) in the liquid reagents and adding MQ water to reach full volume.

Silica coated iron oxide nanoparticles (sIONPs) are synthesized within this lab which have been used for organ nanowarming, and CPA stability studies as previously reported by Gao et al [1]. The sIONPs and EMG308 were prepared in CPA (M22, VMP) or water at required concentrations depending upon SAR measurement and nanowarming experiments. Colloidal stability of sIONPs and EMG308 in M22 was monitored over one week. The stability of the solution was determined by using dynamic light scattering to measure the hydrodynamic diameter of the sIONPs in CPA. The sIONPs were stable in M22 for the duration of the week and EMG308 was stable in M22 for one week after LM5 was removed.

## S5.2 ICP-OES quantification of IONP solutions

Total Fe content in solutions of EMG308 in M22 with LM5 removed and sIONPs in M22 were measured using ICP-OES by pipetting 20 µL of each solution into a glass ampule alongside 400 µL HNO3 and 180 µL DI water for a total solution volume of 600 µL. The ampules were flame sealed and the solution was allowed to digest overnight at 90 o C. Solutions were then diluted 10x in DI water prior to total Fe measurement via ICP-OES (University of Minnesota Research Analytical Laboratory, St. Paul, MN).

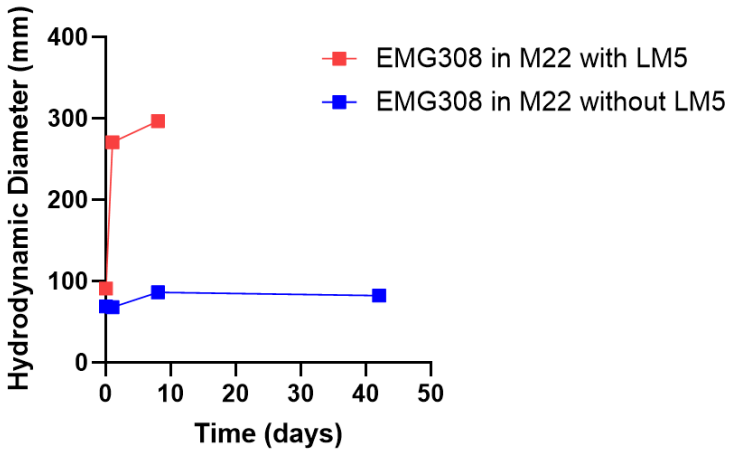


Figure S5.1: Stability of EMG308 in M22 w/o LM5- Plot of Hydrodynamic diameter vs time measured using DLS. Increase in diameter corresponds to aggregation and instability of EMG308s when carrier solution is present (LM5 in M22).

Table S5.1: CPA composition and calorimetric properties

| **CPA** | **Molarity (M)** | | |
|---|---|---|---|
| | **VS55** | **M22** | **EG-Sucrose** |
| Total Concentration<br>(with carrier solution sugars*) | 8.6 M<br>(55.3%w/w) | 9.5 M<br>(66.2%w/w) | 8.0 M<br>(60.4%w/w) |
| Total Concentration<br>(without carrier solution sugars) | 8.4 M<br>(52.6%w/w) | 9.3 M<br>(63.2%w/w) | 7.5 M<br>(57.9%w/w) |
| CCR, CWR (°C/min) | ~2.5, 50 [2] | 0.1, 0.4 [3, 4] | <1, ~45 [5] |
| $T_m$: Melting Temperature (°C) | -38 [6], ~-45 [7] | ~-55 [8] | ~-43 [5] |
| $T_g$: Glass Transition Temperature (°C) | ~-123 [6] | ~-123 [4, 7] | ~-121 [5] |
| **Components** | | | |
| Dimethyl sulfoxide | 3.09 | 2.86 | |
| Ethylene Glycol | | 2.86 | 7.15 |
| Formamide | 3.08 | 2.71 | |
| HEPES | 0.01 | | |

| | | | |
|---|---|---|---|
| N-methyl formamide (NMF) | | 0.51 | |
| Polyvinylpyrrolidone (2,500 kDa) | | 0.01 | |
| Propylene Glycol | 2.21 | | |
| Sucrose | | | 0.60 |
| 3-Methoxy, 1,2-propanediol (MG) | | 0.38 | |
| X-1000 | | 1% w/v | |
| Z-1000 | | 2% w/v | |
| 5x EC carrier solution | 20% v/v | | 20% v/v |
| 5X LM5 carrier solution | | 20% v/v | |

*Note: Carrier solution Euro-Collins (EC) has ~0.2M Glucose and LM5 has 0.09M Glucose, 0.045M Mannitol, 0.045M Lactose.

## S5.3 Computational Modeling of Heat Transfer during vitrification

The governing equation of heat transfer during cryopreservation by vitrification and volumetric heat generation ($q_V'''$) is given as follows, with heat conduction as the primary mode of heat transfer during dielectric warming, microwave warming, and nanowarming.

$$\rho C_P \frac{\partial T}{\partial t} = \nabla \cdot (k \nabla T) + q_v''' \qquad (S5.1)$$

Details of mathematical modeling are given in Figure S5.2. Cryobag with CPA was modeled as a simplified geometry assuming height of geometry same as actual height of CPA (top free surface) in the cryobag. CAD geometry was created in COMSOL 5.4 and later meshing is performed using default setting of extra fine tetrahedral mesh (max. element size ~ 5mm). Dimensions (Width x Height X Thickness) of modeled cryobag for 0.5L volume were 14 x 13 x 5.5 ($L_C$~1.19cm), 1L were 19.5 x 14.5 x 6.5cm ($L_C$~1.42cm) and 3L were 18.5 x 30 x 10.5cm ($L_C$~2.19 cm). Figure S5.3 shows the computational geometry of cryobag with CPA for 0.5, 1 and 2.5L volumes. Temperature is plotted for center of the cryobag geometry (geometrical center) as this is the limiting point where the cooling will be the slowest. Also, temperature the edge of cryobag is also plotted where edge point is assumed to be ~5% inwards from the actual edge (i.e. 95% of half width from center) due

to the fact that actual edge point would be following the same temperature profile as boundary condition (e.g. CRF temperature in cooling) therefore to understand CPA temperature distribution towards the edge of cryobag geometry temperature probe needs to be slightly inside away from the boundary edge (i.e. 5% inwards in our case). Note that the volumetric maximum temperature coincides with the center of geometry and minimum temperature coincides with the actual edge of cryobag. Average center Cooling rate (CR) is estimated by calculating instantaneous dT/dt and taking its average from 0 to -100°C range. For simplicity, thermal properties in modeling are assumed to be of CPA M22 for all the volumes analyzed as listed in Table S2. Note that specific heat for other CPAs such as VS55 is slightly lower (~10%) than M22 at cryogenic temperatures which would imply slightly higher CR than predicted by model in other CPAs such as M22.

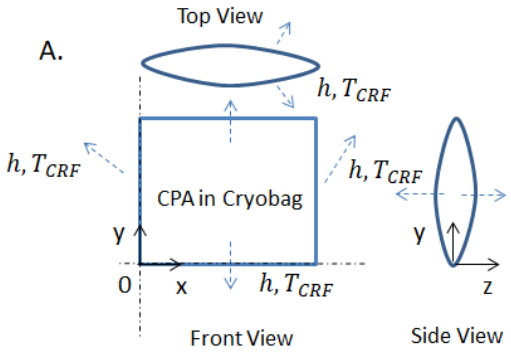


B.

| Case | Convective Cooling in CRF |
|---|---|
| Volumetric Generation | $q_v''' = 0$ |
| Initial Condition | $T = T_{start} = 20$ to 0°C |
| Boundary Condition | $-k\nabla T = h\,(T - T_{cool})$<br>$h = 100 \frac{W}{m^2K}$<br>$T_{CRF} = f(t)$ |

Figure S5.2: Mathematical Model of Heat Transfer. A. Schematic of the geometry and B. Inset table showing details of mathematical model (initial and boundary conditions) for heat transfer FEM during cooling of CPA inside a cryobag.

Temperature difference between center of geometry is kept smaller than the fracture thresholds estimated from simple thermal shock equation as below.

$$\Delta T_{max} = \sigma_{tensile} \frac{(1-\nu)}{gE\beta} \qquad \text{(S5.2)}$$

where g is the geometric coefficient (assumed as 0.5 for cylindrical geometry), ν is poisson's ratio (assumed as 0.2 for typical brittle materials), E is the modulus of elasticity (assumed as 1 GPa for organic materials) and σ is the tensile yield strength of CPA (adapted as 3.2 MPa), based upon prior literature [14]. Worst case $\Delta T_{max}$ threshold can be estimated for M22, by assuming largest coefficient of linear thermal expansion: β (~2.52*10^-4 [1/K]) [15] which comes out to be ~20°C. Now it is interesting to note that actual threshold form thermal shock equation would be further larger as β is function of temperature and would decrease at cryogenic temperatures [15].

Table S5.2: Thermo-physical properties of CPA used for computational FEM modeling

| CPA | Thermal Conductivity: k (W/mK) | Specific Heat: $C_P$ (KJ/kg.K) | Density: ρ (kg/m3) | Coefficient of Thermal Expansion: β *10^-4 (1/ºC) | CCR (ºC/min) | CWR (ºC/min) |
|---|---|---|---|---|---|---|
| M22 | 0.3 [9] | 3.43 (0ºC)<br>3.378 (-18ºC)<br>3.318 (-40ºC)<br>3.180(-76ºC)<br>3.324(-119ºC)<br>1.461(-130ºC)<br>1.318 (-149ºC)<br>[10] | 1100 [11] | 2.52 [12] | 0.1 [3, 4, 13] | 0.4 [3, 4, 13] |

Furthermore, for other CPAs such as VS55 thermal expansion coefficient (β) has been reported slightly smaller (~1.84 * 10^-4) implying $\Delta T_{max}$ threshold would be further higher. Another practically useful way to indirectly estimate a thermal stress threshold for two similar biomaterial such as organs varying in size is based upon simple comparison of $CR*L_C^2$ = constant [16] given in literature (Note: CR is taken to be outer surface cooling rate and $L_C$ is assumed to be effective length scale of outer surface). This allows a simple criterion in choosing the cooling in glassy region for minimizing thermal stresses below a threshold. Therefore, the larger the $L_C$ (size of sample) the slower is the CR in order to keep thermal stresses similar to smaller sample. For 0.5L ($L_C$~1.2cm) CR in glassy region is chosen to 0.5°C/min hence for 1L ($L_C$ ~1.4 cm) estimated CR comes out to be 0.35°C/min and for 3L ($L_C$~2.2 cm) as 0.15°C/min both of which are very close to optimum chosen CR predicted from computational modeling (0.4 and 0.3).

Effect of start temperature on CRF cooling protocol is also analyzed by varying start temperature of cryobag sample and CRF (20, 0, -20°C) which is found to be not significantly large. Now starting from lower temperature would be closer to anneal temperature meaning shorter annealing time though for the start temperature range (20 to -20°C) analyzed, this effect is practically very small (e.g., ~1-3% shorter for 0.5L). On the other hand, it is found that higher start temperature in general would lead to slight increase in avg. cooling rate till anneal temperature because of larger ΔT between sample and CRF which implies larger heat flux (proportional to temperature difference of sample and ambient) and hence slight faster cooling (e.g., ~1.4°C/min at 20°C start temperature vs

~1°C/min at -20°C start temperature for 0.5L). For designing CRF vitrification protocols other than the cryobag volumes tested in this study, we provide cooling protocol parameters as function of Lc which will facilitate successful vitrification for any other shape and volume (see Figure S5.4).

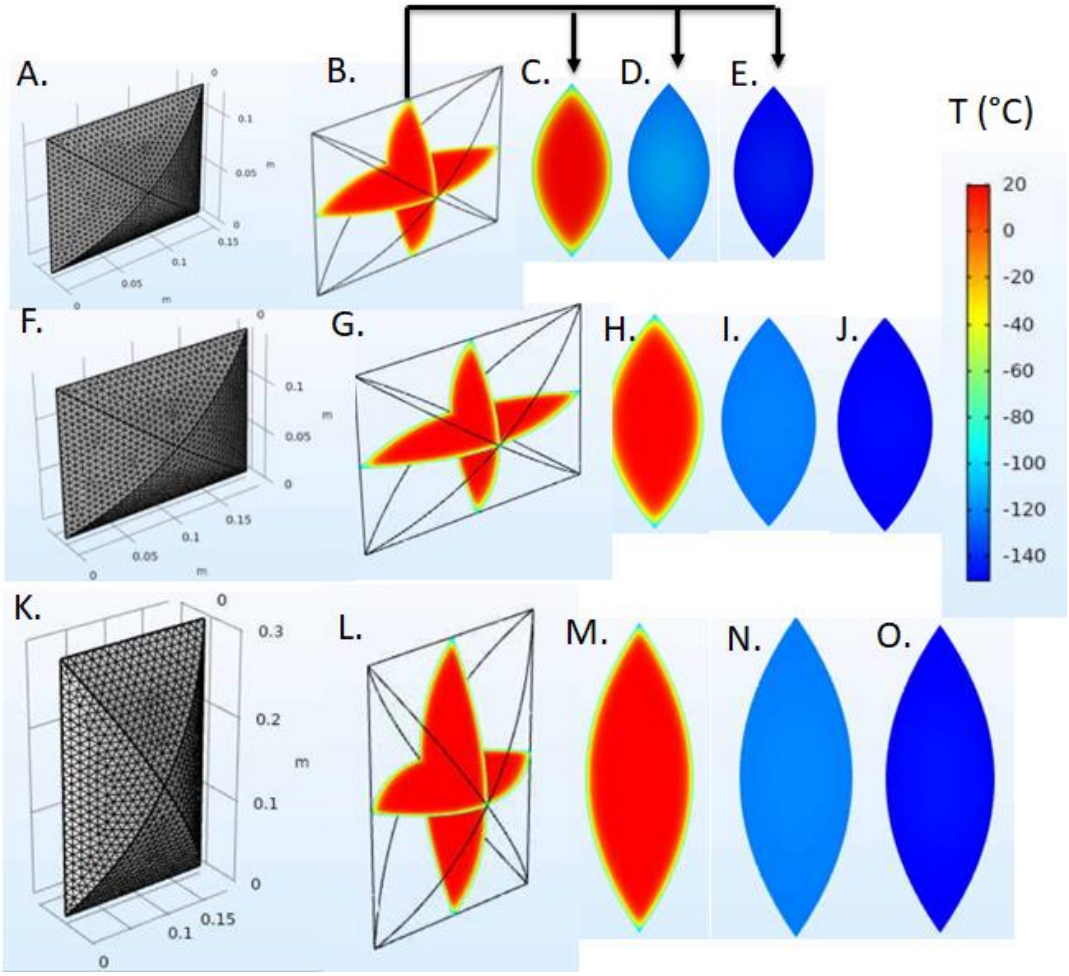


Figure S5.3: Heat Transfer Modeling of CPA inside cryobags. Computational mesh geometry for A. 0.5L, F. 1L, K. 3L volume. Modeled 3D temperature distribution inside cryobag for B. 0.5L, G. 1L and L. 3L volume at a time point of 300 sec (start of annealing step). 2D temperature distribution in one plane of cryobag at the time points at start of annealing C. 0.5L, H. 1L, M. 3L, end of annealing D. 0.5L, I. 1L, N. 3L and end of cooling protocol E. 0.5L, J. 1L, O. 3L volume.

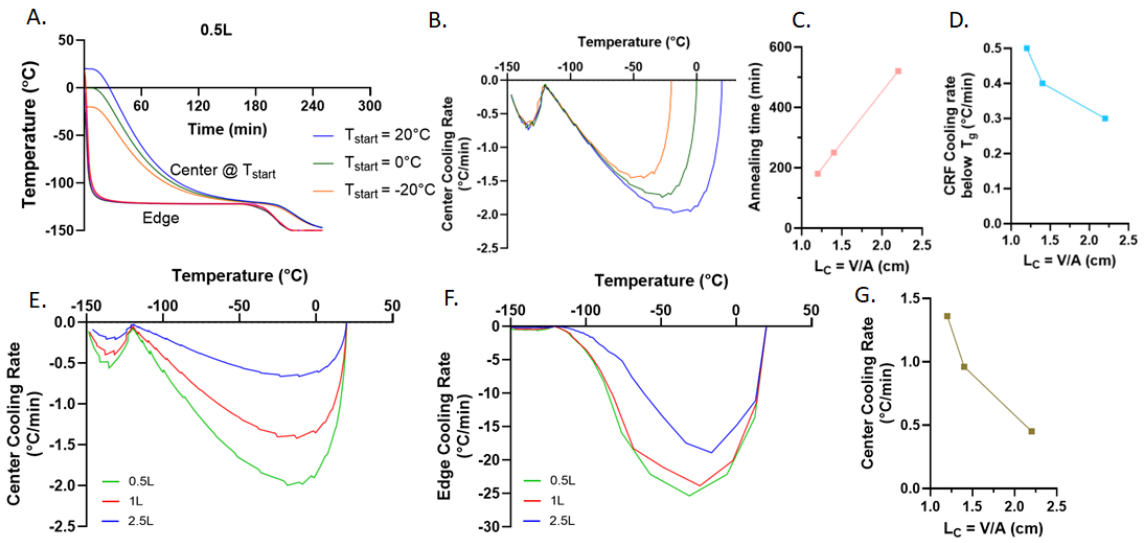


Figure S5.4: Designing CRF cooling protocols based upon $L_C$. A. Temperature vs time for 0.5L CPA (M22) volume with varying start temperature of CRF protocol. B. Effect of start temperature on center cooling rate for 0.5L M22. C. Plot of anneal time as function of $L_C$. D. Plot of CRF cooling rate in glassy region (from $T_{anneal}$ to $T_{storage}$). E. Center and F. Edge cooling rate variation with temperature for 0.5, 1 and 3L CPA (M22) volumes. G. Average center cooling rate (0 to -100°C) as function of $L_C$.

## S5.4 Porcine Liver Perfusion

Constant flow-rate machine perfusion of porcine livers was executed using a perfusion circuit developed in our lab and described in detail earlier [2]. Step loading of CPA was performed starting from carrier solution Euro-Collins (EC) as plotted in Figure S5 below. The chosen flow rate of ~65 mL/min has been based upon literature studies (on hypothermic machine perfusion [17] and supercooling [18]) where similar values have shown to keep perfusion pressure in portal vein within vascular limits for clinical scale livers (<3-4 mmHg). Though, for the purpose of this study we focused upon perfusing CPA for sufficient long to have close to >96% equilibration in tissue to demonstrate physical vitrification success.

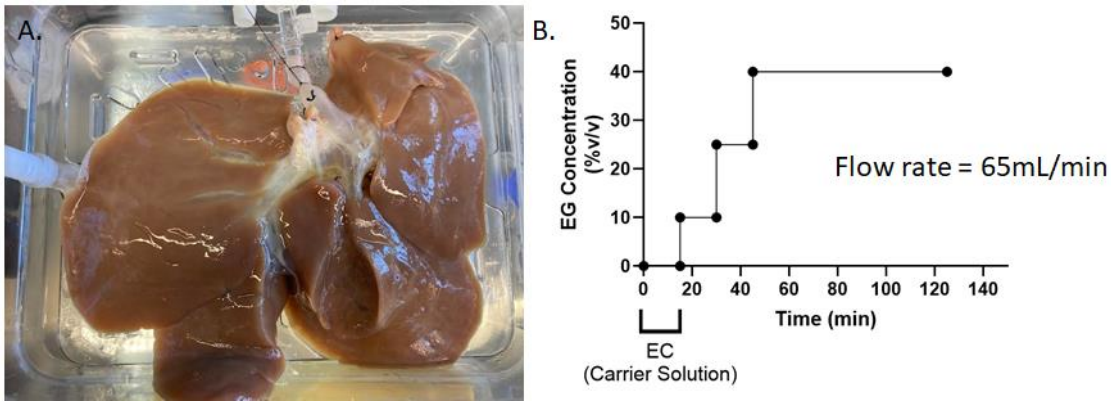


Figure S5.5: Perfusion of porcine liver with 40%EG+0.6MSucrose for physical vitrification: A. Photo of liver after cannulation in portal vein for perfusion. B. Step loading of CPA conc. with time. Note first 15mins correspond to 0%EG meaning 1xEC (Euro Collins-carrier solution) step.

## S5.5 Porcine Liver Heat Transfer Modeling

To further confirm our experimental observation of physical vitrification inside a porcine liver we modeled a 3D geometry based on the actual image of liver converted to 2D sketch and extruded into the thickness of liver geometry (dimensions: width x height x thickness ~ 20 x 30 x 2cm) Figure S5.6A. Total volume ~ 1L and since liver is laid horizontally in CRF where $L_C$ decreases to ~0.83cm allowing execution of 0.5L ($L_C$~1cm) CRF cooling protocol as boundary condition. The temperature within the liver is then solved numerically and shown in Figure S5.6B-E below. The limiting CR within the liver would be at center which is ~4°C/min (averaged over 0 to -100°C) Figure S5.6F which is greater than CCR of 40%EG+0.6MSucrose (<1C/min) confirming no ice formation should occur during cooling. From Figure S5.6E it can be seen the whole liver will cool very uniformly with $\Delta T_{max}$ ~ 3°C minimizing any risk of fracture failure.

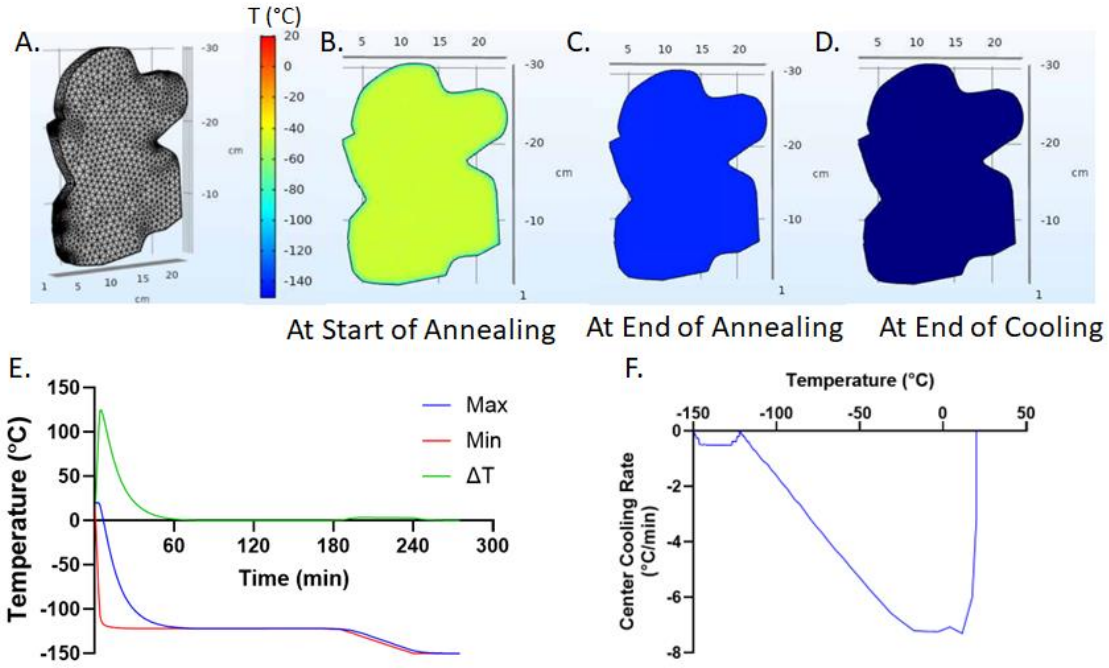


Figure S5.6: Heat Transfer Modeling of porcine liver vitrification in CRF. A. 3D CAD geometry. Temperature distribution across liver B. At start of annealing step (t ~ 5 min), C. at end of annealing step (t ~ 184 min) and D. at end of cooling protocol (t ~ 275 min). E. Temperature vs time plot for liver. Max. and Min represent the maximum and minimum temperature evaluated over the completed domain volume. Note, the center of liver corresponds to maximum temperature. Temperature difference between max and min is also plotted. F. Plot of center cooling rate with temperature (average ~ 4°C/min over 0 to -100°C).

Figure S5.7: Placement of same sample volume i.e. 1L in 3 different orientations inside CRF resulting in three unique characteristics length A. $L_C$ ~ 1.8cm, B. $L_C$ = 1cm, C. $L_C$ ~1.5cm

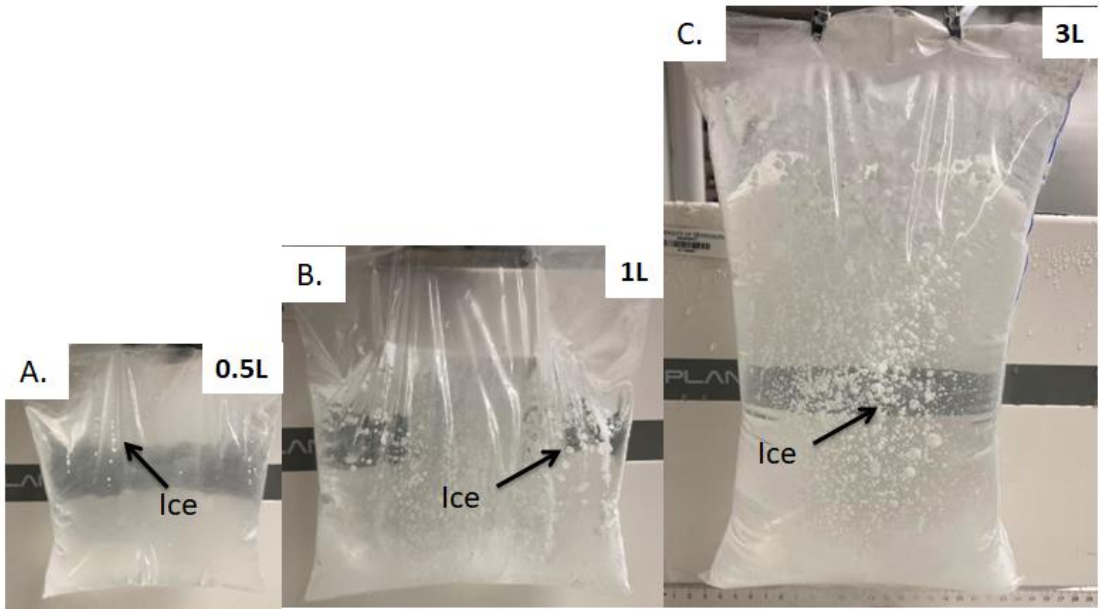


Figure S5.8: Ice formation failure representative photos of CPAs at 0.5L, 1L, 3L (CPA-VS55).

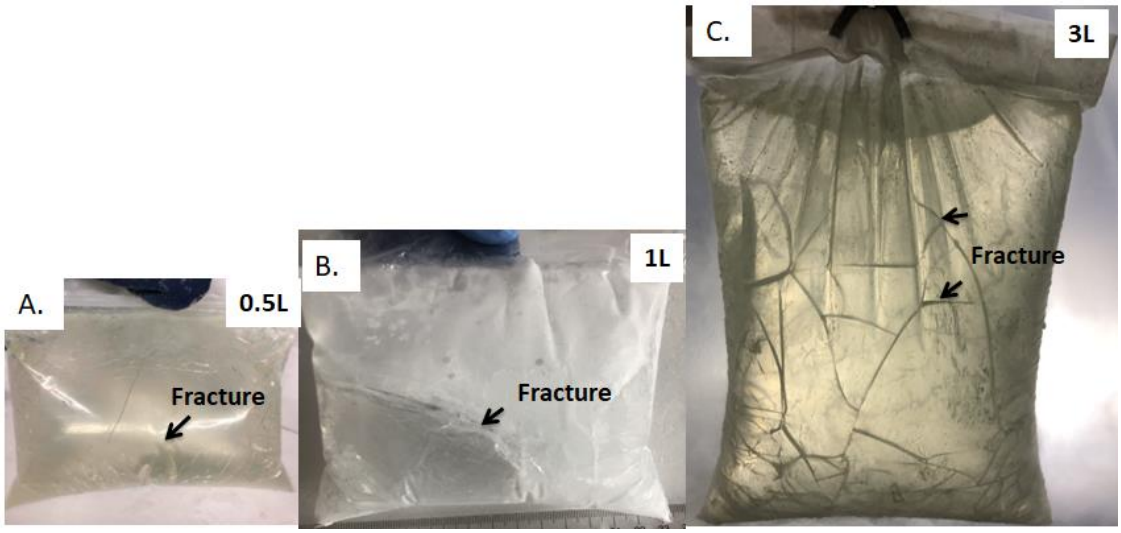


Figure S5.9: Fracture failure representative photos of CPAs at 0.5, 1, and 2.5L scale.

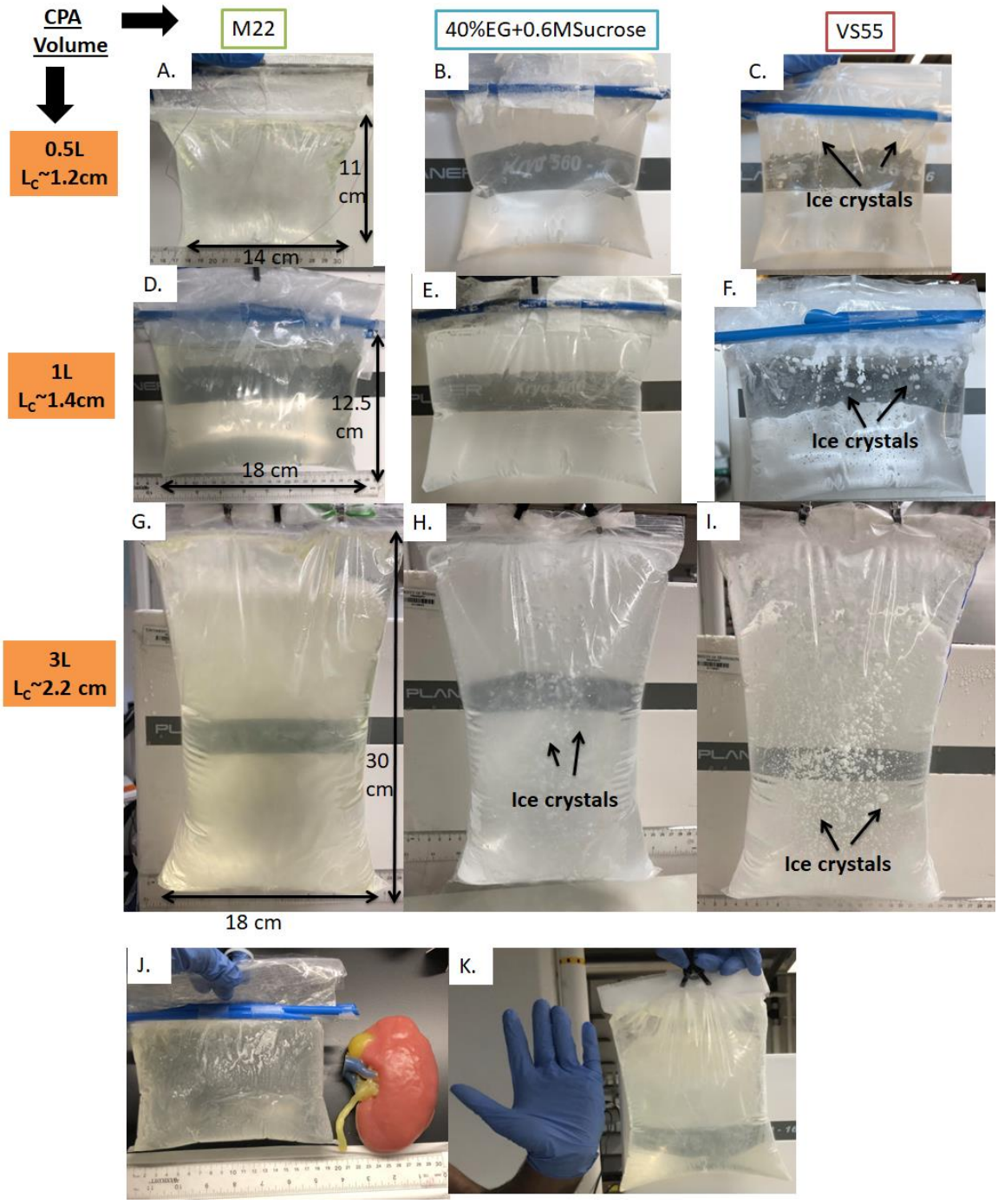


Figure S5.10: Photos after executing CRF cooling protocols for the three CPAs (M22-left, 40%EG+0.6MSucrose-center, VS55-right) tested at A, B & C. 0.5 and D, E, & F. 1L and G, H & I. 3L volumes. VS55 seems to form ice crystals at all 3 volumes due to achieved CR < CCR while 40%EG+0.6MSucrose vitrified successfully without ice formation at 0.5, 1L and M22 vitrified at all 3 volumes up to 3L. Human size comparison of vitrified cryobags (bottommost photos)- J.

human kidney replica next to 0.5L cryobag of M22. K. human hand side by side to the vitrified 3L M22 cryobag.

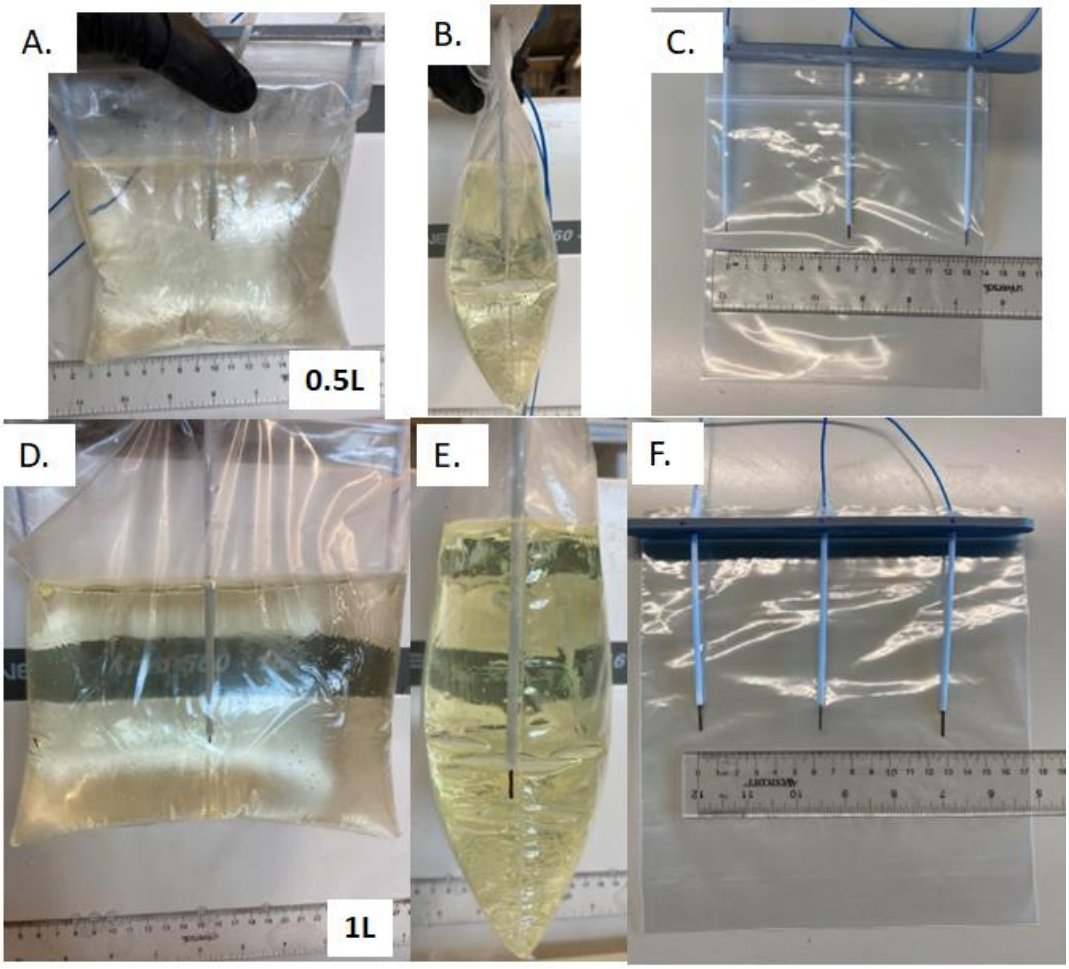


Figure S5.11: 3D printed jigs for fiber optic temperature probe placement in cryobag. A. Front, B. Side view of 0.5L M22 vitrified with probes. C. Probe location in 0.5L cryobag. D. Front, E. Side view of 1L M22 vitrified with probes. F. Probe location in 1L cryobag.

## S5.6 Heat transfer considerations during vitrification in CRF

Characteristics length for heat transfer in a complex shape/geometry is calculated as $L_C = V/A$ where V is total volume and A is total surface area of geometry participating in heat transfer. Cooling rates can be increased for the same volume by reducing the characteristics length $L_C$ for example by reducing thickness of sample inside cryobag which increases the surface area for heat transfer and hence smaller $L_C$. This could be achieved by physically constraining the cryobag using an external mesh. Another way $L_C$ can be decreased is by laying horizontally cryobag on a mesh

platform inside CRF. We achieved this in our case with porcine liver (V~1L) which vitrified at faster cooling rate and shorter annealing time than 1L CPA cryobag since it's $L_C$ was reduced to ~1cm which is similar to a 0.5L CPA volumes in cryobag hanging vertically inside CRF.

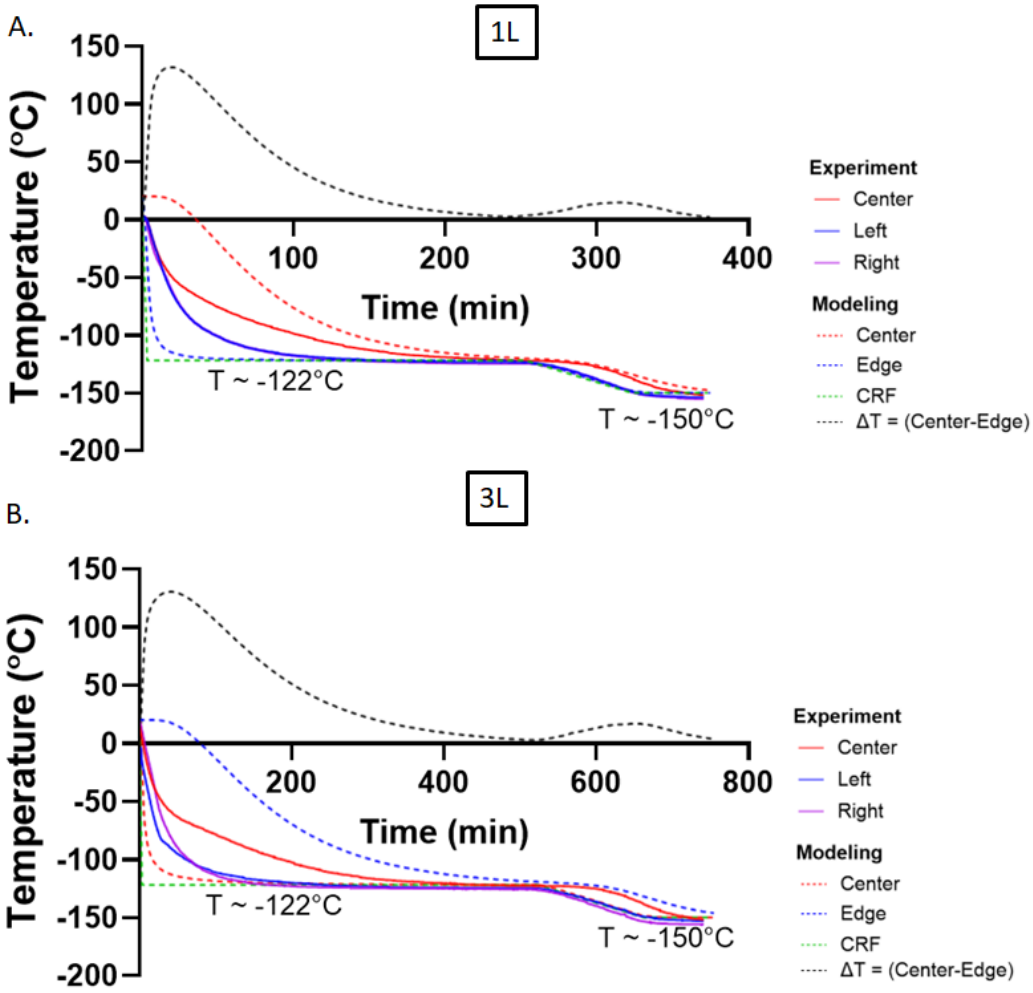


Figure S5.12: Thermometry of liter-scale vitrification. Temperature vs time plot for A. 1L M22, and B. 3L M22. Solid lines represent experimentally measured temperature and dashed lines represent predicted temperature from FEM.

## S5.67 µCT imaging for physical verification of vitrification

Cryobags were imaged using micro-CT scanner NIKON XT H 225 for 500mL volumes. M22, VS55, 40%EG+0.6Msucrose were vitrified in CRF and then transported to microCT lab using a vitrified LN2 based transport container. For NIKON XT H 225 scan of CPAs, the accelerating

voltage was set at 121 kV, and the current was set to 150 µA. We placed a 1-mm aluminum filter between the source and the object to reduce the beam hardening effect [19]. The resolution was 0.098 mm for 0.5L samples. The vitrified CPA samples were held at LN2 vapor temperature (-150°C) in a Styrofoam container during imaging. Two calibration samples, i.e. air and water at room temperature attached to the top of the vitrified CT sample container are used in calculating Hounsfield unit (HU) radiodensity. During the entire scan runtime ~30 min, sample remains in glass state as temperatures are below $T_g$. Artifacts such as beam hardening are addressed during reconstruction to enhance image quality (3D CT pro, Nikon Metrology, MI). Lastly, image post-processing is executed using VGstudio Max 3.2 (Volume Graphics, NC, USA) to convert into unsigned 16-bit float images which are later exported as DICOM images for a final analysis using MATLAB (MathWorks). HU are calculated based upon the following formula:

$$HU = 1000 * \frac{Grey\ scale\ Sample - Grey\ scale\ Water}{Grey\ scale\ Water - Grey\ scale\ Air} \qquad \text{(S5.3)}$$

The edge of the sample shows a smaller signal due to the beam hardening effect, which we attempted to reduce but didn't fully eliminate. This artifact derives its name from its underlying cause: the increase in mean X-ray energy, or "hardening" of the X-ray beam as it passes through the scanned object. Lower-energy X-rays are attenuated more readily than higher-energy X-rays, so a polychromatic beam passing through an object preferentially loses the lower-energy parts of its spectrum.

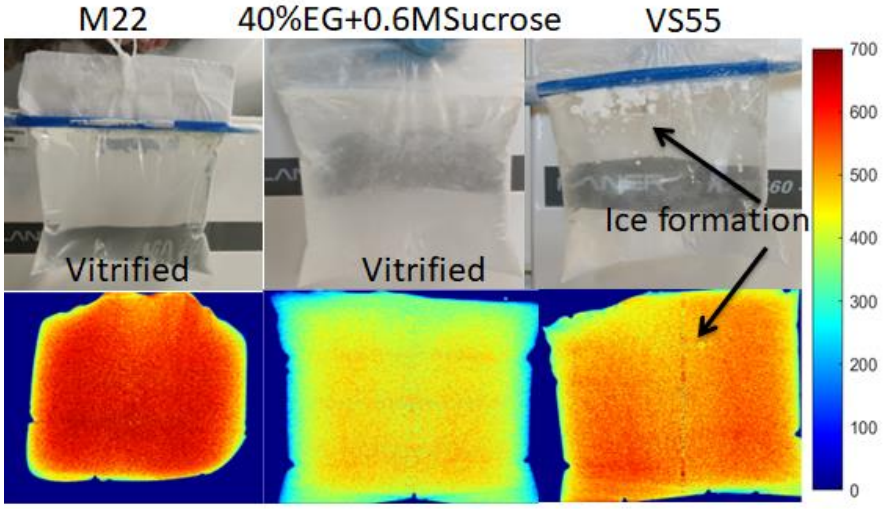


Figure S5.13: µCT images of vitrified CPAs M22, 40%EG+0.6MSucrose and VS55 alongside with Hounsfield units (HU). VS55 shows some ice formation whereas M22, 40%EG+0.6MSucrose shows complete vitrification. Note that difference in HU on the edges of cryobag is due to the edge

effect because of differences in attenuation across edges where physical thickness reduces drastically. Also, the threshold HU for vitrification is slightly different for 40%EG+0.6MSucrose (HU> 400) than M22 and VS55 (Vitrified HU > 500).

Figure S5.14: Photos of center cross section of vitrified liver cut open.

## S5.8 Characteristics length ($L_C$), Cooling Rate and Nanowarming Rate calculation for human organs

1. Here we provide representative calculations of $L_C$ for a human kidney whose Length ~ 11cm, Width~ 7cm, Thickness~ 3.5cm is taken from literature.

Assuming ellipsoidal shape of kidney with semi-axes as half length, half width and half thickness.

$$Volume\ of\ kidney\ (V) = \frac{4\pi}{3} * \frac{length}{2} * \frac{width}{2} * \frac{thickness}{2} \qquad \text{(S5.4)}$$

$$Volume\ of\ kidney\ (V) = \frac{4\pi}{3} * \frac{11}{2} * \frac{7}{2} * \frac{3.5}{2} = 141\ cm^3$$

Using Knud Thomsen's approximation for surface area of ellipsoid:

$$Surface\ Area\ of\ kidney\ (A) \approx 4\pi * \left[\frac{\left(\frac{length}{2} * \frac{width}{2}\right)^{1.6} + \left(\frac{width}{2} * \frac{thickness}{2}\right)^{1.6} + \left(\frac{thickness}{2} * \frac{length}{2}\right)^{1.6}}{3}\right]^{\frac{1}{1.6}}$$

(S5.5)

$$Surface\ Area\ of\ kidney\ (A) \approx\ 4\pi * \left[\frac{\left(\frac{11}{2} * \frac{7}{2}\right)^{1.6} + \left(\frac{7}{2} * \frac{3.5}{2}\right)^{1.6} + \left(\frac{3.5}{2} * \frac{11}{2}\right)^{1.6}}{3}\right]^{\frac{1}{1.6}}$$

$$= 156.2\ cm^3$$

Now, characteristics length for heat transfer becomes:

$$L_C = \frac{V}{A} = \frac{141}{156.2} = 0.9\ cm$$

2. Center cooling rate can be calculated using modeled CR vs $L_C$ parametric fit from literature [20].

$$\log\left(\frac{CR}{CCR}\right)\left[\frac{^\circ C}{min}\right] = a + b * \log(L_C\ [cm]) \qquad \text{(S5.6)}$$

where a is 1.399 and b is -1.609 for M22 and plugging value of $L_C$ of human kidney as 1.1 cm.

$$CR = 0.4 * [1.399 - 1.609 * \log(1.1)]$$

$$CR = 2.15\ \frac{^\circ C}{min}$$

3. Lastly, we estimate nanowarming rate in human kidney at 10mgFe/mL IONP concentration perfused in vasculature as follows:

$$\rho C_P \frac{\partial T}{\partial t} = SAR_V \qquad \text{(S5.7)}$$

$$\text{plugging } SAR_V = SAR_{Fe} * C_{Fe}$$

$$Nanowarming\ rate = \frac{\partial T}{\partial t} = \frac{SAR_{Fe} * C_{Fe}}{\rho C_P}$$

$$Nanowarming\ rate = \frac{1080\ \left[\frac{W}{gFe}\right] * 10\ \left[\frac{mgFe}{mL}\right]}{1100\ \left[\frac{kg}{m3}\right] *\ 3300\left[\frac{J}{kg}.K\right]}$$

$$Nanowarming\ rate \sim 40\ \frac{^\circ C}{min}$$

## S5.9 RF Coils (1, 15, 120 kW) Characterization and Modeling

Electromagnetic models for both systems were performed using Flux2D software (Altair) assuming rotational symmetry, frequency domain and a voltage source. For the 15 kW (80 mL) coil, this approach has proven to be accurate for this style of coil by physical mapping [21, 22]. For the 120 kW (2.5 L) coil, this approach has also been previously validated [23]. The generated magnetic field variation within the coil volume is plotted in Figure S5.14 with 120 kW coil being the most uniform field in the largest volume of interest (VOI).

A simple linear least square fit (equation 8) to magnetic field strength and coil power (Figure 6) gives a correlation as follows which is practically useful in setting up a desired magnetic field strength for nanowarming experiments.

$$H\left(\frac{kA}{m}\right) = 0.3326\,Power\,(\%) + 1.731 \qquad \text{(S5.8)}$$

Magnetic field strength is calculated from voltage readings from oscilloscope using simple equation below:

$$B_{axial} = \frac{V_{rms}}{s_{axial} * f} \qquad \text{(S5.9)}$$

$$B_{radial} = \frac{V_{rms}}{s_{radial} * f} \qquad \text{(S5.10)}$$

$$B_{total} = \sqrt{{B_{axial}}^2 + {B_{radial}}^2} \qquad \text{(S5.11)}$$

where B is magnetic flux density, $V_{rms}$ is measured voltage in root mean square (RMS), f is frequency in kHz and $s_{axial}$, $s_{radial}$ is sensitivity factor for axial and radial direction engraved on the metal section of RF probe. Magnetic field strength (H) can be found further easily by:

$$H = \frac{B}{\mu_o} \qquad \text{(S5.12)}$$

where $\mu_o$ is vacuum magnetic permeability.

Table S5.3: Capabilities of custom-built state-of-art 120kW RF Coil System.

| | |
|---|---|
| Magnetic Field Strength | **3 - 35 kA/m** |
| Treatment Region Inner Diameter | 13.3 cm |
| Treatment Region Uniform Length | 20 cm |

| | |
|---|---|
| Field Uniformity in Treatment Region | +/- 5% |
| Frequency Range | 360 kHz to 400kHz |

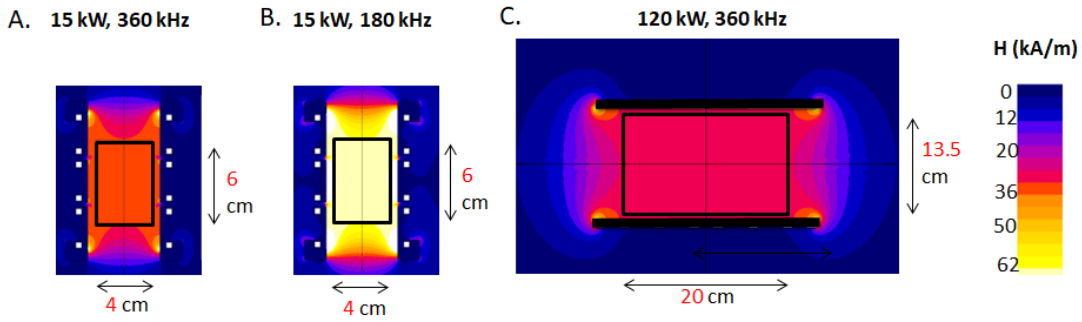


Figure S5.15: 2D FEA simulation of uniformity for A. 15kW coil at peak field and 360 kHz B. 15kW coil at peak field and 180 kHz, C. 120kW coil at peak field and 360 kHz.

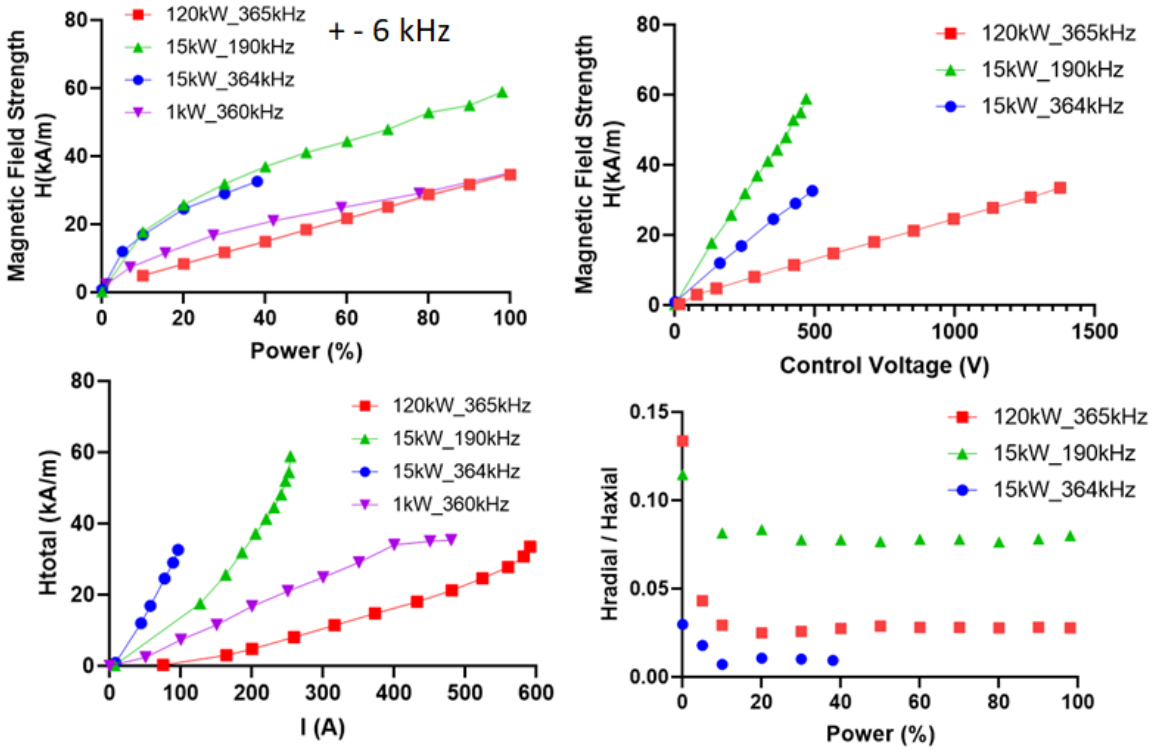


Figure S5.16: Magnetic Field vs A. Coil power, B. Control voltage, C. Coil current comparison for 3 different RF coils 1kW, 15kW and 120kW used for nanowarming. Ratio of radial to axial component of magnetic field strength as function of coil power. The radial component of magnetic field is roughly within 10% of axial field strength regardless of coil power for all the three RF coils.

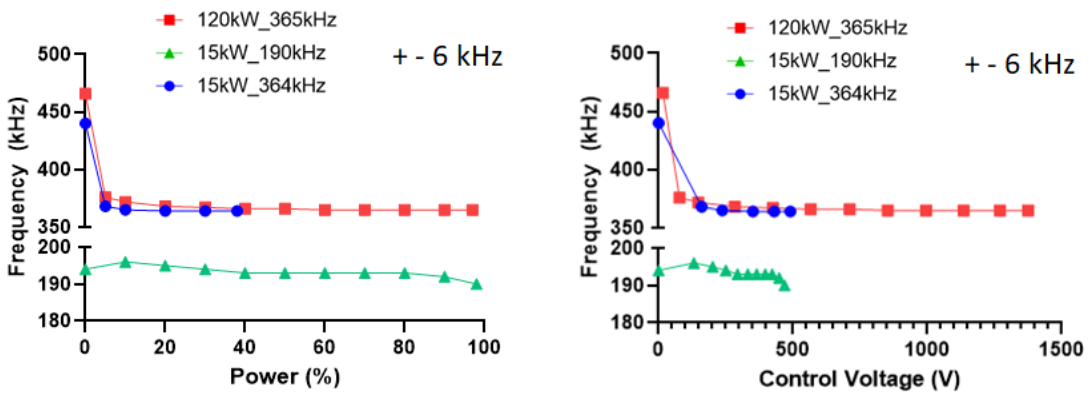


Figure S5.17: RF Coil frequency measured using oscilloscope as function of A. Coil power and B. Control voltage for the three RF coils 1, 15, 120kW systems.

## S5.10 Experimental SAR Measurement

EMG308 IONPs are prepared at ~4mgFe/mL concentrations in M22, H20, VMP. 1mL of IONP solution is taken in a cryovial (Figure S5.18) and heated in RF coil for ~60-180 sec or more depending on the achieved heating rate (slower rate at smaller field strengths are heated for longer duration example ~180 sec at 5 kA/m). Experimental $SAR_V$ is directly calculated by measuring temperature rise produced during heating of IONP samples inside an RF coil. $SAR_V$ can be calculated by applying simple model such as time rise method [36] as follows:

$$SAR_V = \rho C_P \frac{\partial T}{\partial t} \qquad \text{(S5.13)}$$

$$SAR_{Fe} * C_{Fe} = SAR_V \qquad \text{(S5.14)}$$

where ρ is density, $C_{Fe}$ is concentration of IONPs in the sample and $C_p$ is specific heat (at constant pressure) of the sample. SAR can be expressed as heat generation per unit volume in terms as $SAR_V$ ($W/m^3$) or heat generation per unit mass of magnetic nanoparticles (Fe) commonly called as $SAR_{Fe}$ (W/g.Fe) or sometimes called as SLP-specific loss power. It is to be noted that since Cp and ρ varies in cryogenic temperature it is important to incorporate this temperature dependence in SAR calculations.

It was found that the $SAR_{Fe}$ of EMG308 in M22 with and without LM5 at 35kA/m, 360kHz tested in 120kW RF coil is very similar (see Figure S18D).

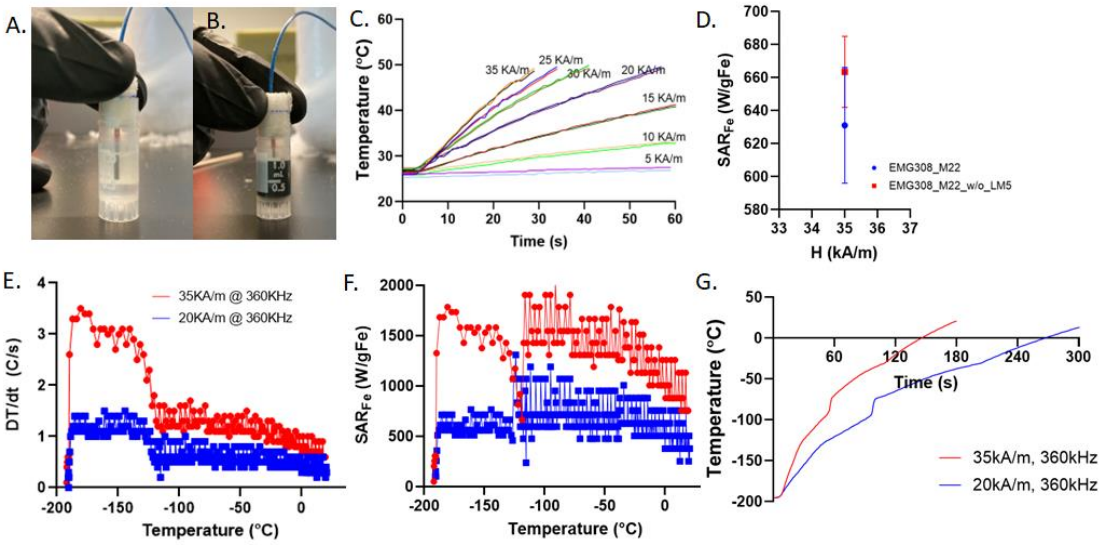


Figure S5.18: SAR (specific absorption rate) Measurement of CPA+IONPs. Photos of A. CPA and B. CPA+IONP in a cryovial with fiber optic temperature probe for SAR measurement. C. Temperature vs time curve for SAR measurement of sIONP+M22 at 360kHz and varying magnetic field strength in 120kW RF coil. D. SAR comparison for EMG308 in M22 with and without LM5 carrier solution. E. Temperature vs time curve, F. Slope of temperature vs time curve and G. Raw values of instantaneous SAR during cryogenic SAR measurement of sIONP in M22 at 35, 20 kA/m and 360 kHz in 120 kW RF coil.

## S5.11 Theoretical SAR: Optimizing Magnetic Field, Frequency for maximum SAR and understanding physical limits of SAR

Specific Absorption Rate (SAR) is an indicator of energy deposition which causes heat dissipation inside a magnetic nanomaterial when present in an alternating magnetic field. Theoretically for a magnetic nanofluid, SAR can be calculated using equation given by Rosensweig [25]

$$SAR_V = \pi\mu_o f H^2 \chi_o \frac{2\pi f\tau}{1+(2\pi f\tau)^2} \sim [\frac{W}{m3}] \qquad \text{(S5.15)}$$

At lower frequencies: $1 \gg (2\pi f\tau)^2 \rightarrow f \ll \frac{1}{2\pi\tau}$

$$SAR_V = \pi\mu_o f H^2 \chi_o 2\pi f\tau = (2\pi^2\mu_o\chi_o\tau)\, f^2 H^2 \qquad \text{(S5.16)}$$

At higher frequencies: $1 \ll (2\pi f\tau)^2 \rightarrow f \gg \frac{1}{2\pi\tau}$

$$SAR_V = (\frac{1}{2\tau}\mu_o\chi_o)\, H^2 \qquad \text{(S5.17)}$$

At low frequencies (f < ~2.6 MHz), the SAR depends directly on frequency (Eq. S5.16). However, at higher frequencies (f > ~2.6 MHz), the relationship with frequency appears to saturate heating becomes somewhat independent of frequency (Eq. S5.17).

## S5.12 Eddy Current Heating Estimation

Eddy current during nanowarming can be estimated using simple correlation as given in literature [23]:

$$P_{eddy} = \sigma(\pi\mu_o)^2(r^2)f^2H^2 \qquad \text{(S5.18)}$$

where H is magnetic field strength, f is frequency, r being radial distance from center of coil or the radius of sample and $\mu_o$ is magnetic permeability of free space. It is to be mentioned that electrical conductivity σ in above correlation should consider both dielectric loss (due to dipolar molecules) and dc electrical conductivity (due to ionic components) contributions.

$$\sigma_{total} = \sigma_{dc} + \omega\varepsilon''\varepsilon_o \qquad \text{(S5.19)}$$

In past, dielectric properties and electrical conductivity has been measured for different single CPA components though these values are limited and absent at lower RF frequencies such as kHz range where nanowarming coils operate (typically 100-500 kHz) for common organ vitrification CPAs and their mixture cocktails (only available for single component CPA such as glycerol at 1-100 kHz [28]). Now, in addition to dielectric heating due to polar molecules relaxation, at temperature above $T_m$ of CPA cocktails, where mobility is increased due to less viscosity, another form of EM heating i.e. ionic heating occurs, whose contribution to eddy heating is added via dc electrical conductivity of CPA solutions in above Eq. S5.19. This ionic contribution is due to the free ions present in the form of salts in the carrier solutions of CPA cocktails (LM5 for M22, Euro-Collins for VS55). This increases effective dielectric loss at near zero temperatures and has been measured in literature at higher frequencies (~MHz) [29, 30]. Therefore, to capture the CPA cocktail behavior and in absence of dielectric properties for organ vitrification CPAs (M22, VS55, 40%EG+0.6MSucrose), we assume dielectric properties from the closet available literature values on CPA+carrier solution (assumed values of σ & ε'' as function of temperature for 50%v/v DMSO + CPT at 27MHz as given elsewhere [29]). Total electrical conductivity is calculated as ~0.1 S/m

at >-20°C and decreases down to <0.02 S/m at ~-80°C [29]. We calculated $P_{eddy}$ using Eq. S5.18 for the 120 kW RF coil as function of radius and magnetic field strength at 360kHz as shown in main Figure 7. It is found that $P_{eddy}$ is within 20% (at >-20C) and reduces down to ~2% (at ~-80°C) of $SAR_V$ i.e., % of nanoparticle heating (calculated assuming 10mgFe/mL IONPs at $SAR_{Fe}$ ~ 1050 W/gFe in the cryogenic -90° to -40°C temperature range and $SAR_{Fe}$ ~ 680 W/gFe in >-30°C temperature range).

For a worst-case scenario, we assumed electrical conductivity as 0.1 S/m which gives higher limit of $P_{eddy}$ and lowest limit of penetration depth. Magnetic nanomaterial is taken as magnetite (iron-oxide EMG308) with properties from literature [25, 26]. Effective diameter of EMG308 is taken as ~12nm which ensures theoretically calculated SAR values are similar to experimental measured $SAR_V$ of EMG308 at 360kHz and 0 to 35 kA/m. First, we calculate SAR as function of magnetic field strength and frequency at 10mgFe/mL EMG308. MATLAB R2023a is used to calculate $SAR_V$ using Eq. S5.15. Next, we calculate $P_{eddy}$ and $SAR_V$ as function of magnetic field and frequency at 6.5 cm radial distance for the RF coil (using Eq. S5.15, S5.18). % $P_{eddy}/SAR_V$ (SAR heating is calculated based upon 10mgFe/mL IONPs) is plotted in Figure S19B which shows the regions where eddy current heating exceeds nanoparticle heating ($P_{eddy}/SAR_V$ >100%) which would provide an upper limit on magnetic field and frequency in enhancing SAR. Neelan relaxation time comes out to be ~6.7 x $10^{-8}$ sec for d~12nm IONPs. Another important constraint for maximizing field and frequency is from penetration depth of RF fields which can be estimated using the simple correlation as below. Penetration or skin depth for an RF wave can be defined as the length scale at which the electromagnetic field (H or E) has fallen to ~37% (1/e) of its peak value and can be approximated as simple formula below.

$$\delta = \frac{1}{\sqrt{\sigma \pi \mu f}} \qquad \text{(S5.20)}$$

Now, theoretically one would want to operate at as high frequency as possible for higher heating as SAR increases with frequency though only upto a point (inflection point: $f_o$) beyond which it saturates. On the other hand, eddy heating would also start to become significantly large at higher frequencies (MHz) as its proportional to sq. of frequency and SAR would roughly become independent of frequency. To find the maximum field and frequency, we use two criterion 1. eddy heating assigned to limit at certain threshold of SAR of magnetic nanoparticles ($P_{eddy}/SAR_V$ = 20%) and 2. Penetration depth > 20 cms at all times. This gives us field strength < 22 kA/m and frequency < 3.3 MHz as shown in region blue region of Figure S19B.

## S5.13 Calculations for maximum IONP concentration based upon volume packing fraction

For simple cubic 3D packing, maximum packing fraction can be derived simply below.

$$\emptyset_m = \frac{\frac{4}{3}\pi r^3}{(2*r)^3} = \frac{\pi}{6} = 0.524 \qquad \text{(S5.21)}$$

Now we can correlate packing fraction with

$$\emptyset_m = \frac{V_{Fe}}{V_{CPA\ solution}} = \frac{(\frac{mass_{Fe}}{\rho_{Fe}})}{V_{CPA\ solution}} = \frac{(\frac{C_{Fe} * V_{CPA\ solution}}{\rho_{Fe}})}{V_{CPA\ solution}} = \frac{C_{Fe}}{\rho_{Fe}}$$

Assuming IONPs as magnetite whose density is 5180 mgFe/mL [25], and plugging maximum packing fraction, we can estimate maximum IONP concentration theoretical limit as:

$$C_{Fe} = \emptyset_m * \rho_{Fe} = 0.524 * 5180 = 2714.3\ mgFe/mL$$

Now, for a coated IONP, let's consider hydrodynamic diameter as effective particle diameter (see Figure S18C schematic of packing fraction) which is for phosphonate/polyethylene glycol coated iron oxide nanoparticles pIONPs ~ 40nm [27]. In this case maximum packing fraction can be calculated as:

$$d_{hydrodynamic}\ (40\ nm) = 4 * d_{particle}\ (10nm)$$

$$\emptyset_m = \frac{\frac{4}{3}\pi {r_{particle}}^3}{(2 * r_{hydrodynamic})^3} = \frac{\frac{4}{3}\pi {r_{particle}}^3}{(2 * (4 * r_{particle}))^3} = \frac{0.524}{64} \sim 0.0082$$

$$C_{Fe} = \emptyset_m * \rho_{Fe} = 0.0082 * 5180 = 42.4\ mgFe/mL$$

Similarly, for silica-coated IONPs - sIONP (hydrodynamic diameter ~ 100nm), this maximum IONP concentration comes out to be ~2.69 mgFe/mL.

Practically we have found that these maximum IONP conc. are larger i.e. sIONP~ 15-20 mgFe/mL, pIONP ~100-150 mgFe/mL based upon the fact that IONP solution start to become too viscous such as a gel like texture upon increasing any further concentration [1].

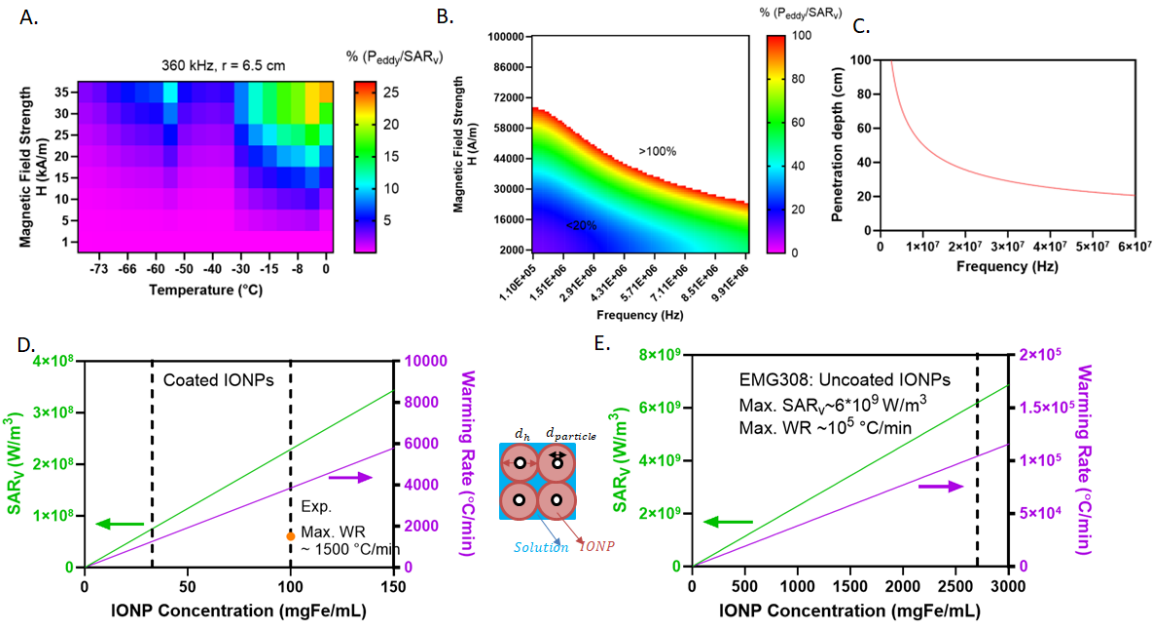


Figure S5.19: Theoretical maximum $SAR_V$ (nanoparticle heating): $SAR_V$ Limits with magnetic field, frequency and IONP concentration. A. Heat map plot of $P_{eddy}/SAR_V$ as a function of temperature and magnetic field strength at a fixed radial distance (r- from the center of RF coil) of 6.5 cm (corresponding to 120 kW RF coil) and 360 kHz. B. Calculated ratio of $P_{eddy}$ to $SAR_V$ (modeled using Rosenweig [37]) calculated in a broader frequency and field strength at room temperature (electrical conductivity~ 0.1 S/m) depicting the optimum regime of nanoparticle heating (blue region where eddy heating is restricted to <20% of nanoparticle heating as example). C. Plot of penetration depth with frequency. This is a balance between penetration depth, eddy heating and nanoparticle heating. $SAR_V$ variation with IONP concentration for D. coated IONPs and E. uncoated IONPs at 15kA/m, 1.8 MHz (being the max. field and. The theoretical maximum IONP concentration is calculated using maximum packing fraction. Maximum $SAR_V$ ~ $6*10^9$ W/$m^3$ which leads to maximum nanowarming rate of ~112,000 °C/min.

## S5.14 Nanowarming of mL to liter scale CPA volumes

We rewarmed 1mL cryovial containing VMP with EMG308 at ~100mgFe/mL after being vitrified in a LN2 bath. Rearming was conducted from LN2 temperature of -196°C and stopped at near 0°C. Temperature was recorded every 0.2 sec for such high concentration of IONP where ultra-fast warming rates were expected. Warming rates are plotted in Figure S20 and calculated as

~1500°C/min in 0 to -100°C range. Further, EMG308 in M22 at ~50mgFe/mL and 4mgFe/mL were also tested showing warming rate dependence (approximately linear) on IONP concentration in CPA solutions.

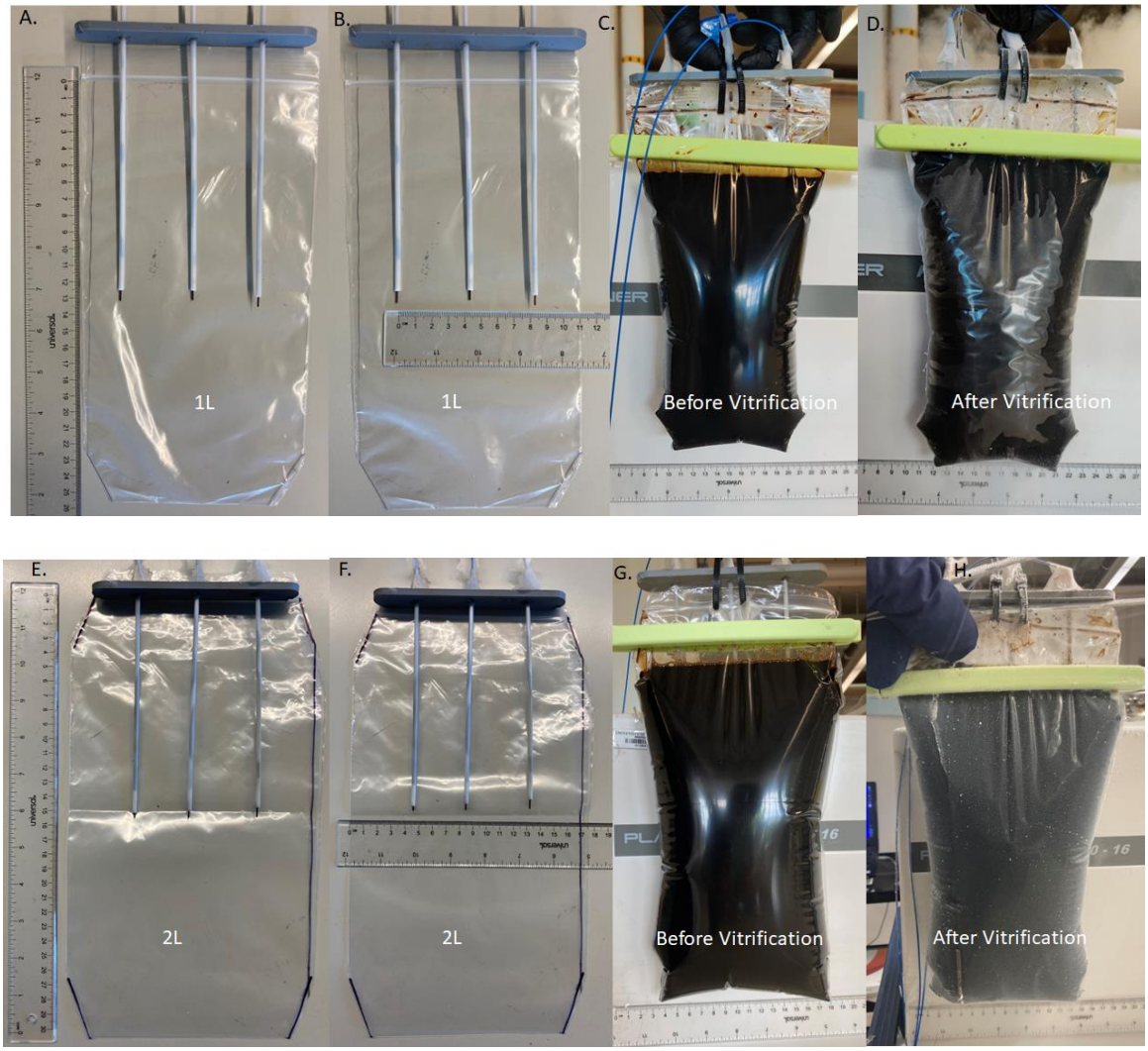


Figure S5.20: Photos of thermometry jigs for liter scale nanowarming. EMG308+M22 cryobag with fiber optic probe placement for A, B. 1L volume and E, F. 2L volume. EMG308+M22 before and after vitrification C, D. 1L volume and G, H. 2L volume.

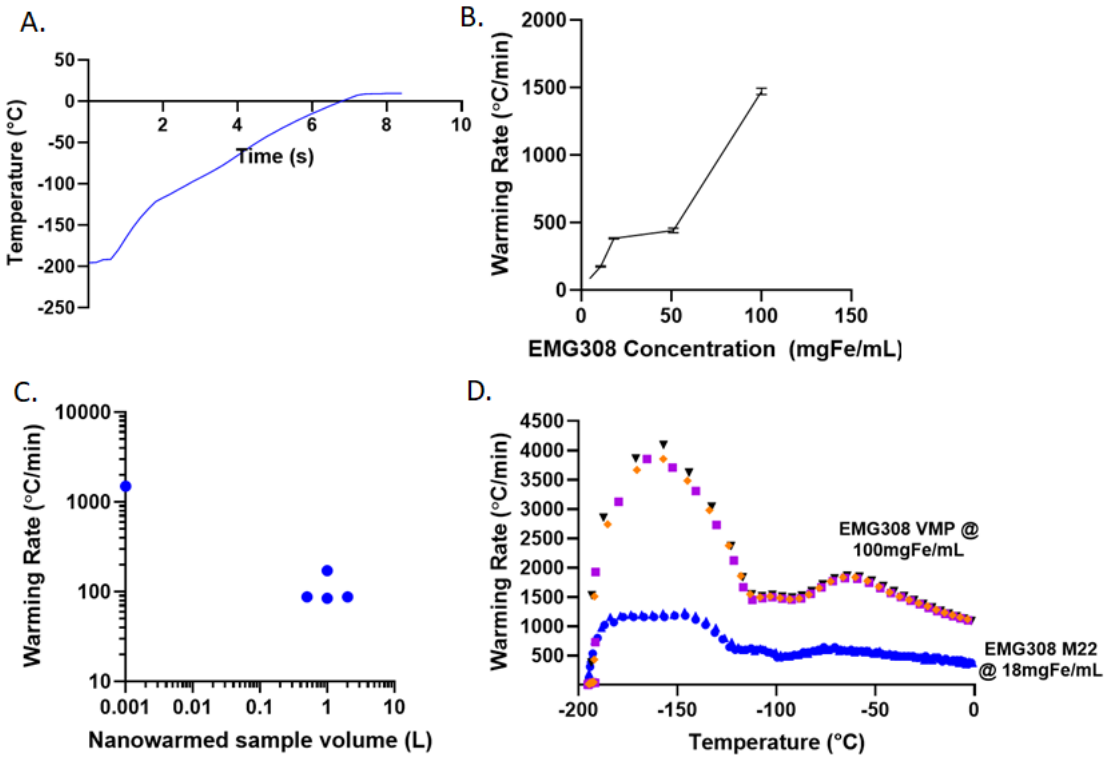


Figure S5.21: Nanowarming Heating Demonstration from 1mL to 2L CPA volumes. A. Thermometry (Temperature vs time) for nanowarming of 1mL100mgFe/mL EMG308 in VMP from cryogenic vitrified state. B. Warming rate measured for various IONP concentrations. C. Warming Rates for all the range of volumes rewarmed from vitrified cryogenic state using nanowarming. D. Warming rate variation with temperature for small volume (1mL) higher IONP concentrations (>10mgFe/mL) samples. Instantaneous WR reaches as high as ~4000°C/min for 100mgFe/mL sample. Various colors represent 3 repeats.

## S5.15 Calculation of required minimum vitrifiable CPA concentration in CRF for a given $L_C$

Critical cooling rate (CCR) decreases with increasing CPA concentration. Han et. al. [31] fitted CCR of various single component CPAs with their total solute (%w/w) concentration as given below:

$$CCR\left[\frac{^{\circ}C}{min}\right] = 10^{7} e^{-0.269 * Conc.\ [\%^{w}/_{w}]} \quad \text{(S5.22)}$$

where Conc. represents CPA concentration in %w/w.

Now, for a given $L_C$ we can estimate achievable minimum cooling rate inside a control rate freezer (CRF) based upon Gangwar et. al. [32] where CR decreases exponentially with increasing size for all 3 the CPAs analyzed- VS55, M22, DP6. Now to simplify and get a first-order estimate of CRs we assume M22 thermal properties represent CPA throughout the range of CPA concentration of interest (say >40%w/w).

$$CR\ \left[\frac{^\circ C}{min}\right] = 0.1 * 10^{a+b*\log(L_C\ [cm])} \qquad \text{(S5.23)}$$

where a is 1.399 and b is -1.609 for M22.

For minimum concentration which can vitrify, achievable CR (Eq. 23) is equated to CCR (Eq. S5.22):

$$CCR = CR$$

$$10^7 * e^{-0.269\ Conc.} = 0.1 * 10^{(1.399-1.609*\log L_C)}$$

$$Conc.\ [\%\frac{w}{w}] = 3.72 * (18.42 - 2.3 * (1.399 - 1.609 * \log L_C\ [cm])) \quad \text{(S5.24)}$$

Now, for a $L_C$~ 2.2 cm (case of human liver) which represents our experimental 3L volume tested, CPA conc. needed to vitrify comes out to be ~ 61.2 %w/w which is higher than VS55, EG+sucrose CPA concentrations and lower than M22 (see Table S5.1) hence successful vitrification.

As mentioned earlier these results are limited to the higher CPA concentration range which is the case for organ vitrification. Note that our calculation and min. vitrifiable CPA concentration plot is based upon the assumption of fitting the CCR vs CPA concentration fit for single component permeating CPAs. CPA cocktail mixtures such as VS55, DP6, M22 were shown to still fall on that CCR vs Conc. (%w/w) curve within <10% variation. Also the more amount of non-permeating components (such as sugars, ice-blockers, etc.) in a CPA would lead to deviation from these curves (downwards shift in CCR vs CPA concentration and Min. vitrifiable conc vs $L_C$). As an example, 40%EG+0.6Msucrose CPA (larger amount of sucrose~0.6M in addition to carrier solution sugar~0.2) would deviate more than M22 (carrier solution sugar~0.2M and ice inhibitors ~<0.02) followed by VS55 (carrier solution sugars~0.2M). Lastly, effects such as tissue confinement would also move these estimates to the benefit by lowering CCRs and hence amount of vitrifiable CPA concentrations though tissue sub-optimal equilibration would move curves upwards acting to the worse.

# References for supplementary information for chapter 5


1. Gao, Z., et al., *Preparation of Scalable Silica-Coated Iron Oxide Nanoparticles for Nanowarming.* Advanced Science, 2020. **7**(4): p. 1901624.
2. Sharma, A., et al., *Vitrification and Nanowarming of Kidneys.* Advanced Science, 2021. **8**(19): p. 2101691.
3. Fahy, G.M., et al., *Physical and biological aspects of renal vitrification.* Organogenesis, 2009. **5**(3): p. 167-175.
4. GM, F., W. B, and W. J, *Cryopreservation of complex systems: the missing link in the regenerative medicine supply chain.* Rejuvenation research, 2006. **9**(2).
5. Sharma, A., et al., *Cryopreservation of whole rat livers by vitrification and nanowarming.* Annals of Biomedical Engineering, 2023. **51**(3): p. 566-577.
6. PM, M., *Nucleation and Crystal Growth in a Vitrification Solution Tested for Organ Cryopreservation by Vitrification.* Cryobiology, 1993. **30**(5).
7. Han, Z., et al., *Supplemented phase diagrams for vitrification CPA cocktails: DP6, VS55 and M22.* Cryobiology, 2022.
8. Fahy, G.M., et al., *Cryopreservation of organs by vitrification: perspectives and recent advances.* Cryobiology, 2004. **48**(2): p. 157-178.
9. LE, E., et al., *Thermal conductivity of cryoprotective agents loaded with nanoparticles, with application to recovery of preserved tissues and organs from cryogenic storage.* PloS one, 2020. **15**(9).
10. S, P., et al., *Measurement of Specific Heat and Crystallization in VS55, DP6, and M22 Cryoprotectant Systems With and Without Sucrose.* Biopreservation and biobanking, 2018. **16**(4).
11. Etheridge, M.L., et al., *RF heating of magnetic nanoparticles improves the thawing of cryopreserved biomaterials.* https://doi.org/10.1142/S2339547814500204, 2014.
12. Solanki, P.K., *Thermomechanical Stress in Cryopreservation with Applications to Large-Size Vitrification*. 2020, Carnegie Mellon University.
13. Wowk, B. and G. Fahy, *Toward large organ vitrification: extremely low critical cooling and warming rates of M22 vitrification solution.* Cryobiology, 2005. **51**: p. 362.
14. Rabin, Y., et al., *Fracture formation in vitrified thin films of cryoprotectants.* Cryobiology, 2006. **53**(1): p. 75-95.
15. Solanki, P.K. and Y. Rabin, *Perspective: Temperature-Dependent Density And Thermal Expansion Of Cryoprotective Agents.* CryoLetters, 2022. **43**(1): p. 1-9.
16. Rubinsky, B., E.G. Cravalho, and B. Mikic, *Thermal stresses in frozen organs.* Cryobiology, 1980. **17**(1): p. 66-73.
17. Schlegel, A., et al., *Protective mechanisms of end-ischemic cold machine perfusion in DCD liver grafts.* Journal of hepatology, 2013. **58**(2): p. 278-286.
18. Botea, F., et al., *An exploratory study on isochoric supercooling preservation of the pig liver.* Biochemistry and Biophysics Reports, 2023. **34**: p. 101485.
19. Gao, Z., et al., *Vitrification and rewarming of magnetic nanoparticle-loaded rat hearts.* Advanced Materials Technologies, 2022. **7**(3): p. 2100873.
20. Gangwar, L., et al., *Perspective: A Guide to Successful ml to L Scale Vitrification and Rewarming.* CryoLetters, 2022. **43**(6): p. 303-315.
21. Bordelon, D.E., et al., *Modified solenoid coil that efficiently produces high amplitude AC magnetic fields with enhanced uniformity for biomedical applications.* IEEE transactions on magnetics, 2011. **48**(1): p. 47-52.

22. Manuchehrabadi, N., et al., *Improved tissue cryopreservation using inductive heating of magnetic nanoparticles.* Science translational medicine, 2017. **9**(379): p. eaah4586.
23. Attaluri, A., et al., *Design and construction of a Maxwell-type induction coil for magnetic nanoparticle hyperthermia.* International journal of hyperthermia, 2020. **37**(1): p. 1-14.
24. Ring, H.L., et al., *The impact of data selection and fitting on SAR estimation for magnetic nanoparticle heating.* International Journal of Hyperthermia, 2020. **37**(3): p. 100-107.
25. Rosensweig, R.E., *Heating magnetic fluid with alternating magnetic field.* Journal of magnetism and magnetic materials, 2002. **252**: p. 370-374.
26. Jordan, A., M.L. Etheridge, and J.C. Bischof, -*Magnetic Nanoparticles for Cancer Therapy*, in *Physics of Thermal Therapy*. 2016, CRC Press. p. 310-335.
27. Pasek-Allen, J.L., et al., *Phosphonate coating of commercial iron oxide nanoparticles for nanowarming cryopreserved samples.* Journal of Materials Chemistry B, 2022.
28. Michelson, S. and S. Evans, *Dielectric properties of supercooled cryoprotectant agents.* Physics in Medicine & Biology, 1996. **41**(10): p. 2053.
29. Evans, S., *Electromagnetic rewarming: the effect of CPA concentration and radio source frequency on uniformity and efficiency of heating.* Cryobiology, 2000. **40**(2): p. 126-138.
30. Robinson, M.P. and D.E. Pegg, *Rapid electromagnetic warming of cells and tissues.* IEEE transactions on biomedical engineering, 1999. **46**(12): p. 1413-1425.
31. Gangwar, L., et al., Perspective: A Guide to Successful ml to L Scale Vitrification and Rewarming. CryoLetters, 2022. 43(6): p. 303-315.
32. Han, Z. and J.C. Bischof, Critical Cooling and Warming Rates as a Function of CPA Concentration. 2020.

# Chapter 6. Conclusion and Future Directions

## Concluding remarks

In summary, this work focused on the importance of thermal properties (compiled from literature), dielectric properties (measured experimentally) for predicting success and avoiding failure, i.e., ice crystallization and physical cracking/fractures during vitrification and nanowarming. A universally applicable numerical model based upon a sample's characteristic length ($L_C$) and thermal properties that combines heat transfer with thermal stress has been established, which will provide guidance for successful vitrification and rewarming in a variety of biological systems. Lastly by applying modeled thermal protocols, experimental demonstration of the first-known successful vitrification of large-scale (liter volumes) in a physical (CPA volumes) and biological (porcine liver) system and rewarming of such systems using a novel, state-of-art 120 KW RF coil is shown in this work, which paves a pathway to scale up human organ vitrification and rewarming in near future.

Note that conclusion/discussion is provided at end of each chapter for a more comprehensive summary.

## Future work

There are many interesting possibilities for extension of this work, some of which are described here. Thermal conductivity (k) and specific heat capacity ($C_p$) of tissues such as kidney, liver and heart permeated with organ vitrification CPAs such as VMP, M22, VS55 would be relevant to be measured in future work as it is currently unavailable. Further, dielectric properties (dielectric constant and loss) of tissues with and without CPA permeation in low temperature would be another important measurement to be performed for understanding of tissue dielectric behavior either for nanowarming or dielectric rewarming. For computational modeling, 3D geometric models of organs which include vasculature would be important to understand the effect of vascular variations among different organs on nanoparticle heating during nanowarming. Lastly, as the challenge on large-scale volume vitrification falls back on cooling capabilities, faster and uniform cooling technologies need to be investigated in future studies for scaling vitrification success to human organs. Additionally, RF coils can be optimized further with higher magnetic field and frequency to maximize nanoparticle heating for achieving highest rewarming rates for liter-scale volumes.

# Appendix

## Appendix 1- Thermophysical Property Tables for Chapter 2

Table A1.1: Thermal conductivity as function of temperature for various CPAs compiled from literature.

| Sample | Temperature (ºC) | Thermal Conductivity [W/mK] | Measurement Technique | Source |
|---|---|---|---|---|
| Water/Ice | 0 | 2.16 | Steady State Guarded Cylinder | [1, 2] |
| | -10 | 2.26 | | |
| | -20 | 2.38 | | |
| | -30 | 2.50 | | |
| | -40 | 2.63 | | |
| | -50 | 2.77 | | |
| | -60 | 2.93 | | |
| | -80 | 3.27 | | |
| | -100 | 3.69 | | |
| | -120 | 4.2 | | |
| | -140 | 4.9 | | |
| | -160 | 5.7 | | |
| | -180 | 7 | | |
| | -200 | 8.9 | | |
| | -220 | 12.2 | | |
| | -240 | 20 | | |
| Water/Ice | -5 | 2.3 | Transient Hot Bridge | [3] |
| | -15 | 2.32 | | |
| | -20 | 2.40 | | |
| | -25 | 2.43 | | |
| | -30 | 2.44 | | |
| Water/Ice | -2.4 | 1.9 | Transient Hot Wire | [4] |

| | | | | |
|---|---|---|---|---|
| | -10 | 2.3 | | |
| | -22 | 2.4 | | |
| | -40 | 2.5 | | |
| | -58 | 2.9 | | |
| | -81 | 3.2 | | |
| | -92 | 3.3 | | |
| | -102 | 3.6 | | |
| | -113 | 3.7 | | |
| | -124 | 3.9 | | |
| | -132 | 4.1 | | |
| | -142 | 4.5 | | |
| | -152 | 4.6 | | |
| | -167 | 5.4 | | |
| | -177 | 5.9 | | |
| Propylene Glycol (100%v/v) | 27 | 0.26 | Heat Probe | [5] |
| | -20 | 0.19 | | |
| Propylene Glycol (75%v/v) | -20 | 0.29 | | |
| Propylene Glycol (50%v/v) | -20 | 0.36 | | |
| Glycerol (100%v/v) | -20 | 0.26 | Heat Probe | [5] |
| Glycerol (75%v/v) | -20 | 0.3 | | |
| Glycerol (50%v/v) | -20 | 0.36 | | |
| 1 M Glycerol + 1xPBS | -28 | 1.95 | Thermistor (Pulse decay method) | [6, 7] |
| | -64 | 2.33 | | |
| | -109 | 2.83 | | |
| | -146 | 3.11 | | |
| | -27 | 1.61 | | |

| | | | | |
|---|---|---|---|---|
| 2 M Glycerol + 1xPBS | -64 | 1.96 | | |
| | -108 | 2.15 | | |
| | -147 | 2.25 | | |
| 6 M Glycerol + 1xPBS | -28 | 0.82 | | |
| | -65 | 1.27 | | |
| | -108 | 1.05 | | |
| | -147 | 0.97 | | |
| Glycerol (100%v/v) | 20.5 | 0.3 | Transient Hot Wire | [4] |
| | 0.3 | 0.3 | | |
| | -19.8 | 0.3 | | |
| | -39.9 | 0.3 | | |
| | -80.2 | 0.3 | | |
| | -120.3 | 0.3 | | |
| | -139.8 | 0.3 | | |
| | -160.3 | 0.3 | | |
| DMSO (100%v/v)~ 14 M | -20 | 0.2 | Heat Probe | [5] |
| DMSO (75%v/v)~ 10.6 M | -20 | 0.24 | | |
| DMSO (50%v/v)~7 M | -20 | 0.32 | | |
| 2 M DMSO | 0 | 0.50 | Transient Hot Wire | [4] |
| | -20 | 1.44 | | |
| | -60 | 1.69 | | |
| | -100 | 1.99 | | |
| | -140 | 2.20 | | |
| 6 M DMSO | 0 | 0.38 | | |
| | -20 | 0.38 | | |
| | -60 | 0.59 | | |
| | -100 | 0.72 | | |

| | | | | |
|---|---|---|---|---|
| | -140 | 0.77 | | |
| 10 M DMSO | 0 | 0.30 | | |
| | -20 | 0.28 | | |
| | -60 | 0.27 | | |
| | -100 | 0.26 | | |
| | -140 | 0.25 | | |
| M22 in LM5 | 27 | 0.40 | Hot Probe | [8] |
| | 20 | 0.39 | | |
| | 7 | 0.38 | | |
| | -0.1 | 0.37 | | |
| | -13 | 0.35 | | |
| | -21 | 0.34 | | |
| | -34 | 0.33 | | |
| | -41 | 0.43 | | |
| | -196 | 0.84 | | |
| M22 in LM5 | -2 | 0.31 | Transient Hot Wire | [9] |
| | -19 | 0.31 | | |
| | -42 | 0.31 | | |
| | -61 | 0.31 | | |
| | -80 | 0.31 | | |
| | -95 | 0.31 | | |
| | -112 | 0.34 | | |
| | -121 | 0.33 | | |
| | -140 | 0.32 | | |
| | -157 | 0.31 | | |
| | -169 | 0.3 | | |
| | -179 | 0.29 | | |
| DP6 in EC | 0 | 0.30 | Transient Hot Wire | [9, 10] |
| | -20 | 0.32 | | |
| | -40 | 0.53 | | |
| | -70 | 0.36 | | |
| | -140 | 0.35 | | |

| | | | | |
|---|---|---|---|---|
| VS55 in EC | -1 | 0.35 | Transient Hot Wire | [9] |
| | -22 | 0.35 | | |
| | -38 | 0.34 | | |
| | -50 | 0.46 | | |
| | -59 | 0.53 | | |
| | -68 | 0.35 | | |
| | -83 | 0.33 | | |
| | -99 | 0.33 | | |
| | -110 | 0.37 | | |
| | -123 | 0.34 | | |
| | -135 | 0.33 | | |
| | -148 | 0.33 | | |
| | -169 | 0.32 | | |
| | -179 | 0.32 | | |
| VS55 in Celsior | 5 | 0.34 | Thermal Probe | [5] |
| | -5 | 0.34 | | |
| | -15 | 0.32 | | |
| | -25 | 0.32 | | |
| | -196 | 0.39 | | |

Table A1.2: Thermal conductivity as function of temperature for various animal tissues compiled from literature.

| Tissue Type | Temperature (°C) | Thermal Conductivity (W/m.K) | Measurement Technique | Source |
|---|---|---|---|---|
| Blood Plasma | -10 | 2.03 | - | [11] |
| | -20 | 2.10 | | |
| | -40 | 2.31 | | |
| | -60 | 2.51 | | |
| | -80 | 2.86 | | |
| | -100 | 3.19 | | |

| | | | | |
|---|---|---|---|---|
| Whole Blood | -10 | 1.64 | | |
| | -20 | 1.74 | | |
| | -40 | 1.92 | | |
| | -60 | 2.14 | | |
| | -80 | 2.38 | | |
| | -100 | 2.66 | | |
| Rabbit Kidney Cortex | -10 | 1.52 | Thermistor Probe | [12] |
| | -20 | 1.34 | | |
| | -30 | 1.31 | | |
| | -40 | 1.46 | | |
| | -50 | 1.51 | | |
| | -60 | 1.50 | | |
| | -70 | 1.52 | | |
| Rabbit Kidney | 20 | 0.49 | Self-Heated Thermistor | [13] |
| | 10 | 0.48 | | |
| | 0 | 0.48 | | |
| | -10 | 0.89 | | |
| | -20 | 1.17 | | |
| | -30 | 1.33 | | |
| | -40 | 1.49 | | |
| Rabbit Liver | 20 | 0.52 | Self-Heated Thermistor | [13] |
| | 10 | 0.51 | | |
| | 0 | 0.50 | | |
| | -10 | 1.04 | | |
| | -20 | 1.39 | | |
| | -30 | 1.57 | | |
| | -40 | 1.75 | | |
| Rabbit Liver | 8.8 | 0.45 | - | [14] |
| | -13.7 | 1.26 | | |
| | -24.8 | 1.33 | | |
| | -35.7 | 1.39 | | |
| | -45.5 | 1.48 | | |

| | | | | |
|---|---|---|---|---|
| | -52.5 | 1.47 | | |
| | -84.2 | 1.56 | | |
| | -111.3 | 1.51 | | |
| | -153.3 | 1.79 | | |
| | -180 | 1.84 | | |
| Rabbit Heart | 20 | 0.51 | Self-Heated Thermistor | [13] |
| | 10 | 0.50 | | |
| | 0 | 0.49 | | |
| | -10 | 1.01 | | |
| | -20 | 1.22 | | |
| | -30 | 1.48 | | |
| | -40 | 1.7 | | |
| Rabbit Carotid Artery | 20 | 0.41 | Self-Heated Thermistor | [13] |
| | 10 | 0.40 | | |
| | 0 | 0.39 | | |
| | -10 | 0.90 | | |
| | -20 | 1.23 | | |
| | -30 | 1.42 | | |
| | 20 | 1.56 | | |
| Porcine Pulmonary Vein | 36 | 0.57 | 3ω method | [15] |
| | 14 | 0.47 | | |
| | -14 | 1.14 | | |
| | -31 | 1.44 | | |
| Porcine Esophagus | 36 | 0.55 | | |
| | 14 | 0.48 | | |
| | -17 | 1.61 | | |
| | -37 | 1.84 | | |
| Porcine Phrenic Nerve | 36 | 0.45 | | |
| | 14 | 0.50 | | |
| | -14 | 1.29 | | |
| | -34 | 1.84 | | |
| | 37 | 0.54 | | |

| | | | | |
|---|---|---|---|---|
| Porcine Myocardium | 0.1 | 0.44 | | |
| | -26 | 1.74 | | |
| | -94 | 2.05 | | |
| | -148 | 2.31 | | |
| Porcine Fat | 0 | 0.19 | - | [16] |
| | -5 | 0.23 | | |
| | -10 | 0.25 | | |
| | -20 | 0.29 | | |
| Porcine Cardiac Muscle | 8 | 0.48 | Transient Hot Bridge | [3] |
| | -0.8 | 0.5 | | |
| | -3.5 | 0.66 | | |
| | -5 | 0.87 | | |
| | -10 | 1.32 | | |
| | -16 | 1.37 | | |
| | -24 | 1.45 | | |
| Porcine Leg | 6 | 0.45 | - | [17] |
| | -8 | 1.05 | | |
| | -14 | 1.13 | | |
| Porcine Neck | -8ºC | 0.78 | - | [18] |
| | -8.4ºC | 0.84 | | |
| | -9ºC | 0.41 | | |
| Porcine Liver | 5 | 0.37 | Hot Probe | [19] |
| | -15 | 0.36 | | |
| | -35 | 0.69 | | |
| | -196 | 1.27 | | |
| Porcine Liver | -11 | 1.6 | Thermistor (Pulse decay method) | [6, 20] |
| | -64 | 1.75 | | |
| | -112 | 1.9 | | |
| | -147 | 2.01 | | |
| Canine Myocardium Muscle | 5 | 0.63 | - | [3, 21] |
| | -1.2 | 0.96 | | |
| | -2.3 | 1.3 | | |

| | | | | |
|---|---|---|---|---|
| (79.5% water content) | -4 | 1.8 | | |
| | -8 | 2.15 | | |
| | -25 | 2.43 | | |
| | -40 | 2.39 | | |
| | -180 | 2.15 | | |

Table A1.3: Thermal conductivity as function of temperature for various human tissues compiled from literature.

| Tissue Type | Temperature (°C) | Thermal Conductivity (W/m.K) | Measurement Technique | Source |
|---|---|---|---|---|
| Human Muscle (cross-striated, flow-parallel fiber) | 0 | 0.48 | - | [3, 14] |
| | -44 | 1.93 | | |
| | -545 | 1.88 | | |
| | -72 | 1.79 | | |
| | -132 | 2.25 | | |
| | -173 | 2.44 | | |
| | -177 | 2.61 | | |
| Human Muscle (cross-striated, flow-perpendicular fiber) | -36 | 1.63 | - | |
| | -60 | 1.54 | | |
| | -173 | 1.72 | | |
| Human Skeletal Muscle (74.5% water content) | 9 | 0.64 | - | [3, 21] |
| | -2 | 1.13 | | |
| | -5 | 1.71 | | |
| | -16 | 2.05 | | |
| | -25 | 2.13 | | |
| | -40 | 2.09 | | |
| | -60 | 1.98 | | |
| Human Liver (62% water content) | 8 | 0.37 | - | |
| | -1.8 | 0.42 | | |

| | | | | |
|---|---|---|---|---|
| | -4.7 | 0.89 | | |
| | -9.6 | 1.23 | | |
| | -14.7 | 1.44 | | |
| | -19.8 | 1.59 | | |
| | -25.3 | 1.62 | | |
| | -40 | 1.64 | | |
| | -180 | 1.54 | | |
| Human Liver | 16.8 | 0.47 | - | [3, 14] |
| | 1.4 | 0.43 | | |
| | -84.4 | 1.64 | | |
| | -99.6 | 1.70 | | |
| | -141.4 | 1.87 | | |
| | -147 | 1.54 | | |
| | -151.2 | 1.89 | | |
| | -170.6 | 1.93 | | |
| Human Prostate | -0.9 | 0.5 | - | |
| | -10.2 | 1.8 | | |
| | -20.4 | 2.00 | | |
| | -27.4 | 2.05 | | |
| | -40.6 | 2.07 | | |
| | -160.5 | 2.3 | | |
| Human Kidney (Cortex) | 5.3 | 0.46 | - | |
| | -22.5 | 1.48 | | |
| | -35.5 | 1.48 | | |
| | -43.3 | 1.66 | | |
| | -74.5 | 1.61 | | |
| | -133.3 | 1.94 | | |
| | -135.4 | 1.61 | | |
| | -157.2 | 2.01 | | |
| | -161.5 | 1.63 | | |
| | -177.4 | 2.09 | | |
| | -13.4 | 1.5 | - | |

| | | | | |
|---|---|---|---|---|
| Human Brain (Grey matter) | -22.7 | 1.6 | | |
| | -30.5 | 1.7 | | |
| | -46.4 | 1.72 | | |
| | -56.6 | 1.78 | | |
| | -88.3 | 1.95 | | |
| | -108.5 | 1.84 | | |
| | -128.6 | 1.85 | | |
| | -131.3 | 2.2 | | |
| | -158.4 | 1.79 | | |
| | -162.5 | 2.19 | | |
| | -163.4 | 1.84 | | |
| | -180.2 | 2.36 | | |
| Human Brain (White matter) | 19.7 | 0.43 | - | |
| | 4.6 | 0.41 | | |
| | -14.5 | 1.08 | | |
| | -26.6 | 1.36 | | |
| | -63.4 | 1.48 | | |
| | -116.3 | 1.58 | | |
| | -134.4 | 1.44 | | |
| | -154 | 1.72 | | |
| Human Brain (Grey 50% and White 50% matter) | 12 | 0.47 | - | |
| | -20 | 1.44 | | |
| | -71 | 1.67 | | |
| | -108 | 1.66 | | |
| | -138 | 1.94 | | |
| | -161 | 2.03 | | |

Table A1.4: Thermal conductivity as function of temperature for various Tissue permeated with CPAs compiled from literature.

| Tissue+CPA | Temperature (°C) | Thermal Conductivity (W/m.K) | Measurement Technique | Source |
|---|---|---|---|---|
| Porcine Liver, treated with 1X PBS+ 2M Glycerol | -10 | 1.56 | Thermistor | [6, 20] |
| | -64 | 1.68 | | |
| | -108 | 1.78 | | |
| | -146 | 1.73 | | |
| Porcine Liver, treated with 1XPBS + 6M glycerol | -13 | 1.0 | | |
| | -64 | 1.55 | | |
| | -110 | 1.42 | | |
| | -148 | 1.24 | | |
| Porcine Liver, treated with 1XPBS + 8M glycerol | -10 | 0.65 | | |
| | -64 | 1.27 | | |
| | -109 | 1.07 | | |
| | -149 | 0.86 | | |
| Porcine Liver+VS55 | 5 | 0.372 | Thermal Probe | [19] |
| | -15 | 0.356 | | |
| | -35 | 0.686 | | |
| | -196 | 1.266 | | |

Table A1.5: Specific Heat capacity as function of temperature for various CPAs compiled from literature. Note, measurement technique for all the data is DSC as discolosed in source references.

| CPA Type | Temperature (°C) | Specific Heat (J/kg.K) | Source |
|---|---|---|---|
| Water/Ice | 42 | 4200 | [1] |
| | 9.8 | 4200 | |
| | -2.7 | 2100 | |
| | -23.3 | 1900 | |
| | -42.3 | 1800 | |

| | | | |
|---|---|---|---|
| | -66.9 | 1600 | |
| | -92.7 | 1400 | |
| | -121.4 | 1200 | |
| | -152.9 | 1000 | |
| 1 M Glycerol + 1xPBS | 0 | 3969 | [6, 7] |
| | -73 | 1641 | |
| | -110 | 1216 | |
| | -148 | 959 | |
| 2 M Glycerol + 1xPBS | -5 | 3781 | |
| | -73 | 1712 | |
| | -110 | 1206 | |
| | -148 | 903 | |
| 6 M Glycerol + 1xPBS | -20 | 2984 | |
| | -73 | 1996 | |
| | -110 | 1114 | |
| | -148 | 834 | |
| VS55 (8.4M) | -1.5 | 3011 | [22, 23] |
| | -21 | 2925 | |
| | -44 | 2819 | |
| | -79 | 2715 | |
| | -118 | 2968 | |
| | -128 | 1134 | |
| | -150 | 985 | |
| M22 (9.345M) | 0 | 3430 | |
| | -18 | 3378 | |
| | -40 | 3318 | |
| | -76 | 3180 | |
| | -119 | 3324 | |
| | -130 | 1461 | |
| | -149 | 1318 | |
| DP6 (6M) | 0 | 2984 | |
| | -21 | 2824 | |

| | | | |
|---|---|---|---|
| | -44 | 2675 | |
| | -88 | 2460 | |
| | -110 | 2653 | |
| | -121 | 1224 | |
| | -149 | 888 | |
| VS55 in Celsior | 25 | 3169 | [19] |
| | 7 | 3083 | |
| | -3 | 2008 | |
| | -23 | 2033 | |

Table A1.6: Specific Heat capacity as function of temperature for various tissue types compiled from literature. Note, measurement technique for all the data is DSC as discolosed in source references.

| Tissue Type | Temperature (°C) | Specific Heat (J/kg.K) | Source |
|---|---|---|---|
| Porcine Pulmonary Vein | 39 | 3340 | [23, 24] |
| | 5 | 3270 | |
| | 1 | 2820 | |
| | -34 | 1870 | |
| | -46 | 1740 | |
| | -72 | 1490 | |
| | -84 | 1380 | |
| Porcine Esophagus | 39 | 3490 | |
| | 9 | 3390 | |
| | -30 | 1920 | |
| | -52 | 1630 | |
| | -74 | 1430 | |
| | -86 | 1290 | |
| Porcine Phrenic Nerve | 33 | 3570 | |
| | 13 | 3470 | |
| | -18 | 2440 | |
| | 30 | 1830 | |

| | | | |
|---|---|---|---|
| | -44 | 1700 | |
| | -66 | 1500 | |
| | -90 | 1350 | |
| Porcine Lung | 35 | 3680 | |
| | 13 | 3620 | |
| | -26 | 2040 | |
| | -58 | 1620 | |
| | -80 | 1440 | |
| Porcine Myocardium | 30 | 3590 | |
| | -34 | 1750 | |
| | -62 | 1508 | |
| | -98 | 1241 | |
| Porcine Liver | 0 | 3659 | [20] |
| | -73 | 1522 | |
| | -109 | 1192 | |
| | -147 | 941 | |

Table A1.7: Specific Heat capacity as function of temperature for various Tissue permeated with CPAs compiled from literature. Note, measurement technique for all the data is DSC as discolosed in source references.

| Tissue+CPA | Temperature (°C) | Specific Heat (J/kg.K) | Source |
|---|---|---|---|
| Porcine Liver+1xPBS+ 2M Glycerol | -4 | 3394 | [6, 20] |
| | -73 | 1611 | |
| | -109 | 1135 | |
| | -147 | 872 | |
| Porcine Liver+1xPBS+ 6M Glycerol | -24 | 2807 | |
| | -74 | 1993 | |
| | -110 | 1152 | |
| | -148 | 809 | |
| | -23 | 2688 | |

| | | | |
|---|---|---|---|
| Porcine Liver+1xPBS+8M Glycerol | -75 | 1969 | |
| | -111 | 1190 | |
| | -148 | 781 | |

# References for Appendix 1


1. Ratcliffe, E., *The thermal conductivity of ice new data on the temperature coefficient.* Philosophical Magazine, 1962. **7**(79): p. 1197-1203.
2. Bald, W. and J. Fraser, *Cryogenic surgery.* Reports on Progress in Physics, 1982. **45**(12): p. 1381.
3. Agafonkina, I., et al., *Thermal properties of human soft tissue and its equivalents in a wide low-temperature range.* Journal of Engineering Physics and Thermophysics, 2021. **94**: p. 233-246.
4. Ehrlich, L.E., et al., *Large thermal conductivity differences between the crystalline and vitrified states of DMSO with applications to cryopreservation.* PLoS One, 2015. **10**(5): p. e0125862.
5. Zhang, A., et al., *Determination of thermal conductivity of cryoprotectant solutions and cell suspensions.* Cell Preservation Technology, 2004. **2**(2): p. 157-162.
6. Choi, J. and J.C. Bischof, *Review of biomaterial thermal property measurements in the cryogenic regime and their use for prediction of equilibrium and non-equilibrium freezing applications in cryobiology.* Cryobiology, 2010. **60**(1): p. 52-70.
7. Choi, J.H. and J.C. Bischof, *A quantitative analysis on the thermal properties of phosphate buffered saline with glycerol at subzero temperatures.* International Journal of Heat and Mass Transfer, 2008. **51**(3-4): p. 640-649.
8. Li, Y., et al., *Measurement of thermal conductivities of two cryoprotective agent solutions for vitreous cryopreservation of organs at the temperature range of 77 K–300 K using a thermal sensor made of microscale enamel copper wire.* Biopreservation and Biobanking, 2017. **15**(3): p. 228-233.
9. Ehrlich, L.E., et al., *Thermal conductivity of cryoprotective agents loaded with nanoparticles, with application to recovery of preserved tissues and organs from cryogenic storage.* PLoS One, 2020. **15**(9): p. e0238941.
10. Ehrlich, L.E., J.A. Malen, and Y. Rabin, *Thermal conductivity of the cryoprotective cocktail DP6 in cryogenic temperatures, in the presence and absence of synthetic ice modulators.* Cryobiology, 2016. **73**(2): p. 196-202.
11. Rinfret, A., *Factors affecting the erythrocyte during rapid freezing and thawing.* Annals of the New York Academy of Sciences, 1960. **85**(2): p. 576-594.
12. Bai, X. and D.E. Pegg, *Thermal property measurements on biological materials at subzero temperatures.* 1991.
13. Zhang, H., et al., *Determination of thermal conductivity of biomaterials in the temperature range 233–313K using a tiny detector made of a self-heated thermistor.* Cell Preservation Technology, 2002. **1**(2): p. 141-147.
14. Tsiganov, D., *Cryomedicine: processes and apparatus.* SAYNS-PRESS, Moscow, 2011: p. 304.
15. Natesan, H., et al., *A micro-thermal sensor for focal therapy applications.* Scientific reports, 2016. **6**(1): p. 1-8.
16. Cherneeva, L., *Study of thermal properties of foods.* Report of Vnikhi (Scientific Research Institute of the Refrigeration Industry), Gostorgisdat, Moscow, 1956.

17. Hill, J.E., J.D. Leitman, and S. JE, *Thermal conductivity of various meats.* Food technology, 1967. **21**(8): p. 1143-&.
18. Chato, J. *Thermal Problems in Biotechnology*. in *ASME*. 1968.
19. Jiang, Z., et al., *Coupled experimental-modeling analyses of heat transfer in ex-vivo VS55-perfused porcine hepatic tissue being plunged in liquid nitrogen for vitreous cryopreservation.* International Journal of Heat and Mass Transfer, 2017. **106**: p. 970-979.
20. Choi, J.H. and J.C. Bischof, *A quantitative analysis of the thermal properties of porcine liver with glycerol at subzero and cryogenic temperatures.* Cryobiology, 2008. **57**(2): p. 79-83.
21. I., M.E., *THERMAL CONDUCTIVITY OF BIOLOGICAL TISSUES IN THE DOMAIN OF WATER CHANGE OF PHASE.* 1984, Kholodilnaya Tekhnika- n. 4.
22. Phatak, S., et al., *Measurement of specific heat and crystallization in VS55, DP6, and M22 Cryoprotectant systems with and without sucrose.* Biopreservation and biobanking, 2018. **16**(4): p. 270-277.
23. Phatak, S.S., *Thermal Analysis of Cryoprotectants for Cryopreservation*. 2017, University of Minnesota.
24. Natesan, H., *Development of a Micro-thermal Sensor Based on 3-omega Technique for Dynamic Freezing Applications*. 2019, University of Minnesota.

The following sections describe the author's contribution and participation in various other sub-studies.

# Appendix 2- Rat kidney thermal modeling

This body of work has been published as an article in Advanced Science. The publication is reproduced here.

Sharma, A., Rao, J. S., Han, Z., **Gangwar, L.**, Namsrai, B., Gao, Z., ... & Bischof, J. C. (2021). Vitrification and nanowarming of kidneys. *Advanced Science*, *8*(19), 2101691.


Abstract

Vitrification can dramatically increase the storage of viable biomaterials in the cryogenic state for years. Unfortunately, vitrified systems ≥3 mL like large tissues and organs, cannot currently be rewarmed sufficiently rapidly or uniformly by convective approaches to avoid ice crystallization or cracking failures. A new volumetric rewarming technology entitled "nanowarming" addresses this problem by using radiofrequency excited iron oxide nanoparticles to rewarm vitrified systems rapidly and uniformly. Here, for the first time, successful recovery of a rat kidney from the vitrified state using nanowarming, is shown. First, kidneys are perfused via the renal artery with a cryoprotective cocktail (CPA) and silica-coated iron oxide nanoparticles (sIONPs). After cooling at −40 °C $min^{-1}$ in a controlled rate freezer, microcomputed tomography (μCT) imaging is used to verify the distribution of the sIONPs and the vitrified state of the kidneys. By applying a radiofrequency field to excite the distributed sIONPs, the vitrified kidneys are nanowarmed at a mean rate of 63.7 °C $min^{-1}$. Experiments and modeling show the avoidance of both ice crystallization and cracking during these processes. Histology and confocal imaging show that nanowarmed kidneys are dramatically better than convective rewarming controls. This work suggests that kidney nanowarming holds tremendous promise for transplantation.


The following figure was author's contribution:

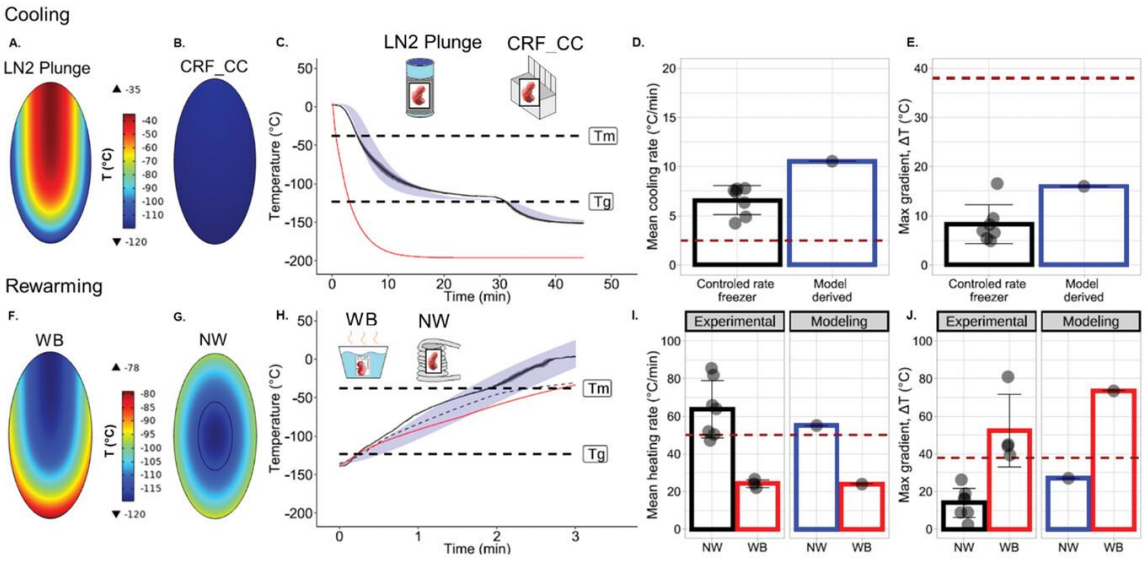


Figure A1: Computational thermal modeling of vitrification and rewarming of kidneys. A,B) Temperature distribution within a kidney approximated as an ellipsoid (2 cm x 1 cm x 1 cm), modeled at the coronal plane through the center for LN2 plunge (failure) and CRF convective cooling (success) cases, near $T_g$ (Supporting Information). C) Numerical solutions showing temperature versus time ($T$ vs $t$) plots for LN2 plunge (red = average of maximum and minimum cooling trajectories) and CRF convective cooling (blue shaded) relative to experimental plots (black-mean and gray-SD ribbon). The blue ribbons show spatial variation (range) in temperature within the kidney. Kidney cooling rate in CRF (black) was computed by taking the average of all temperature probes within a kidney, and then averaging this data over $n$ = 7 kidneys plotted with SD gray ribbon. D,E) Bar plots summarizing modeled cooling rates and maximum gradients $\Delta T$, respectively, within the kidney, relative to experimental values (See Supporting Information for calculation). Black scatter-plot of cooling rates, averaged over all probe locations for $n$ = 7 kidneys, (from Figure 3B) are shown overlaying the experimental bar plots for reference. Maroon dotted line in (D) indicates CCR of 8.4 m VS55. Maroon dotted line in (E) indicates $\Delta T_{max}$ threshold corresponding to stress-to-fracture limit, (38 °C) for VS55. CRF d$T$/d$t$ (blue bar in (D)) was computed by taking the average d$T$/d$t$ of the modeled maximum and minimum temperature rate limits across the modeled kidney volume. F,G) Temperature distribution within a kidney section taken through the center, for water-bath convective warming (WB) and Nanowarming (NW) of a kidney, near $T_g$. H) Numerical solutions showing temperature versus time ($T$ vs $t$) plots for WB rewarming (red) and Nanowarming (blue shaded) relative to experimental plots (black solid lines and gray ribbons representing mean and SD for NW, respectively). The gray SD ribbons show spatial variation (range) in temperature within the kidney. The black dashed line represents

experimental spatial-mean WB rewarming temperature averaged over three temperature probes. I,J) Bar plots summarizing modeled rewarming rates and maximum thermal gradients $\Delta T$, relative to experimental values. Black scatter plot of nanowarming rates, averaged over all probe locations for $n = 7$ kidneys, (from Figure 4B) are shown overlaying the experimental bar plots for reference. In (I), experimental NW (black bar) was computed by taking the average of all temperature probes within a kidney, and then averaging this data over $n = 7$ kidneys. For modeling in (I), NW $dT/dt$ was computed by taking the average of the maximum and minimum temperature rate limits across the modeled kidney volume.



# References for Appendix 2

[1] Sharma, A., et al., *Vitrification and Nanowarming of Kidneys.* Advanced Science, 2021. **8**(19): p. 2101691.

# Appendix 3- Cryomicroscopy during cooling and rewarming of CPAs

This body of work has been published as an article in Cryobiology. The publication is reproduced here.

Han, Z., **Gangwar, L.,** Magnuson, E., Etheridge, M. L., Pringle, C. O., Bischof, J. C., & Choi, J. (2022). Supplemented phase diagrams for vitrification CPA cocktails: DP6, VS55 and M22. *Cryobiology*, *106*, 113-121.

Abstract

DP6, VS55 and M22 are the most commonly used cryoprotective agent (CPA) cocktails for vitrification experiments in tissues and organs. However, complete phase diagrams for the three CPAs are often unavailable or incomplete (only available for full strength CPAs) thereby hampering optimization of vitrification and rewarming procedures. In this paper, we used differential scanning calorimetry (DSC) to measure the transition temperatures including heterogeneous nucleation temperatures (Thet), glass transition temperatures (Tg), rewarming phase crystallization (devitrification and/or recrystallization) temperatures (Td) and melting temperatures (Tm) while cooling or warming the CPA sample at 5 ◦C/min and plotted the obtained transition temperatures for different concentrations of CPAs into the phase diagrams. We also used cryomicroscopy cooling or warming the sample at the same rate to record the ice crystallization during the whole process, and we presented the cryomicroscopic images at the transition temperatures, which agreed with the DSC presented phenomena.

The following figure was author's contribution:

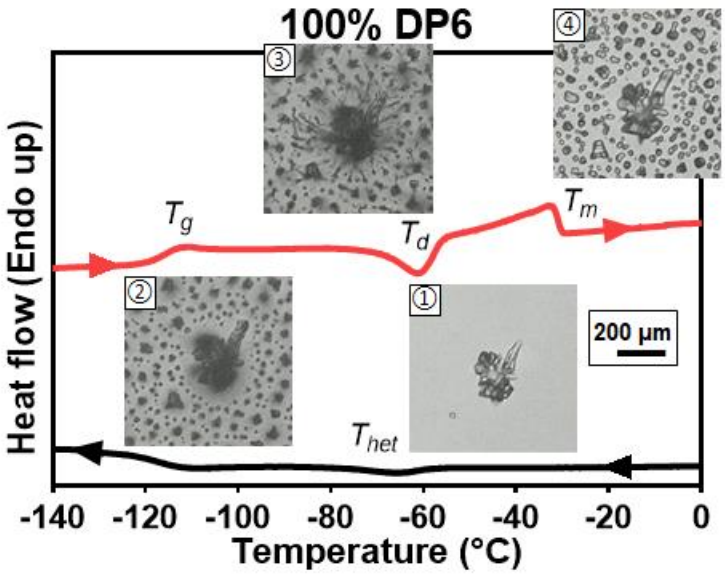


Figure A2: Example DSC thermogram of 100% DP6 during cooling (black) and warming (red). Inset Figs. 1–4: Cryomicroscopic images for 100% DP6 solution at Thet, Tg, Td and Tm, respectively when cooled and rewarmed at 5°C/min. (Adapted and modified from [1] with permission).

# References for Appendix 3

[1] Han, Z., et al., *Supplemented phase diagrams for vitrification CPA cocktails: DP6, VS55 and M22*. Cryobiology, 2022.

# Appendix 4- Differential Scanning Calorimetry to determine CCR, CWR in CPA equilibrated tissue of rat kidneys

This body of work is in submission. The manuscript is reproduced here.

Han, Z., **Gangwar, L.,** Namsrai, B., Rao J., Scheithauer, C., Etheridge, M. L., Finger E., Bischof, J. C., & Choi, J. (2024). In submission.

The author's contribution to this project was to partially measure critical cooling and warming rates (CCR, CWR) in kidney tissue permeated with VS55.

# Appendix 5- Inductive heating of Iron oxide Nanoparticle enhanced PHIL Embolic

This body of work is already published in ACS Applied Materials & Interfaces. The manuscript is reproduced here.

Pasek-Allen, J. L., Kantesaria, S., **Gangwar, L.,** Shao, Q., Gao, Z., Idiyatullin, D., ... & Bischof, J. C. (2022). Injectable and Repeatable Inductive Heating of Iron Oxide Nanoparticle-Enhanced "PHIL" Embolic toward Tumor Treatment. *ACS Applied Materials & Interfaces*, *14*(37), 41659-41670.

The author's contribution to this project was technical towards the development of magnetic field strength protocol and operation of 120 kW RF coil for inductive heating.

# Appendix 6- Kidney Vitrification and Transplant Project

This body of work is already published in Nature Communications. The manuscript is reproduced here.

Han, Z., Rao, J. S., **Gangwar, L.**, Namsrai, B. E., Pasek-Allen, J. L., Etheridge, M. L., ... & Finger, E. B. (2023). Vitrification and nanowarming enable long-term organ cryopreservation and life-sustaining kidney transplantation in a rat model. *Nature communications, 14*(1), 3407.

The author's contribution to this project was in DSC measurement of CCR, CWR for CPA solutions (VMP).and the development of organ vitrification protocol in control rate freezer (CRF).